A NUMERICAL STUDY OF
THE TIME DEPENDENT
SCHRÖDINGER EQUATION
COUPLED WITH NEWTONIAN GRAVITY

APPROVED BY
DISSERTATION COMMITTEE:

Supervisor: _____

_____

_____

_____

_____

This thesis is dedicated to my wife,

Choi-Ling, without whom life would not be so enticing.

A NUMERICAL STUDY OF
THE TIME DEPENDENT
SCHRÖDINGER EQUATION
COUPLED WITH NEWTONIAN GRAVITY

by

REID LARIMORE GUENTHER, B.A.

DISSERTATION

Presented to the Faculty of the Graduate School of

The University of Texas at Austin

in Partial Fulfillment

of the Requirements

for the Degree of

DOCTOR OF PHILOSOPHY

THE UNIVERSITY OF TEXAS AT AUSTIN

December 1995

Acknowledgements

A NUMERICAL STUDY OF
THE TIME DEPENDENT
SCHRÖDINGER EQUATION
COUPLED WITH NEWTONIAN GRAVITY

Publication No. _____

Reid Larimore Guenther, Ph.D.
The University of Texas at Austin, 1995

Supervisor: Richard Matzner

The dynamical study of a massive scalar field in the Newtonian regime could produce some interesting insights into the nature of bosonic matter. Since most of the dark matter in the universe is believed to be nonbaryonic in nature, the study of bosonic matter in the form of a massive bose condensate, boson stars, could lead into insights into dark matter. In this dissertation, I discuss a numerical study of the dynamics of a massive complex scalar field in three spatial dimensions. As the general relativistic equations are too complex to solve as part of an initial study, I move to the Newtonian regime where the behavior of the scalar field is described by the time dependent Schrödinger equation coupled with Newtonian gravity. I use an alternating directions implicit (ADI) finite difference method use to solve the Schrödinger equation while using a multigrid method to solve Poisson's equation . I then discuss how to check the convergence of the difference equations with the unknown analytic solution; a

technique particularly useful due to the richness of the solution space of difference equations. I show that the difference solutions in this dissertation are valid where the matter distribution is well resolved and the approximate boundary conditions have little effect on the order of convergence of the interior finite difference equations. Using boundary conditions which are valid at infinity on a finite computational domain causes errors in the solution. To stem this problem for the Schrödinger equation I developed a new technique for allowing matter to flow out of the computational domain and show the method is shown to be quite robust even in three dimensions. Finally, a numerical study of the dynamics of boson stars is given. It is found that the stars exhibit behavior similar to that of a point Newtonian mass as well as a collisionless fluid.

Table of Contents

List of Tables

List of Figures

Chapter 1

Introduction

1.1   The Problem

In this dissertation I discuss the numerical solution of a seemingly simple set
of coupled partial differential equations (PDEs):

$$i\hbar \frac{\partial \phi(\mathbf{x}, t)}{\partial t} = -\frac{\hbar^2}{2m} \nabla^2 \phi(\mathbf{x}, t) + mc^2 V(\mathbf{x}, t)\phi(\mathbf{x}, t) \qquad (1.1)$$

$$\nabla^2 V(\mathbf{x}, t) = 4\pi G \left(\frac{m}{\hbar c}\right)^2 \phi(\mathbf{x}, t)\phi^*(\mathbf{x}, t). \qquad (1.2)$$

where ϕ is a scalar field, V is a Newtonian potential, m is the mass of the
scalar field, $\hbar$ is Planck's constant, c is the speed of light and G is the gravi-
tational constant. Equation (1.1) is the time dependent form of Schrödinger's
equation, which describes the evolution of a massive complex scalar field in a
Galilean frame of reference, while the second is Poisson's equation where $c^2 V$
is the Newtonian potential generated by a distribution of matter $(m/\hbar)^2 \phi\phi^*$.
Upon first glimpse, one might ask, "Why study such a seemingly simple set of
equations?" Well, this being a dissertation in numerical relativity, one should
expect there to be both physical and computational reasons.

One physical motivation is that equations (1.1) and (1.2) are the weak
field limit of the general relativistic equations governing the behavior of a mas-

sive scalar field. Thus any solution of the general relativistic equations must converge to solutions of (1.1) and (1.2) in the weak field limit. Also, since there are currently no studies of the $(3 + 1)$ dynamics of a massive complex scalar field, a three dimensional numerical study of the field even in the Newtonian regime is something that should be done. Another reason is dark matter. Since the time dependent Schrödinger equation coupled with a gravitational potential describes zero temperature bosons in the Newtonian regime [26], and it is believed that most of the dark matter in the universe is nonbaryonic in nature [26], solutions of (1.1) and (1.2) could shed some "light" on the nature of dark matter. Another reason is that when viewed on cosmological scales these equations describe large scale structure formation with only slight modification for an Einstein-de Sitter universe. [61]

There are also numerous computational reasons to study (1.1) and (1.2). One is the need to examine optimal numerical finite difference techniques for integrating time dependent three dimensional PDEs because of the large number of computations usually needed to computationally integrate most physically interesting three dimensional problems while maintaining a low error ($< 1\%$). In the spirit of Brandt's golden rule: [4]

> The amount of computational work should be proportional to the amount of real physical changes in the computed system.

There is a need to implement the finite difference algorithm used in this dissertation in an adaptive mesh format, and to speed up the computation of (1.1) and (1.2) even more, parallel methods on multiple instruction multiple data (MIMD) machines should be examined. There is also a need to examine how

to implement boundary conditions on a finite grid for time dependent PDEs with infinite domains. All the above reasons validate the research discussed in this dissertation. Also, because this work is supported by a Grand Challenge grant, another reason for studying the time dependent Schrödinger equation coupled with Poisson's equation is that the numerical knowledge gained here will contribute to the Computational Grand Challenge Problem of the coalescence of two black holes [37].

1.2   Physical Motivation

Understanding, the nature of dark matter is one of the biggest challenges in astrophysics today. It holds implications for the existence of new exotic particles, is felt to be directly responsible for the formation of galaxies and could help astrophysicists understand the birth of our universe as well as determine its ultimate fate.[42]

Standard big bang cosmology posits the existence of a critical matter density ρ_{crit} in the universe below which the universe will continue expanding (ad infinitum); and above which the universe will recollapse upon itself. The ratio of the density of luminous matter observed in the universe to the critical density is:

$$\Omega_{lum} \equiv \rho_{lum}/\rho_{crit} < 0.01. \tag{1.3}$$

There is evidence from Doppler shifts of spectral lines of stars and from 21cm radiation from neutral gas clouds of nonluminous matter in the halos of spiral galaxies. [17, 47, 49, 50] The rotational velocity curves of these galaxies have the same pattern. They portray galaxies as having a rapid rise in density from the galactic center with the density becoming constant near the edge of the

luminous halo. These velocity curves lead to the prediction that:

$$\Omega_{halo} \geq 0.03 - 0.1. \tag{1.4}$$

There is also evidence of dark matter in the halos of irregular and elliptical galaxies. Big bang nucleosynthesis predicts: [29]

$$0.011 \leq \Omega_{baryon} \leq 0.12 \tag{1.5}$$

where the main uncertainty is due to the Hubble parameter [42] which enters quadratically. Because the range of Ω_{baryon} lies within the range of Ω_{halo}, the dark matter in the halos of galaxies could be baryonic. In 1933, Zwicky found that the mass needed to bind galaxy clusters was greater than the observed luminous matter. [65] By use of the virial theorem, he estimated from his findings for several clusters that:

$$\Omega_{cluster} \simeq 0.1 - 0.3. \tag{1.6}$$

From the Infrared Astronomical Satellite, sky surveys of infrared-selected galaxies indicate that the cluster mass density could be even higher than Zwicky's results and could be close to the critical density[26]. Limits for the deceleration parameter and the age of the universe predict that Ω_{univ} has an upper limit of 2 while the currently popular inflationary models predict that the $\Omega_{univ} = 1$. Finally, anisotropies of the Cosmic Microwave Background Radiation also give indications that the dark matter content of the universe is sizable. [19]

All of this evidence suggests that a large portion of the matter in the universe is nonbaryonic in nature. There are many possible candidates such as heavy neutrinos, neutralinos, axions, etc. Some of these dark matter candidates

could be bosons. (e.g. axions, Higgs, scalar neutrinos,...) These scalar particles could exist in diffuse gas clouds and compact objects and could also be mixed with baryonic matter. Thus there is a need to study compact objects made of scalar particles; such objects are commonly referred to as boson stars. To obtain a realistic picture of these objects, one would need to know more about the nature of the particles, such as their mass and the types of self-interactions besides gravity. One of the problems of bosons as a dark matter candidate is that bosons are predicted to be unstable and decay rapidly. This is not a problem for boson stars as they are predicted to be:

> macroscopic bose condensates formed by the vacuum expectation value of the scalar field [26].

The actual physical particles are excitations over the vacuum state. Thus the short lifetimes are for the particles and not for the vacuum expectation value of the scalar field.

As mentioned in the previous section, equations (1.1) and (1.2) can simulate large scale structure with only slight modifications [61]. This is possible because the Schrödinger equation can be used to approximate the collisionless Boltzmann equation [55] where the squared modulus of the Schrödinger wave function is the matter density. This is possible because of the equivalence between the classical mechanics of point particles and wave mechanics in the geometric optics limit. Thus the Schrödinger wave function $\phi(\mathbf{x}, t)$ contains both position and momentum information as a position space function. A distribution function $\mathrm{F}(\mathbf{x}, \mathbf{p}, t)$ containing phase space information can be constructed by convolving ϕ with a window function centered at $\mathbf{x}$, taking the

Fourier transform and squaring the result. So by constructing a particular distribution of matter and inserting it into the right hand side of (1.2), one can perform many types of simulations such as stellar dynamics [15, 60] and large scale structure formation from cold dark matter. [61]

1.3   Computational Motivation

Most computational techniques for solving initial boundary value problems [40] lead to solving a set of linear equations:

$$Au^{n+1} = Bu^n \tag{1.7}$$

where A and B are $N \times N$ arrays; $\mathbf{u}^{n+1}$ and $\mathbf{u}^n$ are vectors of length N at times $(n+1)\Delta t$ and $n\Delta t$ respectively for some time step Δt; and one begins with initial data usually at $n = 0$. Thus if one has N grid points in a three dimensional mesh and increases the resolution of the grid by an integer factor α to lower the truncation error of the difference equations, the total number of linear equations used to solve the difference system grows by a factor of α^3. If one uses a direct solver such as LU decomposition, [43] the number of calculations needed to solve a system of N linear equations is of order N^3. This means that the number of calculations and thus the time to solve the difference equations grows by α^6 when increasing resolution by a factor of α. If one uses an iterative method such as Gauss-Seidel, [63, 64] the number of calculations needed to solve effectively the system of linear equations grow by a factor of α^5 as one increases resolution. Optimal solvers such as ADI (alternating direction implicit) [40] and multi-grid [59] take $O(N)$ calculations to solve the N difference equations of the initial boundary value problem. Thus when increasing

resolution of the three dimensional differencing scheme by a factor of α, the number of calculations needed to solve the system grows by α^3 and stays in linear proportion to the number of grid points. Since N is usually quite large for the smooth resolution of three dimensional finite difference problems, there is a need to use optimal solving techniques such as ADI and multi-grid when solving these problems.

Since Cauchy problems have boundary conditions at infinity, a difference solution of a Cauchy problem on a finite grid has the complication of how to implement approximate boundary conditions. An initial approach is to use extrapolated boundary conditions where the solution at the spatial boundaries is found by simply extrapolating from points interior to the boundary. This works fine when the solution near the boundaries remains small when compared with the interior solution but can cause errors when the boundary solution grows large. Take the finite differenced wave equation as an example. In the difference solution using extrapolated boundary conditions a wave packet that encounters the boundary of the grid will simply bounce off the boundary, whereas in reality it should propagate off the computational grid. Difference solutions to the Schrödinger equation have a similar problem and thus there is a need to implement absorbing boundary conditions like those used by Israeli and Orszag for the wave equation [23].

Keeping Brandt's *golden rule* [4] in mind can help researchers can optimize their numerical solutions of physical problems. For most finite difference solutions to multi-dimensional time dependent PDEs, this means using of multi level adaptive methods which, if used properly, can increase the resolution of the difference grid only where needed. One of these methods is the adaptive mesh

refinement (AMR) technique of Berger and Oliger [3] which can be used to solve initial boundary value problems. There are numerous examples of AMR solutions of one and two spatial dimension time dependent problems [9, 44, 18] while not much has been done for three dimensional problems[37] especially in numerical relativity. The problem with AMR is how to implement the data structures needed to keep track of all the grids and how to group designated points on a grid scheduled for regridding. This is still a very active area of research and thus many computational scientists use unigrid techniques and leave AMR for the computer scientists. But to obtain numerical solutions to many multidimensional time dependent problems such as (1.1) and (1.2) in a reasonable amount of real time (on the order of days), AMR is a must.

The most important motivation for this dissertation is that the knowledge gained here should help advance the Computational Grand Challenge effort of coalescing black hole binaries. Currently, this is the major effort of numerical relativity and will involve "fundamental new approaches to computation, architecture and algorithm." [37] In the course of this effort, a modular toolkit is being developed by physicists and computer scientists that can be used to generate time dependent finite difference codes with the data structures for AMR already in place. The belief is that a researcher with a working unigrid code that can benefit from AMR would only need to define his difference scheme and have a general knowledge of the Berger and Oliger algorithm [3] to produce a three dimensional AMR code that runs in parallel. The solution of (1.1) and (1.2) provides a nontrivial problem to use to develop these tools. Another of the computational aspects of this Computational Grand Challenge effort will be the implementation of boundary conditions for gravitational waves moving

off towards infinity. Thus, the development of boundary conditions for (1.1) and (1.2) could also give some insight into this facet of the Grand Challenge.

1.4 The Contents of this Dissertation

The next chapter goes through a somewhat detailed description of how equations (1.1) and (1.2) are derived from the general relativistic action for a complex scalar field. The Chapter also discusses an analogue between the Schrödinger equation and the continuity and Euler's equations for a compressible fluid in a gravitational field. Then in chapter 3, the difference equations for equations (1.1) and (1.2) are derived and a discussion of how to test the validity of the difference solution is given. Chapter 4 gives a description of a new type of boundary layer that can be applied near the boundaries of the computational domain to prevent reflections off the boundary. Chapter 5 presents the results of giving boson stars linear and angular momentum. Also, an attempt to orbit a boson star is made. Finally, the last chapter concludes with some remarks summing up this dissertation and gives a few directions for further research.

Chapter 2

Derivation of the Physical Problem

As there are many instances in research papers where the authors make use of a derivation which they say is contained within a specified work but in actuality is not, in this chapter I present a somewhat pedagogical guide of how one goes from the general relativistic action for a massive complex scalar field to the Einstein and Klein-Gordon equations describing the behavior of the field. Using these equations, I then discusss how one obtains the Schrödinger equation as well as Poisson's equation for the Newtonian potential. In section 2.2.3, I show that there is a conserved current which in the Newtonian limit leads to mass conservation, an important concept for this dissertation and our universe. In the final section, I derive an analogy to the hydrodynamic equations for a compressible fluid in a gravitational field from Schrodinger's equation. This form of Schrödinger's equation will be of use in understanding some of the results in Chapter 5.

2.1 Derivation of the Field Equations

The general relativistic action of a massive scalar field Φ [1] is: [53]

$$
\begin{aligned}
I &= \int d^4x \sqrt{-g}\mathcal{L} \\
&= \int d^4x \sqrt{-g} \left[\frac{Rc^4}{4\pi G} - \mathcal{L}_\Phi \right] \\
&= \int d^4x \sqrt{-g} \left[\frac{Rc^4}{4\pi G} - \frac{1}{2} \left(g^{\mu\nu}\Phi_{;\mu}\Phi^*_{;\nu} + \left(\frac{mc}{\hbar}\right)^2 \Phi\Phi^* \right) \right]
\end{aligned}
\tag{2.1}
$$

where the integral is over all spacetime which is flat at infinity, g is the determinant of the metric, R is the Ricci scalar, m is the mass of the field particle, I use units where $G \neq c \neq \hbar \neq 1$, and $(mc/\hbar)^2 \Phi\Phi^*$ is the energy density of the field. As one may have noticed, the Φ here is not the same ϕ in equations (1.1) and (1.2). In section 2.2.2, under an assumed limit, Φ is defined to be the field ϕ times a time varying phase factor.

2.1.1 Einstein's Equations

In order to find Einstein's equations, one takes the variation of the action (2.1) with respect to the metric $g_{\mu\nu}$:

$$
\frac{\delta I}{\delta g_{\mu\nu}} = \int d^4x \left[\frac{\delta\sqrt{-g}}{\delta g_{\mu\nu}}\mathcal{L} + \sqrt{-g} \left(\frac{c^4}{16\pi G} \left(\frac{g^{\alpha\beta}\delta R_{\alpha\beta}}{\delta g_{\mu\nu}} + \frac{\delta g^{\alpha\beta}R_{\alpha\beta}}{\delta g_{\mu\nu}} \right) - \frac{\delta\mathcal{L}_\Phi}{\delta g_{\mu\nu}} \right) \right] = 0
\tag{2.2}
$$

To find the first term in brackets, one uses:

$$
\frac{\partial g}{\partial g_{\mu\nu}} = g g^{\alpha\beta}\frac{\partial g_{\alpha\beta}}{\partial g_{\mu\nu}} = g g^{\mu\nu}
\tag{2.3}
$$

so that:

$$
\frac{\delta\sqrt{-g}}{\delta g_{\mu\nu}} = \frac{\partial\sqrt{-g}}{\partial g_{\alpha\beta}}\frac{\delta g_{\alpha\beta}}{\delta g_{\mu\nu}} = \frac{-1}{2\sqrt{-g}}\frac{\partial g}{\partial g_{\mu\nu}} = \frac{\sqrt{-g}}{2}g^{\mu\nu}
\tag{2.4}
$$

---

[1] without the explicit self interacting $\lambda|\Phi|^4$ term

In terms of variations of Christoffel symbols, the variation of the Ricci tensor is:

$$\delta R_{\mu\nu} = \left[\left(\delta \Gamma^{\alpha}_{\mu\nu} \right)_{,\alpha} - \left(\delta \Gamma^{\alpha}_{\mu\alpha} \right)_{,\nu} - \delta \left(\Gamma^{\alpha}_{\rho\nu} \Gamma^{\rho}_{\mu\alpha} - \Gamma^{\alpha}_{\rho\alpha} \Gamma^{\rho}_{\mu\nu} \right) \right] \tag{2.5}$$

from this it can be shown somewhat tediously:

$$g^{\mu\nu} \delta R_{\mu\nu} = \frac{1}{\sqrt{-g}} \left[\sqrt{-g} \left(g^{\mu\nu} \delta \Gamma^{\alpha}_{\mu\nu} - g^{\mu\alpha} \delta \Gamma^{\nu}_{\mu\nu} \right) \right]_{,\alpha} \tag{2.6}$$

Since I wish to examine the scalar field in a spacetime that is flat at infinity, the integral:

$$\int d^4x \sqrt{-g} g^{\mu\nu} \delta R_{\mu\nu} = \int d^4x \left[\sqrt{-g} \left(g^{\mu\nu} \delta \Gamma^{\alpha}_{\mu\nu} - g^{\mu\alpha} \delta \Gamma^{\nu}_{\mu\nu} \right) \right]_{,\alpha} = 0 \tag{2.7}$$

vanishes. To find the third term in brackets in (2.2) one uses the relation:

$$\frac{\delta g^{\alpha\beta}}{\delta g_{\mu\nu}} = -\frac{1}{2} \left(g^{\alpha\gamma} g^{\beta\omega} + g^{\alpha\omega} g^{\beta\gamma} \right) \frac{\delta g_{\gamma\omega}}{\delta g_{\mu\nu}} = -\frac{1}{2} \left(g^{\alpha\mu} g^{\beta\nu} + g^{\alpha\nu} g^{\beta\mu} \right) \tag{2.8}$$

The final variation, the variation of $\mathcal{L}_\Phi$ with respect to the metric, is:

$$\frac{\delta \mathcal{L}_\Phi}{\delta g_{\mu\nu}} = \frac{1}{4} \left(g^{\mu\alpha} g^{\nu\omega} \Phi_{,\alpha} \Phi^*_{,\omega} + g^{\mu\alpha} g^{\nu\omega} \Phi_{,\omega} \Phi^*_{,\alpha} \right) \tag{2.9}$$

Plugging in (2.4), (2.7), (2.8) and (2.9), the variation of the action with respect to the metric function $g_{\mu\nu}$ becomes:

$$\frac{\delta I}{\delta g_{\mu\nu}} = \int d^4x \sqrt{-g} \left[\frac{g^{\mu\nu} \mathcal{L}}{2} - \frac{c^4 g^{\mu\alpha} g^{\nu\omega} R_{\alpha\omega}}{16\pi G} \right.$$
$$\left. + \frac{1}{4} \left(g^{\mu\alpha} g^{\nu\omega} \Phi_{,\alpha} \Phi^*_{,\omega} + g^{\mu\alpha} g^{\nu\omega} \Phi_{,\omega} \Phi^*_{,\alpha} \right) \right] = 0. \tag{2.10}$$

Since this must be true for any scalar field and flat spacetime at infinity, the term in brackets must be identically zero:

$$\frac{c^4 g^{\mu\nu} R}{32\pi G} - \frac{1}{4} \left(g^{\mu\nu} \Phi^{;\alpha} \Phi^*_{;\alpha} + \left(\frac{mc}{\hbar} \right)^2 \Phi \Phi^* \right) - \frac{c^4 R^{\mu\nu}}{16\pi G} + \frac{1}{4} \left(\Phi^{;\mu} \Phi^{*;\nu} + \Phi^{;\nu} \Phi^{*;\mu} \right) = 0 \tag{2.11}$$

which leads to the Einstein field equations:

$$R^{\mu\nu} - \frac{1}{2}g^{\mu\nu}R = \frac{8\pi G}{c^4}T^{\mu\nu} \tag{2.12}$$

where the stress energy tensor $(T^{\mu\nu})$ is:

$$T^{\mu\nu} = \frac{1}{2}\left[\Phi^{;\mu}\Phi^{*;\nu} + \Phi^{;\nu}\Phi^{*;\mu} - g^{\mu\nu}\left(\Phi^{;\alpha}\Phi^*_{;\alpha} + \left(\frac{mc}{\hbar}\right)^2\Phi\Phi^*\right)\right] \tag{2.13}$$

2.1.2   The Klein-Gordon Equation

One obtains the Klein-Gordon equations by variation of the action (2.1) with respect to Φ^*:

$$\frac{\delta I}{\delta\Phi^*} = \frac{1}{2}\int d^4x \left[\left(\sqrt{-g}g^{\mu\nu}\Phi_{;\mu}\right)_{,\nu} - \sqrt{-g}\left(\frac{mc}{\hbar}\right)^2\Phi\right] \tag{2.14}$$

where the first term in brackets was obtained by integration by parts. One can simplify the first term in brackets by using the relation:

$$\frac{1}{\sqrt{-g}}\left(\sqrt{-g}g^{\mu\nu}\Phi_{;\mu}\right)_{,\nu} = g^{\mu\nu}\Phi_{;\mu\nu} \tag{2.15}$$

Thus (2.14) becomes:

$$\int d^4x\sqrt{-g}\left[g^{\mu\nu}\Phi_{;\mu\nu} - \left(\frac{mc}{\hbar}\right)^2\Phi\right] = 0 \tag{2.16}$$

and again because this must be true for all Φ and $g_{\mu\nu}$, the term in brackets must be zero which is the Klein-Gordon equations for a massive scalar field:

$$g^{\mu\nu}\Phi_{;\mu\nu} - \left(\frac{mc}{\hbar}\right)^2\Phi = 0 \tag{2.17}$$

2.2   Weak Field Limits

2.2.1   Newtonian Potential

In the Newtonian limit of general relativity, it can be shown that: [39, 58, 52]

$$\nabla^2 V = \frac{4\pi G}{c^4}T^{00} \tag{2.18}$$

where V is the Newtonian potential for a mass density given by T^{00}/c^2. In this limit, the components of the metric may be taken to be:

$$g_{00} = -(1+2V); \ g_{kk} = (1-2V), k = 1, 2 \text{ or } 3; \ g_{\alpha\beta} = 0 \text{ for } \alpha \neq \beta. \quad (2.19)$$

In the rest of the subsection, I use units $G = c = \hbar = 1$ down to where I obtain the desired results. In these units, the Newtonian limit assumes:

$$V \simeq O(\epsilon^2), \ \frac{T^{00}}{m^2 \Phi \Phi^*} \simeq O(1), \ \frac{T^{0n}}{m^2 \Phi \Phi^*} \simeq O(\epsilon), \ \frac{T^{nn}}{m^2 \Phi \Phi^*} \simeq (\epsilon^2) \quad (2.20)$$

where $\epsilon \ll 1$, and $n = 1, 2,$ or 3. Thus the T^{00} component of the scalar field energy density divided by $m^2 \Phi \Phi^*$ is:

$$\frac{T^{00}}{m^2 \Phi \Phi^*} = \frac{1}{2} \left(\frac{(1-2V)^2}{m^2 \Phi \Phi^*} \Phi_{,0} \Phi_{,0}^* + \frac{(1-4V^2)}{m^2 \Phi \Phi^*} \sum_{k=1}^{3} \Phi_{,k} \Phi_{,k}^* + (1-2V) \right) \quad (2.21)$$

and the T^{nn} component divided by $m^2 \Phi \Phi^*$ is:

$$
\begin{aligned}
\frac{T^{nn}}{m^2 \Phi \Phi^*} &= \frac{1}{2} \left(-\frac{(1-4V^2)}{m^2 \Phi \Phi^*} \Phi_{,0} \Phi_{,0}^* + \frac{(1+2V)^2}{m^2 \Phi \Phi^*} \sum_{k=1}^{3} \Phi_{,k} \Phi_{,k}^* + (1+2V) \right) \\
&\quad - \frac{(1+2V)^2}{m^2 \Phi \Phi^*} \Phi_{,n} \Phi_{,n}^*.
\end{aligned}
\quad (2.22)
$$

Summing the 11, 22 and 33 components of $T^{\mu\nu}$ divided by $m^2 \Phi \Phi^*$ is:

$$\frac{\sum_{k=1}^{3} T^{kk}}{m^2 \Phi \Phi^*} = -\frac{3}{2} \frac{(1-4V^2)}{m^2 \Phi \Phi^*} \Phi_{,0} \Phi_{,0}^* - \frac{(1+2V)^2}{m^2 \Phi \Phi^*} \sum_{k=1}^{3} \Phi_{,k} \Phi_{,k}^* + (1+2V) \simeq O(\epsilon^2)$$

$$(2.23)$$

Thus the term containing the spatial derivatives divided by $(1+2V)$ is:

$$\frac{(1+2V)}{m^2 \Phi \Phi^*} \sum_{k=1}^{3} \Phi_{,k} \Phi_{,k}^* = -\frac{(1-2V)}{m^2 \Phi \Phi^*} \Phi_{,0} \Phi_{,0}^* + 1 + O(\epsilon^2) \quad (2.24)$$

Plugging this back into $T^{00}/(m^2 \Phi \Phi^*)$ and canceling terms:

$$\frac{T^{00}}{m^2 \Phi \Phi^*} = (1-2V) + O(\epsilon^2) \quad (2.25)$$

Taking only the $O(1)$ term one finds:

$$T^{00} \simeq m^2 \Phi \Phi^* \qquad (2.26)$$

Then plugging T^{00} into equation (2.18), one obtains:

$$\nabla^2 V \simeq 4\pi m^2 \Phi \Phi^* \qquad (2.27)$$

Going back to units where $G \neq c \neq \hbar \neq 1$, this becomes:

$$\nabla^2 V \simeq 4\pi G \left(\frac{m}{\hbar c}\right)^2 \Phi \Phi^* \qquad (2.28)$$

which is the equation for the Newtonian potential $(c^2 V)$ with a mass density given by:

$$\rho = \left(\frac{m}{\hbar}\right)^2 \Phi \Phi^*. \qquad (2.29)$$

2.2.2 The Schrödinger Equation

From the Klein-Gordon equation and the equations of the Newtonian metric in units where $G = c = \hbar = 1$, one gets:

$$-(1 - 2V)\,\Phi_{,tt} + (1 + 2V)\,\nabla^2 \Phi - m^2 \Phi = 0. \qquad (2.30)$$

Defining Φ to be:

$$\Phi(\mathbf{x}, t) \equiv \phi(\mathbf{x}, t) e^{-imt}, \qquad (2.31)$$

then the second time derivative of Φ becomes:

$$\Phi_{,tt} = \left(-im\phi_{,t} + \phi_{,tt}\right) e^{-imt} - im\left(-im\phi + \phi_{,t}\right) e^{-imt} \qquad (2.32)$$

Plugging this into (2.30) and dividing by $m^2 \phi$ and dropping the exponential:

$$-2V + 2i\left(1 - 2V\right)\frac{\phi_{,t}}{m\phi} + \left(1 - 2V\right)\frac{\phi_{,tt}}{m^2 \phi} + \left(1 + 2V\right)\frac{\nabla^2 \phi}{m^2 \phi} = 0. \qquad (2.33)$$

Assuming that:

$$V \simeq O(\epsilon), \quad \left| \frac{\phi_{,t}}{m\phi} \right| \simeq O(\epsilon), \quad \left| \frac{\phi_{,tt}}{m^2\phi} \right| \simeq O(\epsilon), \quad \left| \frac{\nabla^2\phi}{m^2\phi} \right| \simeq O(\epsilon), \tag{2.34}$$

then dropping the order ϵ^2 terms in equation (2.33)

$$-2V + 2i\frac{\phi_{,t}}{m\phi} + \frac{\phi_{,tt}}{m^2\phi} + \frac{\nabla^2\phi}{m^2\phi} = 0. \tag{2.35}$$

Rearranging terms this becomes:

$$i\phi_{,t} = -\frac{1}{2m}\nabla^2\phi + mV\phi \tag{2.36}$$

Converting back to units $G \neq c \neq \hbar \neq 1$, one obtains:

$$i\hbar\phi_{,t} = -\frac{\hbar^2}{2m}\nabla^2\phi + mc^2V\phi \tag{2.37}$$

which is the Schrödinger equation.

2.2.3 Mass Conservation

There exists a conserved current for the Klein-Gordon equation:

$$J^\mu = -\frac{i}{2\hbar}g^{\mu\nu}\left(\Phi_{;\nu}\Phi^* - \Phi\Phi^*_{;\nu}\right) \tag{2.38}$$

which one can see is conserved by taking the covariant divergence of J^μ:

$$
\begin{aligned}
J^\mu{}_{;\mu} &= -\frac{i}{2\hbar}g^{\mu\nu}{}_{;\mu}\left(\Phi_{;\nu}\Phi^* - \Phi\Phi^*_{;\nu}\right) \\
&\quad -\frac{i}{2\hbar}g^{\mu\nu}\left(\Phi_{;\nu}\Phi^*_{;\mu} - \Phi_{;\mu}\Phi^*_{;\nu}\right) \\
&\quad -\frac{i}{2\hbar}g^{\mu\nu}\left(\Phi_{;\mu\nu}\Phi^* - \Phi\Phi^*_{;\mu\nu}\right) = 0
\end{aligned}
\tag{2.39}
$$

The first term vanishes since $g^{\mu\nu}{}_{;\nu} = 0$, the second term vanishes assuming the symmetry of the spacetime metric, and the third term vanishes if the field

equation (2.17) is satisfied. equation (2.17). Associated with this conserved current is also a conserved scalar particle number on a $t =$constant surface:

$$N_p = \frac{1}{c} \int d^3x \sqrt{-g} J^0 \tag{2.40}$$

This is conserved if the integral is over all space. If one plugs in the Φ given by equation (2.31) and uses the Newtonian metric (2.19), the J^0 component of the current is:

$$J^0 = \frac{mc}{\hbar^2} \phi\phi^* \tag{2.41}$$

where terms of $O(V^2)$ have been dropped. Thus, the conserved particle number in the Newtonian limit is:

$$N_p = \frac{m}{\hbar^2} \int d^3x \, \phi\phi^* \tag{2.42}$$

This should be correct since the Newtonian density ρ is $(m/\hbar)^2\phi\phi^*$. Also note that any solution of equations (1.1) and (1.2) should conserve N_p. So this provides one of the ways to check a finite difference solution of the time dependent Schrödinger equation coupled with Newtonian gravity.

2.3   A Hydrodynamic Model for Schrödinger's Equation

In quantum mechanics, Schrödinger's equation describes the dynamics of a set of particles when the Heisenberg uncertainty principle becomes important in relating a possible range of positions and momenta for the set of particles. In this quantum regime, the certainty of position and momentum of a point particle is longer prevails. Instead these parameters can only be described by a position density function, $\phi(\mathbf{x},t)\phi^*(\mathbf{x},t)$ which gives the probable location of

the particle in position space or described by the probable momentum density, $\phi(\mathbf{p}, t)\phi^*(\mathbf{p}, t)$, in momentum space. [38]

In fluid mechanics, the continuity and Euler equations describe the behavior of a perfect fluid. Along with an equation of state, these equations approximate the behavior of a large number of molecules when one wants to predict the behavior of these molecules on a spatial scale much larger than the average distance between molecules.[33] Thus when the probability density of the Schrödinger is viewed in an analogous fashion to that of the density of a fluid, one should expect that solutions of the Schrödinger's equation exhibit fluid like behavior. This section presents a derivation of an analogous set of equations to the continuity and Euler's equations for a compressible self-gravitating fluid from the Schrödinger equation, (2.37). [55, 35, 13, 14, 32]

Given the definition of density,

$$\rho(\mathbf{x}, t) = (\frac{m}{\hbar})^2 \phi\phi^* \tag{2.43}$$

the time derivative of density is:

$$\frac{\partial \rho}{\partial t} = \frac{\partial(\phi^*\phi)}{\partial t} = \left(\frac{m}{\hbar}\right)^2 \left(\phi\frac{\partial\phi^*}{\partial t} + \phi^*\frac{\partial\phi}{\partial t}\right) \tag{2.44}$$

which after replacing the time derivatives with the right hand side of the Schrödinger equation, becomes:

$$\frac{\partial\rho}{\partial t} = \frac{m^2\phi^*}{i\hbar^3}\left(\frac{-\hbar^2}{2m}\nabla^2\phi + mc^2 V\phi\right) - \frac{m^2\phi}{i\hbar^3}\left(\frac{-\hbar^2}{2m}\nabla^2\phi^* + mc^2 V\phi^*\right). \tag{2.45}$$

Upon simplification, one obtains:

$$\frac{\partial\rho}{\partial t} = -\frac{m}{2\hbar^2}\nabla\cdot\left(\phi^*\nabla\phi - \phi\nabla\phi^*\right). \tag{2.46}$$

Now define a current density as:

$$\mathbf{j} \equiv \frac{m}{2i\hbar^2}\left(\phi^*\nabla\phi - \phi\nabla\phi^*\right), \tag{2.47}$$

and write the scalar field of the Schrödinger equation as:

$$\phi(\mathbf{x},t) = A(\mathbf{x},t)e^{i\frac{S(\mathbf{X},t)}{\hbar}} \tag{2.48}$$

where A and S are well-behaved real valued functions. So one sees that:

$$\frac{\partial\rho}{\partial t} = -\nabla\cdot\mathbf{j} = -\frac{m}{\hbar^2}\nabla\cdot(\phi\phi^*\nabla S) = -\nabla\cdot\left(\frac{\rho}{m}\nabla S(\mathbf{x},t)\right) \tag{2.49}$$

which is just a continuity equation describing the conservation of matter over time as proved in the previous section. To obtain a form of Euler's equation from the Schrödinger equation, (2.37), input the form of the field in equation (2.48) into the Schrödinger equation:

$$i\hbar\frac{\partial\phi}{\partial t} = i\hbar e^{i\frac{S}{\hbar}}\frac{\partial A}{\partial t} - Ae^{i\frac{S}{\hbar}}\frac{\partial S}{\partial t} = -\frac{\hbar^2}{2m}\left(\nabla\cdot\left(e^{i\frac{S}{\hbar}}\nabla A + \frac{i}{\hbar}Ae^{i\frac{S}{\hbar}}\nabla S\right)\right) + mc^2VAe^{i\frac{S}{\hbar}}. \tag{2.50}$$

The full blown form of the right hand side is:

$$= -\frac{\hbar^2}{2m}\left(\frac{2i}{\hbar}e^{i\frac{S}{\hbar}}\nabla S\cdot\nabla A + e^{i\frac{S}{\hbar}}\nabla^2 A + \frac{i}{\hbar}Ae^{i\frac{S}{\hbar}}\nabla^2 S - \frac{1}{\hbar^2}Ae^{i\frac{S}{\hbar}}\left(\nabla S\right)^2\right) + mc^2VAe^{i\frac{S}{\hbar}}. \tag{2.51}$$

Bringing the time derivative of A to the right hand side and dropping the exponential, one obtains:

$$-A\frac{\partial S}{\partial t} = -i\hbar\frac{\partial A}{\partial t} - \frac{i\hbar}{m}\nabla S\cdot\nabla A - \frac{\hbar^2}{2m}\nabla^2 A - \frac{i\hbar}{2m}A\nabla^2 S + \frac{A}{2m}\left(\nabla S\right)^2 + mc^2VA. \tag{2.52}$$

To transform this equation into the form of Euler's equation, use the relation:

$$\frac{\partial\rho}{\partial t} = \frac{\partial A^2}{\partial t} = 2A\frac{\partial A}{\partial t} = -\nabla\left(\frac{1}{m}A^2\nabla S\right) = -\frac{2A}{m}\nabla A\cdot\nabla S - \frac{A^2}{m}\nabla^2 S \tag{2.53}$$

which can be rewritten as:

$$\frac{\partial A}{\partial t} + \frac{A}{2m}\nabla^2 S = -\nabla A \cdot \nabla S. \tag{2.54}$$

Plugging this relation back into equation (2.52) and bringing all the terms containing S to the left hand side, one obtains:

$$\frac{1}{m}\frac{\partial S}{\partial t} + \frac{(\nabla S)^2}{2m^2} = -c^2 V + \frac{\hbar^2}{2m^2}\frac{\nabla^2 A}{A}. \tag{2.55}$$

which upon taking a gradient becomes:

$$\frac{1}{m}\frac{\partial(\nabla S)}{\partial t} + \frac{1}{m^2}\left(\nabla S \cdot \nabla\right)\nabla S = -\nabla\left(c^2 V - \frac{\hbar^2}{2m^2}\frac{\nabla^2 A}{A}\right). \tag{2.56}$$

By defining a velocity vector, $\mathbf{v}$, to be:

$$\mathbf{v} \equiv \frac{\mathbf{j}}{\rho} = \frac{\nabla S}{m} \tag{2.57}$$

one obtains a form of Euler's equation from the Schrödinger equation:

$$\frac{\partial \mathbf{v}}{\partial t} + \left(\mathbf{v} \cdot \nabla\right)\mathbf{v} = -\nabla\left(V - \frac{\hbar^2}{2m^2}\frac{\nabla^2 \rho^{\frac{1}{2}}}{\rho^{\frac{1}{2}}}\right) \tag{2.58}$$

where the quantity $-(\hbar^2/2m^2)\nabla^2\rho^{\frac{1}{2}}/\rho^{\frac{1}{2}}$ can be viewed as an internal pressure potential. So one sees that the dynamics of a massive scalar field coupled with Newtonian gravity can be studied from a hydrodynamic viewpoint by solving equations (2.49) and (2.58). However, one of the goals of this dissertation is to give a very efficient way of solving (1.1) and (1.2) and then interpret the results from a hydrodynamic perspective.

One thing one might say about this analogy is that the "Schrödinger fluid" appears irrotational because the velocity field is the gradient of a real

valued function. This is only partially true for the complex scalar field as can be seen when the scalar field is given an initial angular boost:

$$\phi(\mathbf{x}, 0) = A(\mathbf{x}, 0)e^{i\frac{S(\mathbf{x}, 0)}{\hbar}}e^{iN\varphi} \tag{2.59}$$

where φ is the usual azimuthal angle in spherical-polar coordinates. Thus, this defines an initial state with a z-component of angular momentum. The gradient of this quantity is:

$$\nabla\phi = e^{i\frac{S}{\hbar}}e^{iN\varphi}\nabla A + \frac{i}{\hbar}Ae^{i\frac{S}{\hbar}}e^{iN\varphi}\nabla S + \frac{iNAe^{i\frac{S}{\hbar}}e^{iN\varphi}}{r\sin\theta} \tag{2.60}$$

where r and θ are the usual spherical-polar coordinates. This allows one to write ∇S as:

$$\nabla S = \hbar\frac{\nabla\phi}{\phi} + i\hbar\frac{\nabla A}{A} - \hbar\frac{N}{r\sin\theta}. \tag{2.61}$$

Thus, the line integral of the velocity field around any closed contour C is:

$$\oint_C \mathbf{v}(\mathbf{x}, 0) \cdot d\mathbf{s} = \oint_C \frac{\nabla S(\mathbf{x}, 0)}{m} \cdot d\mathbf{s} = \frac{\hbar}{m}\oint_C \left(\nabla(\ln\phi) + i\nabla(\ln A) - \frac{n\hat{\varphi}}{r\sin\theta}\right) \cdot d\mathbf{s} \tag{2.62}$$

Because the first two terms in the right most integral are gradients of real valued functions, their line integral about the contour C will be zero which one can see from Stoke's theorem[25]. Thus the contour integral is:

$$\oint_C \mathbf{v}(\mathbf{x}, 0) \cdot d\mathbf{s} = -\frac{2\pi N\hbar}{m} \tag{2.63}$$

The quantity N must be an integer and $\phi = 0$ at the origin in order that ϕ be single valued. So when $n = 0$, the velocity field *is* irrotational. When $n \neq 0$, the velocity field can have rotations which are quantized. These phenomena are called quantized whirlpools and were first discussed by Dirac in his classic paper on magnetic monopoles.[14] and have subsequently received more detailed study. [56, 46, 62, 22] More about these whirlpools will be discussed in chapter 5.

Chapter 3

Finite Difference Solutions

Before delving into how to numerically solve (1.1) and (1.2), I wish to make a change of variables for simplification purposes by performing the following changes of the actual physical independent and dependent variables to variables used in computational solutions:

$$\left(\frac{mc}{\hbar}\mathbf{x}_{phys}, \frac{mc^2}{\hbar}t_{phys}\right) \;\rightarrow\; (\mathbf{x}_{comp}, t_{comp}) \tag{3.1}$$

$$\frac{\sqrt{4\pi G}}{c^2}\phi_{phys} \;\rightarrow\; \phi_{comp} \tag{3.2}$$

where m is the mass of the scalar particle. Thus, in terms of the computational variables, the physical variables have values:

$$\mathbf{x}_{phys} \;=\; 3.518 \times 10^{-38}\frac{\text{g cm}}{m}\,\mathbf{x}_{comp} \tag{3.3}$$

$$t_{phys} \;=\; 1.173 \times 10^{-48}\frac{\text{g s}}{m}\,t_{comp} \tag{3.4}$$

$$\phi_{phys} \;=\; 9.816 \times 10^{23}\frac{\text{g}^{\frac{1}{2}}\ \text{cm}^{\frac{1}{2}}}{\text{s}}\,\phi_{comp} \tag{3.5}$$

So one sees that the computational variables are truly unitless. Dropping the *comp* subscript, the time dependent Schrödinger equation coupled with Newtonian gravity becomes:

$$\frac{\partial \phi}{\partial t} \;=\; i\left(\frac{\nabla^2}{2} - V\right)\phi \tag{3.6}$$

$$\nabla^2 V \;=\; \phi\phi^* \tag{3.7}$$

22

These equations have the boundary conditions:

$$\lim_{r \to \infty} \phi = 0 \tag{3.8}$$

$$\lim_{r \to \infty} V = -\frac{C}{r} \tag{3.9}$$

where $r \equiv |\mathbf{x}|$ and C is some positive constant. Since the density is proportional to $\phi\phi^*$, in these units the density will be defined as equal to $\phi\phi^*$. These variables will be used throughout the rest of this dissertation except in the last chapter where I will perform simulations of phenomena that might have actually occurred in our universe. Before delving into numerical solutions of (3.6) and (3.7), one might wonder how interesting initial data can be generated for these equations and so that is where this chapter begins.

3.1 Generation of Initial Data

Since one of the main motivations of this dissertation is to computationally study boson stars, I need a way to generate density profiles, which are compact and stationary when evolved by equation (3.6) and subject to the self gravitating condition of equation (3.7). This can be done by imposing spherical symmetry and assuming time independence for equations (3.6) and (3.7). Doing this, one obtains the spherically symmetric eigenvalue problem:

$$E\phi = \frac{1}{2r^2}\frac{\partial}{\partial r}\left(r^2\frac{\partial \phi}{\partial r}\right) - V\phi \tag{3.10}$$

$$\frac{1}{r^2}\frac{\partial}{\partial r}\left(r^2\frac{\partial V}{\partial r}\right) = \phi\phi^*. \tag{3.11}$$

To obtain a static compact density distribution when evolved by equations (3.6) and (3.7), solve equations (3.10) and (3.11) for the eigenvalue E of the lowest

eigenstate. These equations can be put into the form of four coupled first order ODEs: [1]

$$
\begin{aligned}
\frac{\partial \phi}{\partial r} &= \frac{1}{r^2} \phi' \\
\frac{\partial \phi'}{\partial r} &= 2r^2 \left(E + V \right) \phi \\
\frac{\partial V}{\partial r} &= \frac{1}{r^2} V' \\
\frac{\partial V'}{\partial r} &= r^2 \rho = r^2 \phi \phi^*
\end{aligned}
\tag{3.12}
$$

where ϕ' and V' are variables and, given $\phi(r = 0)$, solved to high accuracy using a Runge-Kutta method. [63] To find E, make an initial guess and repeat the solution of (3.12) refining the guess of E to machine accuracy subject to the boundary conditions (3.8) and (3.9). As there are numerous free software packages to solve ODEs using the Runge-Kutta method, [24] there is no need to discuss how these equations are solved. A typical solution of (3.12) for ρ and V is shown in figures (3.1) and (3.2). As one can see, the density drops off towards zero from a central peak while the potential is what you would expect for the density distribution ($\phi \phi^*$) shown in the previous figure. Thus by interpolating the numerical solution of the above spherically symmetric eigenvalue problem into three dimensions, one can generate initial data for the numerical solution of (3.6) and (3.7) whose density distribution should remain nearly static. When sets of spherically symmetric static data found from solving equations (3.10) and (3.11) are placed on a three dimensional grid as initial data and evolved, one can observe the interactions of boson stars in the Newtonian regime. Since

---

[1] ordinary differential equations
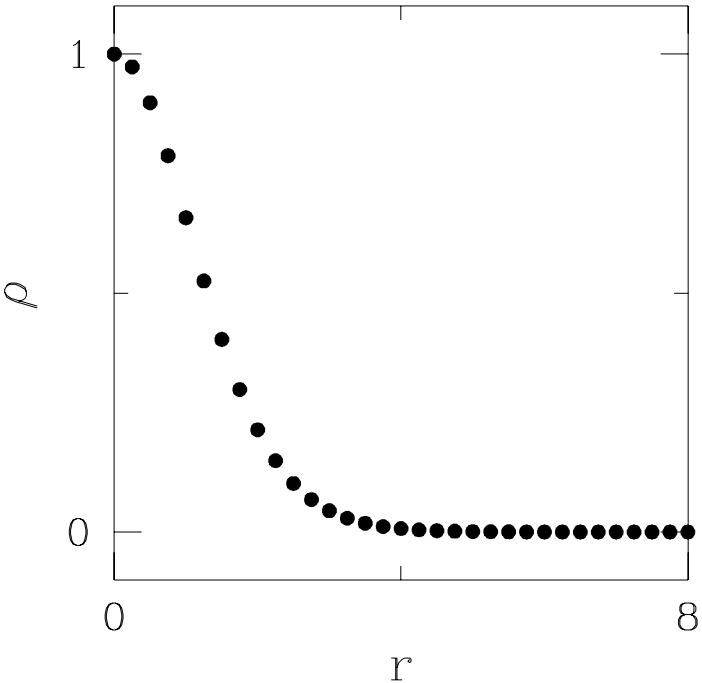
Figure 3.1: A typical density ρ from solution of the eigenvalue problem.
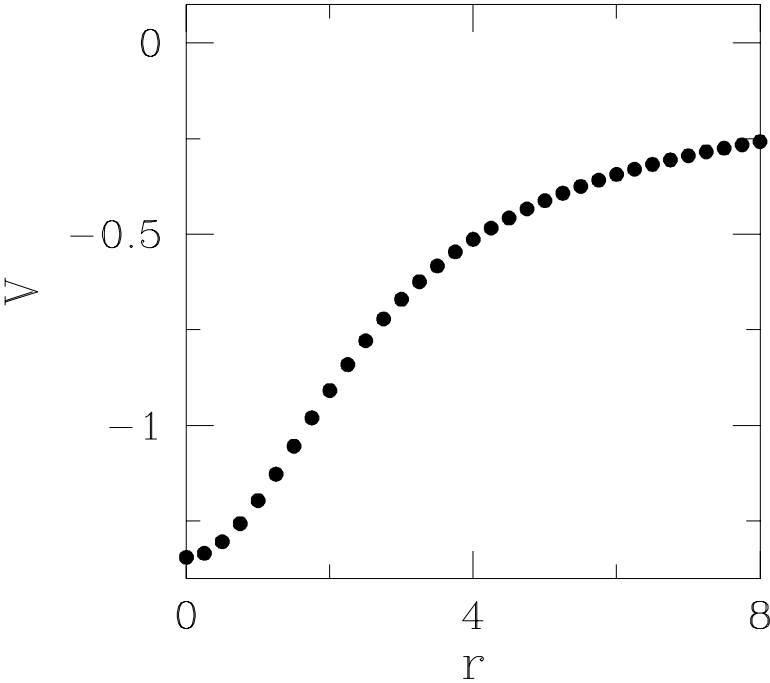
Figure 3.2: A typical potential V from solution of the eigenvalue problem.

the Schrödinger wave function has the property:

$$< \phi^* \left(\mathbf{x}, t \right) - i \nabla \phi \left(\mathbf{x}, t \right) >= \mathbf{p} \tag{3.13}$$

where $\mathbf{p}$ is the average momentum of the field, one can add to the average momentum of the initial data simply by convolving $\phi(\mathbf{x}, t)$ with $\exp(i\mathbf{p} \cdot \mathbf{x})$ as one sees that:

$$- i \nabla \left(\phi \left(\mathbf{x}, t \right) \exp^{i\mathbf{p} \cdot \mathbf{x}} \right) = \exp^{i\mathbf{p} \cdot \mathbf{x}} \left(-i\nabla + \mathbf{p} \right) \phi \left(\mathbf{x}, t \right) \tag{3.14}$$

Thus the initial data for each boson star can be given arbitrary linear momentum. As shown in the last section of chapter 2, one can add angular momentum in quantized increments by convolving the scalar field, $\phi(\mathbf{x}, t)$, with $\exp(iN\varphi)$ where $N = 0, \pm 1, \pm 2, \ldots$.

3.2   Finite Difference Equations

As discussed in the first chapter, there is a need to solve equations (3.6) and (3.7) by the most efficient means possible. For Poisson's equation this suggests the use of multigrid [4, 59] which for N grid points generally takes $O(N)$ floating point operations to solve. I use a multigrid routine written by Matthew Choptuik and enhanced by Scott Klasky for Neumann boundary conditions to solve a centered difference form [40] of equation (3.7).[2] Although multigrid has optimal efficiency, in these days of vector supercomputers, it seems that to many people[3] the computational speed of an algorithm [4] is the algorithms most important aspect. In defense of this, Choptuik's multigrid routine runs

---

[2] An elaborate pseudocode for multigrid can be found in [28].

[3] Especially those deciding on allocation times for supercomputer usage.

[4] Usually measured in floating point operations per second

at about 200 Megaflops out of a possible 1 Gigaflop on the Cray C90 for a 129^3 grid which is a respectable speed especially for multigrid. Another way to enhance the computational time of multigrid is by using parallel computers. Scott Klasky and I developed an algorithm for this which is discussed in [28].

The method used for solving equation (3.6) had two motivations. One concerns instability [31, 30] which for centered difference schemes can occur if the time step is too large in comparison to the spatial mesh width. The other motivation is to use a method with optimal efficiency. Choptuik and I chose a method that has unconditional stability and takes O(N) steps to solve. To begin one notes from Taylor series expansion that formally equation (3.6) can be written:

$$\phi\left(\mathbf{x}, t + \lambda h\right) = e^{i\lambda h D}\phi\left(\mathbf{x}, t\right) \qquad (3.15)$$

where h is the spatial mesh width of the finite difference mesh, λ is a constant proportionality factor relating the spatial mesh size to temporal mesh size, and $D = \nabla^2/2 - V$. Multiplying by $\exp(-i\lambda h t D/2)$ this becomes:

$$e^{-\frac{i}{2}\lambda h D}\phi\left(\mathbf{x}, t + \lambda h\right) = e^{\frac{i}{2}\lambda h D}\phi\left(\mathbf{x}, t\right) \qquad (3.16)$$

If this equation were expanded and put into second order centered difference form now it would be a Crank-Nicholson type equation [40] and would require a seven banded diagonal solver. For n points per edge of the difference grid and a total of n^3 grid points, the bandwidth of the solver would be $O(n^2)$ and thus could be quite large in comparison to the matrix formed from the three dimensional plus time difference equations. Thus the method would be an inefficient way to solve (3.6). One sees that equation (3.16) can be written

in the form:

$$e^{-\frac{i\lambda h}{4}\frac{\partial^2}{\partial x^2}}e^{-\frac{i\lambda h}{4}\frac{\partial^2}{\partial y^2}}e^{-\frac{i\lambda h}{4}\frac{\partial^2}{\partial z^2}}e^{\frac{i\lambda h}{2}V}\phi\left(\mathbf{x},t+\lambda h\right) = e^{\frac{i\lambda h}{4}\frac{\partial^2}{\partial x^2}}e^{\frac{i\lambda h}{4}\frac{\partial^2}{\partial y^2}}e^{\frac{i\lambda h}{4}\frac{\partial^2}{\partial z^2}}e^{-\frac{i\lambda h}{2}V}\phi\left(\mathbf{x},t\right)+O\left(\lambda^3 h^3\right)$$
(3.17)

where the error term arises because the potentaial V does not commoute with the partial derivatives. This equation can be broken up into four equations:

$$e^{-\frac{i\lambda h}{4}\frac{\partial^2}{\partial x^2}}S\left(\mathbf{x}\right) = e^{\frac{i\lambda h}{4}\frac{\partial^2}{\partial x^2}}\phi\left(\mathbf{x},t\right)$$
(3.18)

$$e^{-\frac{i\lambda h}{4}\frac{\partial^2}{\partial y^2}}T\left(\mathbf{x}\right) = e^{\frac{i\lambda h}{4}\frac{\partial^2}{\partial y^2}}S\left(\mathbf{x}\right)$$
(3.19)

$$e^{-\frac{i\lambda h}{4}\frac{\partial^2}{\partial z^2}}U\left(\mathbf{x}\right) = e^{\frac{i\lambda h}{4}\frac{\partial^2}{\partial z^2}}T\left(\mathbf{x}\right)$$
(3.20)

$$e^{\frac{i\lambda h}{2}V}\phi\left(\mathbf{x},t+\lambda h\right) = e^{-\frac{i\lambda h}{2}V}U\left(\mathbf{x}\right).$$
(3.21)

Now, in second order centered difference form the second partial derivative of x can be written:

$$\frac{\partial^2}{\partial x^2} = \frac{1}{h^2}\left(\delta_x^2 - \frac{1}{12}\delta_x^4 + \frac{1}{90}\delta_x^6\ldots\right)$$
(3.22)

where δ_x^2 is the second order central density operator defined by:

$$\delta_x^2 f(x) = f(x+h) - 2f(x) + f(x-h)$$
(3.23)

Replacing the parital derivatives with the first term in the expansion equation (3.22), expanding the exponentials of equations (3.18)-(3.21) to lowest significant order in h, and replacing the continuous notation of the variables with discretized notation, one obtains:

$$\left(1 - \frac{i\lambda}{4h}\delta_i^2\right)S_{ijk} = \left(1 + \frac{i\lambda}{4h}\delta_i^2\right)\phi_{ijk}^n$$
(3.24)

$$\left(1 - \frac{i\lambda}{4h}\delta_j^2\right)T_{ijk} = \left(1 + \frac{i\lambda}{4h}\delta_j^2\right)S_{ijk}$$
(3.25)

$$\left(1 - \frac{i\lambda}{4h}\delta_k^2\right)U_{ijk} = \left(1 + \frac{i\lambda}{4h}\delta_k^2\right)T_{ijk}$$
(3.26)

$$\left(1 + \frac{i\lambda h}{2}V_{ijk}^{n+\frac{1}{2}}\right)\phi_{ijk}^{n+1} = \left(1 - \frac{i\lambda h}{2}V_{ijk}^{n+\frac{1}{2}}\right)U_{ijk}$$
(3.27)

where:

$$\phi_{ijk}^n = \phi(x_o + ih, y_o + jh, z_o + kh, n\lambda h) = \phi(\mathbf{x}, t). \tag{3.28}$$

$V_{ijk}^{n+\frac{1}{2}}$ is used because, we wanted to have the difference equations in Crank-Nicolson form[40] so that they would be unconditionally stable [31, 30]. These are the difference evolution equations of (3.6) in ADI form where given ϕ_{ijk}^n one can use a tridiagonal solver to find the update function, ϕ_{ijk}^{n+1}. Since the computational domain can not cover an infinite physical domain, it is assumed that ϕ_{ijk}^n is nearly zero around the outer boundaries and thus one can use extrapolation boundary conditions with the above difference equations:

$$\phi_{0jk}^n = 2\phi_{1jk}^n - \phi_{2jk}^n \tag{3.29}$$

$$\phi_{I+1jk}^n = 2\phi_{Ijk}^n - \phi_{I-1jk}^n \tag{3.30}$$

with similar equations for the left and right j and k boundaries. $V_{ijk}^{n+\frac{1}{2}}$ is found by the $O(\lambda^2 h^2)$ extrapolation:

$$V_{ijk}^{n+\frac{1}{2}} = \frac{3}{2}V_{ijk}^n - \frac{1}{2}V_{ijk}^{n-1} \tag{3.31}$$

as one can find the potential, V, at the n and $n-1$ time steps from solving the multigrid solution to (3.7) using ϕ_{ijk}^n and ϕ_{ijk}^{n-1} respectively.

On vector supercomputers, tridiagonal solvers do not vectorize well because when computing the solution $\mathbf{u}$ to a given tridiagonal matrix problem $A\mathbf{u} = \mathbf{b}$, the computation of u_i depends on u_{i-1} and thus the *flops* are relatively small compared to other methods for solving linear equations. The vectorization of these routines can be improved by writing a tri-diagonal solver that solves an array of lines rather than one line at a time which is referred to as inilining.[11] The inlined tridiagonal solver runs almost five times faster on the

Cray C90 than the specially written tridiagonal solver written for Cray vector supercomputers and improved the speed for the solution of (3.24)-(3.27) by a factor of 3 for 129^3 grids. A new method for parallelizing the ADI method using a one dimensional multigrid technique will be discussed in a currently unpublished paper[21] and other methods can be found in the following references[57, 16].

A particular solution of equations (3.24)-(3.27) coupled with the multigrid solution of V^n_{ijk} is shown in one dimensional movie form in figures 3.3-3.6. Initial data was generated for a single boson star with a central density of 1 centered in a 129^3 spatial mesh with spatial width of 32.0 in the x, y and z directions.[5] Each spatial frame displays 65 points of spherically symmetric data with a domain from $r = 0.0$ to $r = 8.0$ with the data being interpolated from the three dimensional calculation. Each movie starts in the upper left corner at $t = 0.0$ and proceeds from left to right and top to bottom in time increments of 0.5 to a final time of 19.5 in the lower right corner. The range of figures 3.3 and 3.4 which show the evolution of the real and imaginary parts of ϕ goes from -1.0 to 1.0. These movies show that for the given initial data the scalar field simply oscillates at a constant frequency with the imaginary part of ϕ remaining 90 degrees behind in phase from the real part of ϕ.

Figure 3.5 for the density $\phi\phi^*$ has a range from 0.0 to 1.1. It shows that the density remains relatively constant with slight perturbations around the initial distribution which can be seen from this movie by looking closely at the changes at the central point ($r = 0$) of each time frame. This is to be expected

---

[5] Remember that the spatial, temporal, ϕ and V computational units are all dimensionless
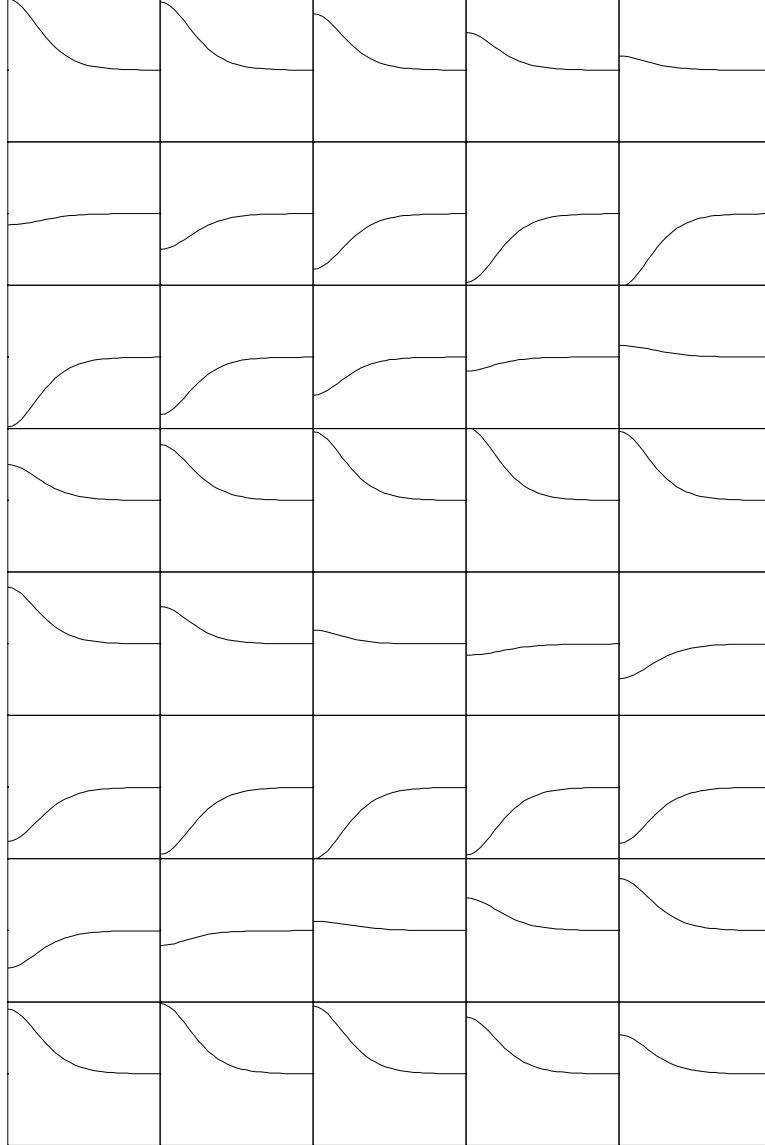
Figure 3.3: Time evolution of the real part of the scalar field ϕ. Limits: computational domain $(x, y, z:$ -8 to 8); frame domain (r: 0 to 8); frame range $(\phi_{real}$: -1 to 1).
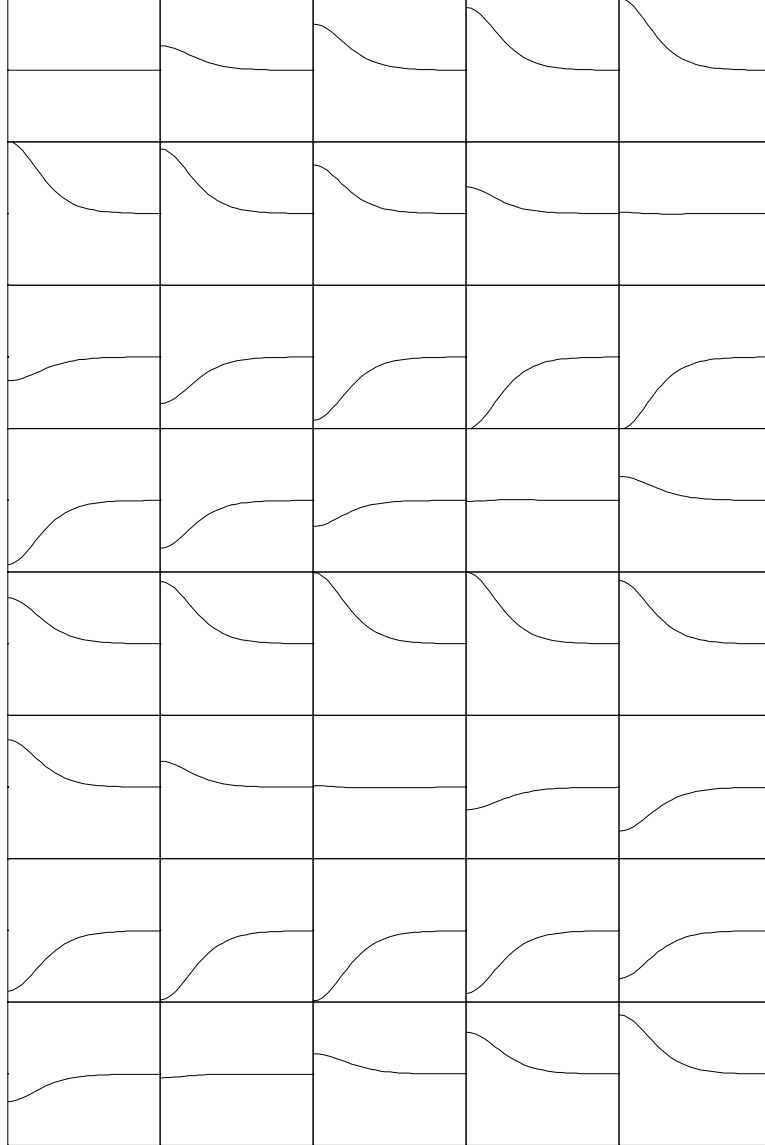
Figure 3.4: Time evolution of the imaginary part of the scalar field ϕ. Limits: computational domain $(x, y, z$: -8 to 8); frame domain $(r$: 0 to 8); frame range $(\phi_{imaginary}$: -1 to 1).
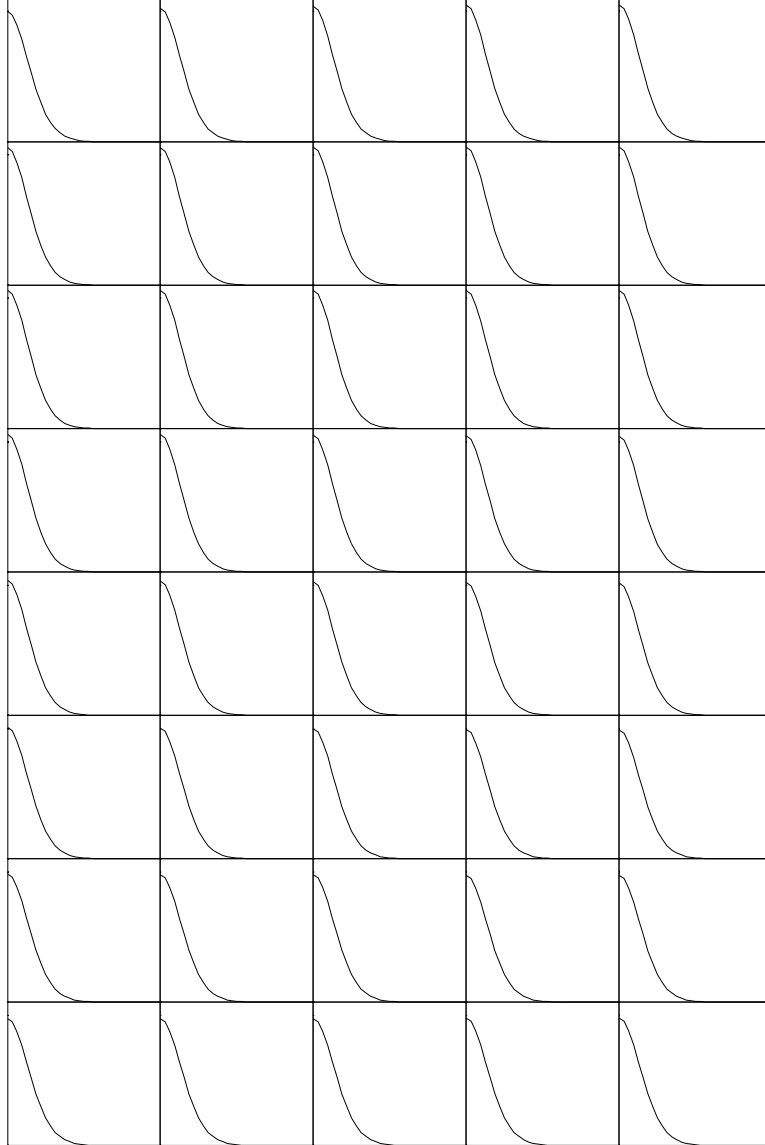
Figure 3.5: Time evolution of the density of the scalar field $\phi\phi^*$. Limits: computational domain $(x, y, z$: -8 to 8); frame domain $(r$: 0 to 8); frame range $(\phi\phi^*$: 0 to 1.1).
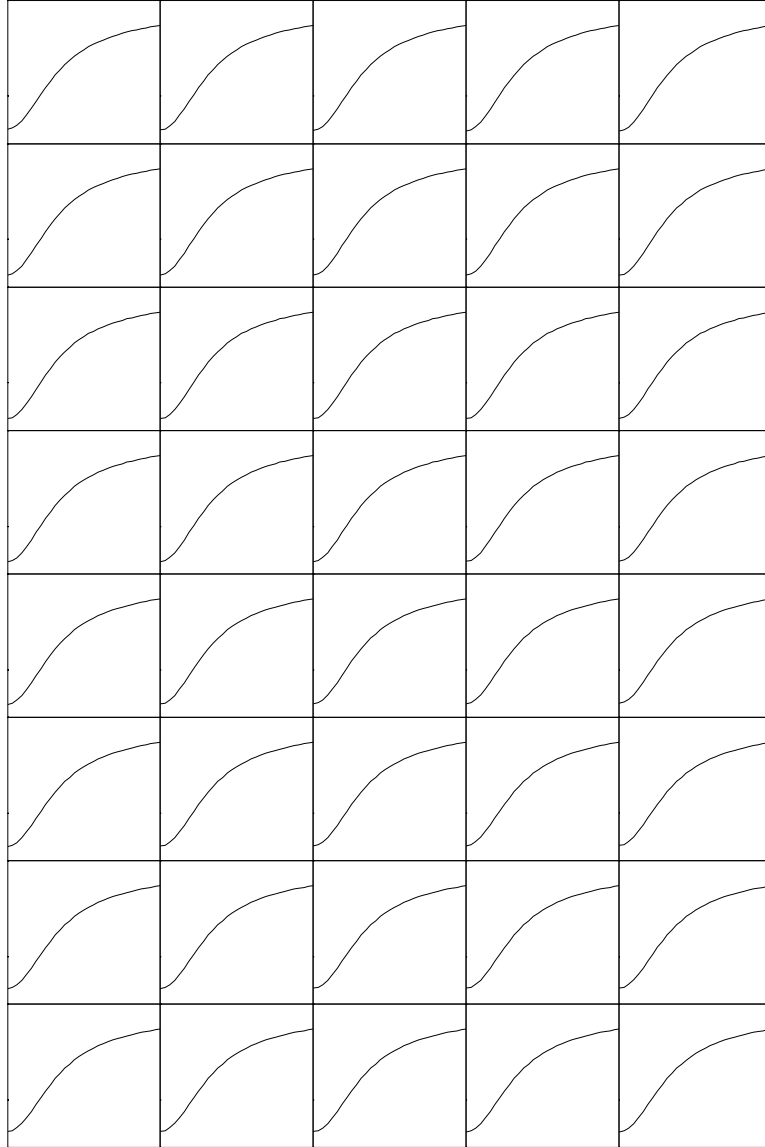
Figure 3.6: Time evolution of the Newtonian potential V. Limits: computational domain (x, y, z: -8 to 8); frame domain (r: 0 to 8); frame range (V: -1.5 to 0).

# mesh points	initial mass $t = 0$	final mass $t = 80$	% change in mass	time steps
33^3	$25.9150\cdots$	$25.9147\cdots$	1.3×10^{-3}	160
65^3	$25.915036\cdots$	$25.915001\cdots$	1.2×10^{-4}	320
129^3	$25.9150179\cdots$	$25.9150168\cdots$	4.3×10^{-6}	640
257^3	$25.91502873\cdots$	$25.91502864\cdots$	3.4×10^{-7}	1280

Table 3.1: The results of the evolution of a single boson star with an initial central density of 1.0 centered in a spatial mesh of width 32.0 on a side for a varying number of mesh points.

since the initial data is that of the spherically symmetric eigenvalue problem and thus a proper finite difference time evolution of this solution should give a constant density. The slight oscillation of the density results mainly because of truncation error of the finite difference solution. This situation is somewhat akin to that of a harmonic oscillator solution with a potential slightly perturbed from the bottom of the potential well.

The movie for the solution of the Newtonian potential has a range from -1.5 to 0.0 and shows that V remains relatively constant due to the nearly constant density. Each time frame also shows that the potential is assuming the functional form of $-C/r$ as r goes to infinity which is the form of the Newtonian potential due to a point mass. This is also expected since the density distribution becomes very small (10^{-8}) relative to the central density at $r = 8.0$.

How well a computational solution obeys the conservation laws for the modeled PDEs is considered by many computational scientists to be a good way to check the validity of the computational solution. As shown in section 2.2.3, the time-dependent Schrödinger equation coupled with a Newtonian potential conserves mass. Thus by spatially integrating the density $\left(\phi_{ijk}^n \phi_{ijk}^{n*}\right)$ at the

initial time ($n = 0$) and the final time, one can test how well the difference evolution equations (3.24)-(3.27) conserve mass. The results of the evolution of a single boson star with an initial central density of 1.0 centered in a spatial mesh of width 32.0 on a side for a varying number mesh points are given in table 3.1. The initial and final masses have been computed to machine accuracy for `real*8 FORTRAN` variables on Cray computers[6] and are given at the initial time ($t = 0$) and the final time ($t = 80$). The number of computational steps in each evolution are shown to indicate that the width of the time steps are kept at a constant factor to each spatial mesh width.[7] As the table shows, the largest percentage change in mass is on the order of 10^{-3} for the 33^3 mesh and drops by at least a factor of 9 for each doubling of the mesh point spacing. Superficially, these results appear to indicate that the difference solution models the differential equations quite well even for a 33^3 spatial mesh. As the next section will demonstrate, these results are deceptive and a better way to check the validity of a finite difference solution is through convergence checking.

3.3   Convergence of the Finite Difference Solution

Most of the physicists with whom I have talked distrust numerical solutions of partial differential equations believing that the error of approximation can infect the numerical solution so that results of the simulation do not represent the analytic solution. This myth can be dispelled for finite difference solutions of PDEs by convergence checking [45, 8] in which one shows that in the limit that the grid spacing h goes to zero the finite difference solution should be the

---

[6] `real*8` on Crays have a machine precision of about 14 significant digits.

[7] i.e. $\lambda \equiv \Delta y / h$ is constant for all computations.

same as the analytic solution. Whereas many numerical scientists check their computational solutions by comparing them with an exact solution or by showing that the solution adheres to a conservation law such as mass conservation, a more rigorous test that the general difference solution of a PDE converges to the solution of the PDE[8] is convergence checking. For pedagogical reasons, I will show that the spherically symmetric difference equations of (3.6) and (3.7) converge to the analytic solution. Then I will show that the three dimensional difference solution (3.24)-(3.27) is similar to that of the spherically symmetric solution.

In order to easily satisfy the regularity condition at $r = 0$, the spherically symmetric center difference equations for the Schrödinger equation coupled with Newtonian gravity are generated from the differential equations:

$$\frac{\partial \phi}{\partial t} = \frac{3i}{2} \frac{\partial}{\partial r^3} \left(r^2 \frac{\partial \phi}{\partial r} \right) - iV\phi \tag{3.32}$$

$$3 \frac{\partial}{\partial r^3} \left(r^2 \frac{\partial V}{\partial r} \right) = \phi \phi^* \tag{3.33}$$

The centered difference forms for these equations are:

$$\Delta_+^t \phi_j^n = \frac{i}{2} \left[\alpha_+^r \Delta_+^r \left(\mu_+^t \phi_j^n \right) - \alpha_-^r \Delta_-^r \left(\mu_+^t \phi_j^n \right) \right] - i\chi_+^t V_j^n \, \mu_+^t \phi_j^n \tag{3.34}$$

$$\left(\alpha_r^+ \Delta_+^r - \alpha_-^r \Delta_r^- \right) V_j^n = \phi_j^n \phi_j^{*n} \tag{3.35}$$

where $\alpha_r^\pm, \Delta_+^t$ and $\Delta_r^\pm$ are defined in table 3.2. To find the behavior of the error, one inputs into (3.34) and (3.35) the differential form for the difference operators and the Richardson expansions[45]:

$$\phi_j^n = \phi + h e_{\phi_1} + h^2 e_{\phi_2} + h^3 e_{\phi_3} + O(h^4) \tag{3.36}$$

$$V_j^n = V + h e_{V_1} + h^2 e_{V_2} + h^3 e_{V_3} + O(h^4) \tag{3.37}$$

---

[8]in the limit that the discrete domain approaches the continuum, $h \to 0$.

Differencing Operators:

$$\Delta_{+}^{t} g_{j}^{n} \quad \equiv \quad \frac{g_{j}^{n+1} - g_{j}^{n}}{\lambda h} = \left(\frac{\partial}{\partial t} + \frac{(\lambda h)^{2}}{24} \frac{\partial^{3}}{\partial t^{3}} \right) g_{j}^{n+\frac{1}{2}} + O(h^{4})$$

$$\Delta_{\pm}^{r} g_{j}^{n} \quad \equiv \quad \pm \frac{g_{j\pm1}^{n} - g_{j}^{n}}{h} = \left(\frac{\partial}{\partial x} \pm \frac{h}{2} \frac{\partial^{2}}{\partial x^{2}} + \frac{h^{2}}{6} \frac{\partial^{3}}{\partial x^{3}} \right) g_{j}^{n} + O(h^{3})$$

Averaging and Extrapolating Operators:

$$\mu_{+}^{t} g_{j}^{n} \quad \equiv \quad \frac{g_{j}^{n+1} + g_{j}^{n}}{2} = \left(1 + \frac{(\lambda h)^{2}}{8} \frac{\partial^{2}}{\partial t^{2}} \right) g_{j}^{n+\frac{1}{2}} + O(h^{4})$$

$$\chi_{\pm}^{t} g_{j}^{n} \quad \equiv \quad \frac{3 g_{j}^{n} - g_{j}^{n\mp1}}{2} = \left(1 \mp \frac{3 (\lambda h)^{2}}{8} \frac{\partial^{2}}{\partial t^{2}} \right) g_{j}^{n} + O(h^{4})$$

Variable Definitions:

$$\alpha_{\pm}^{r} \quad \equiv \quad \frac{3 r_{j\pm\frac{1}{2}}^{2}}{r_{j+\frac{1}{2}}^{3} - r_{j-\frac{1}{2}}^{3}} = \frac{1}{h} \pm \frac{1}{r_{j}} + \frac{h}{6 r_{j}^{2}} \mp \frac{h^{2}}{12 r_{j}^{3}} - \frac{h^{3}}{72 r_{j}^{4}} + O(h^{4})$$

$$g_{j}^{n} \quad \equiv \quad g(r_{j}, n\lambda h)$$

$$r_{j} \quad \equiv \quad \left(j - \frac{1}{2} \right) h$$

Table 3.2: Definitions of operators and variables used in the text.

where ϕ and V are the analytic solutions to (3.32) and (3.33) and the $e_{\phi 1}, e_{V1}, \ldots$ are error terms which in the limit $h \to 0$ are independent of h. Since terms of a given order of h are independent of h, one can separate the differential expansion of the difference equations into equations at each order of h:

$$\frac{\partial \phi}{\partial t} - \frac{i}{2}\frac{1}{r^2}\frac{\partial}{\partial r}\left(r^2\frac{\partial \phi}{\partial r}\right) + iV\phi = 0 \tag{3.38}$$

$$\frac{1}{r^2}\frac{\partial}{\partial r}\left(r^2\frac{\partial V}{\partial r}\right) - \phi\phi^* = 0 \tag{3.39}$$

which are the $O(1)$ equations;

$$\frac{\partial e_{\phi_1}}{\partial t} - \frac{i}{2}\frac{1}{r^2}\frac{\partial}{\partial r}\left(r^2\frac{\partial e_{\phi_1}}{\partial r}\right) + iVe_{\phi_1} - ie_{V_1}\phi = 0 \tag{3.40}$$

$$\frac{1}{r^2}\frac{\partial}{\partial r}\left(r^2\frac{\partial e_{V_1}}{\partial r}\right) - \phi^* e_{\phi_1} - \phi e_{\phi_1}^* = 0 \tag{3.41}$$

which are the $O(h)$ equations;

$$\begin{aligned}
\frac{\partial e_{\phi_2}}{\partial t} \quad - \quad & \frac{i}{2}\frac{1}{r^2}\frac{\partial}{\partial r}\left(r^2\frac{\partial e_{\phi_2}}{\partial r}\right) + iVe_{\phi_2} = \\
& \frac{i\lambda^2}{16}\frac{\partial^2}{\partial t^2}\left(\frac{1}{r^2}\frac{\partial}{\partial r}\left(r^2\frac{\partial \phi}{\partial r}\right)\right) + \\
& \frac{i}{24}\frac{\partial^4\phi}{\partial r^4} + \frac{i}{6r}\frac{\partial^3\phi}{\partial r^3} + \frac{i}{12r^2}\frac{\partial^2\phi}{\partial r^2} - \frac{i}{12r^3}\frac{\partial \phi}{\partial r} - \\
& \frac{i\lambda^2}{8}\frac{\partial^2\phi}{\partial t^2}V + \frac{3i\lambda^2}{8}\frac{\partial^2 V}{\partial t^2}\phi - ie_{V_2}\phi - ie_{V_1}e_{\phi_1} \tag{3.42}
\end{aligned}$$

$$\begin{aligned}
\frac{1}{r^2}\frac{\partial}{\partial r}\left(r^2\frac{\partial e_{V_2}}{\partial r}\right) \quad - \quad & \phi^* e_{\phi_2} - \phi e_{\phi_2}^* = e_{\phi_1}e_{\phi_1}^* - \\
& \frac{1}{12}\frac{\partial^4 V}{\partial r^4} - \frac{1}{3r}\frac{\partial^3 V}{\partial r^3} - \frac{1}{6r^2}\frac{\partial^2 V}{\partial r^2} + \frac{1}{6r^3}\frac{\partial V}{\partial r} \tag{3.43}
\end{aligned}$$

which are the $O(h^2)$ equations;

$$\begin{aligned}
\frac{\partial e_{\phi_3}}{\partial t} \quad - \quad & \frac{i}{2}\frac{1}{r^2}\frac{\partial}{\partial r}\left(r^2\frac{\partial e_{\phi_3}}{\partial r}\right) + iVe_{\phi_3} = \\
& \frac{i}{24}\frac{\partial^4 e_{\phi_1}}{\partial r^4} + \frac{i}{6r}\frac{\partial^3 e_{\phi_1}}{\partial r^3} + \frac{i}{12r^2}\frac{\partial^2 e_{\phi_1}}{\partial r^2} - \frac{i}{12r^3}\frac{\partial e_{\phi_1}}{\partial r} -
\end{aligned}$$

$$\frac{i\lambda^2}{8}\frac{\partial^2 e_{\phi_1}}{\partial t^2} - i\phi\left(e_{V_3} - \frac{3\lambda^2}{8}\frac{\partial^2 e_{V_1}}{\partial t^2}\right) -$$

$$ie_{\phi_1}\left(e_{V_2} - \frac{3i\lambda^2}{8}\frac{\partial^2 V}{\partial t^2}\right) - ie_{V_1}\left(\frac{\lambda^2}{8}\frac{\partial^2 \phi}{\partial t^2} + ie_{\phi_2}\right) -$$

$$\frac{\lambda^2}{24}\frac{\partial^2 e_{\phi_1}}{\partial t^2} + \frac{i\lambda^2}{16}\frac{\partial^2}{\partial t^2}\left(\frac{1}{r^2}\frac{\partial}{\partial r}\left(r^2\frac{\partial e_{\phi_1}}{\partial r}\right)\right) \qquad (3.44)$$

$$\frac{1}{r^2}\frac{\partial}{\partial r}\left(r^2\frac{\partial e_{V_3}}{\partial r}\right) \quad - \quad e_{\phi_1}e_{\phi_2}^* - e_{\phi_1}^* e_{\phi_2} = \phi e_{\phi_3}^* + \phi^* e_{\phi_3} -$$

$$\frac{1}{12}\frac{\partial^4 e_{V_1}}{\partial r^4} - \frac{1}{3r}\frac{\partial^3 e_{V_1}}{\partial r^3} - \frac{1}{6r^2}\frac{\partial^2 e_{V_1}}{\partial r^2} + \frac{1}{6r^3}\frac{\partial e_{V_1}}{\partial r} \qquad (3.45)$$

which are the $O(h^3)$ equations. As one sees, the $O(1)$ equations are just the original differential equations .[9] Assuming that there is no error in the initial data for the difference equations,[10] the $O(h)$ and $O(h^3)$ equations which have no sources from lower order nonzero terms show that the errors $e_{\phi 1}, e_{V 1}, e_{\phi 3}$ and $e_{V 3}$ will remain identically zero. The same sort of pattern is inherent in all the odd order equations and thus all the odd order errors will remain identically zero. This is what Richardson posited in 1910 for the solution of centered difference approximations to PDEs [45], and thus solutions to centered difference equations will have the form:

$$u_j^n = u + h^2 e_{u_2} + h^4 e_{u_4} + O(h^6). \qquad (3.46)$$

The even order h equations show that the equations for the even order errors are the same as the original differential equations except that they have driving terms dependent on ϕ, V and lower order errors. Thus the errors should behave in a similar manner as that of ϕ and V. One can compute an estimate of this error by comparing center difference finite difference solutions using different

---

[9] i.e. the difference system is consistent.
[10] i.e. $e_{\phi_m}(r, t = 0) = e_{V_m}(r, t = 0) = 0$ for $m = 1, 2, 3, \ldots$

mesh widths, usually h and $2h$:

$$e_{\phi_2} = \frac{\phi_{2h} - \phi_h}{3h^2} - 5h^2 e_{\phi_4} + O(h^4) \tag{3.47}$$

This *truncation error estimate* is the basis of Berger and Oliger's AMR technique [3, 7]. Another useful quantity one can compute from the expansions of the finite difference solutions is the test for second order convergence of the finite difference solution at a given time:

$$T_{convg}\left(u_{h_1}, u_{h_2}, u_{h_3}; h_1, h_2, h_3, t\right) \equiv \frac{|u_{h_3} - u_{h_2}|}{|u_{h_2} - u_{h_1}|} - \frac{(h_3^2 - h_2^2)}{(h_2^2 - h_1^2)} = O(h^2) \tag{3.48}$$

where the terms in $|\ |$ are the spatial norms of the difference of two numerical solutions at a given time using different size hs.[11] Since this is only true in the limit $h \to 0$, the centered difference equations (3.34) and (3.35) should only approximate this equation, but the approximation improves as one decreases the size of h. Thus given three finite difference solutions with varying h at particular times one can check the convergence of one's finite difference equations by showing that T_{convg} approaches zero as h_1, h_2, and $h_3 \to 0$.

Figures 3.7-3.11 give a comparison of this convergence factor for the spherically symmetric, (3.34) and (3.35), and the general three dimensional difference solutions, equations (3.24)-(3.27), to the time dependent Schrödinger equation coupled with Newtonian gravity. The spherically symmetric and three dimensional solutions start with the same initial data for a single boson star with central density of 1.0 and T_{convg} computed at 80 times from $t = 1.0$ to $t = 80.0$ for varying ratios of the spatial grid spacing h. A spherically symmetric difference solution with 17 spatial mesh points covering from $r = 0$ to

---

[11] $h_1 = n_1 h$, $h_2 = n_2 h$ and $h_3 = n_3 h$ where n_1, n_2 and n_3 are natural numbers.

$r = 16$ will have a comparable three dimensional solution with equivalent mesh spacing but 33^3 spatial mesh points since the spherically symmetric initial data is centered in the three dimensional grid. Thus since the spherically symmetric solutions have a spatial mesh width of 16, the three dimensional solutions have a mesh width of 32 in the x, y and z dimensions.

Figure 3.7 shows the spherically symmetric results of T_{convg} for increasingly finer values of h_1, h_2 and h_3 at varying times. As the figure shows T_{convg} appears to have an almost random distribution within the plot box. This indicates that the errors of the spherically symmetric finite difference equations are dominated by the higher order error terms than the $O(h^2)$ errors. In figure 3.8 the points for the coarser set of hs still oscillate but in a more consistent pattern than in the previous figure. The T_{convg} with the finest set of hs does settle around zero which indicates that the the difference scheme is converging to the continuum solution. In figure 3.9, one can see that the T_{convg}s grow closer to zero for finer sets of hs. The spurious points off of the zero line are due to when the real part of ϕ is near a zero crossing in the oscillation. This causes the numerator of the first term with | |s in (3.48) to be artificially too large or the denominator to be too small and thus give an incorrect value for T_{convg}. This is also complicated by the different oscillation frequencies of the difference solution for different values of h also caused by errors in the difference solution.

Looking at the three dimensional results in figure 3.10, the T_{convg} with the coarsest set of hs appears to be even worse than the comparable spherically symmetric results in figure 3.7. This is expected since there is an order h^3 error term introduced in the three dimensional ADI solution since the potential V does not commute with the finite difference operators. The T_{convg} for the coars-

est set of hs in figure 3.10 is for evolution runs with 33^3, 65^3 and 129^3 spatial mesh points and shows that the conclusions from the mass conservation results in table 3.1 that the solution of the difference equations for these mesh sizes are close to the differential solution are misleading. The T_{convg}s for finer sets of h do appear to be approaching zero, and figure 3.11 shows that this is definitely true. One would like to show three dimensional results which are similar to the spherically symmetric results shown in figure 3.9 but unfortunately in three dimensions one quickly runs into memory problems so that a 257^3 spatial grid is the largest grid able to be implemented for this problem on the Cray C90 at the Pittsburgh Supercomputing Center.

Similar results were found for the imaginary part of the scalar field as well as the Newtonian potential. Thus the difference equations are shown to be consistent with there differential equations for the given initial data and on the given spatial mesh width for finest spatial meshes. This could not be demonstrated for any of the three dimensional solutions if one doubles the mesh width even the 257^3 solution since the single star could not be very well resolved for an $h = 0.25$ and thus the higher order error terms would dominate the difference solution. This problem can be solved by using adaptive meshing which will allow one to resolve very compact objects on a large domain. Also one might wonder what happens when two stars collide or the initial data for a single star is given momentum and the subsequent evolution causes it to collide with the computational boundary. In both cases a large amount of matter comes in contact with the boundaries which invalidates the extrapolation boundary conditions used in equations (3.24)-(3.27) and the boundary condition for the potential equation, $V = -C/r$. In these cases, absorbing boundary condi-

tions similar to those used by Israeli and Orszag [23] for the wave equation are needed. Luckily, the implementation of these boundary conditions turn out to be quite simple and robust. The implementation of these boundary conditions are discussed in the next chapter.
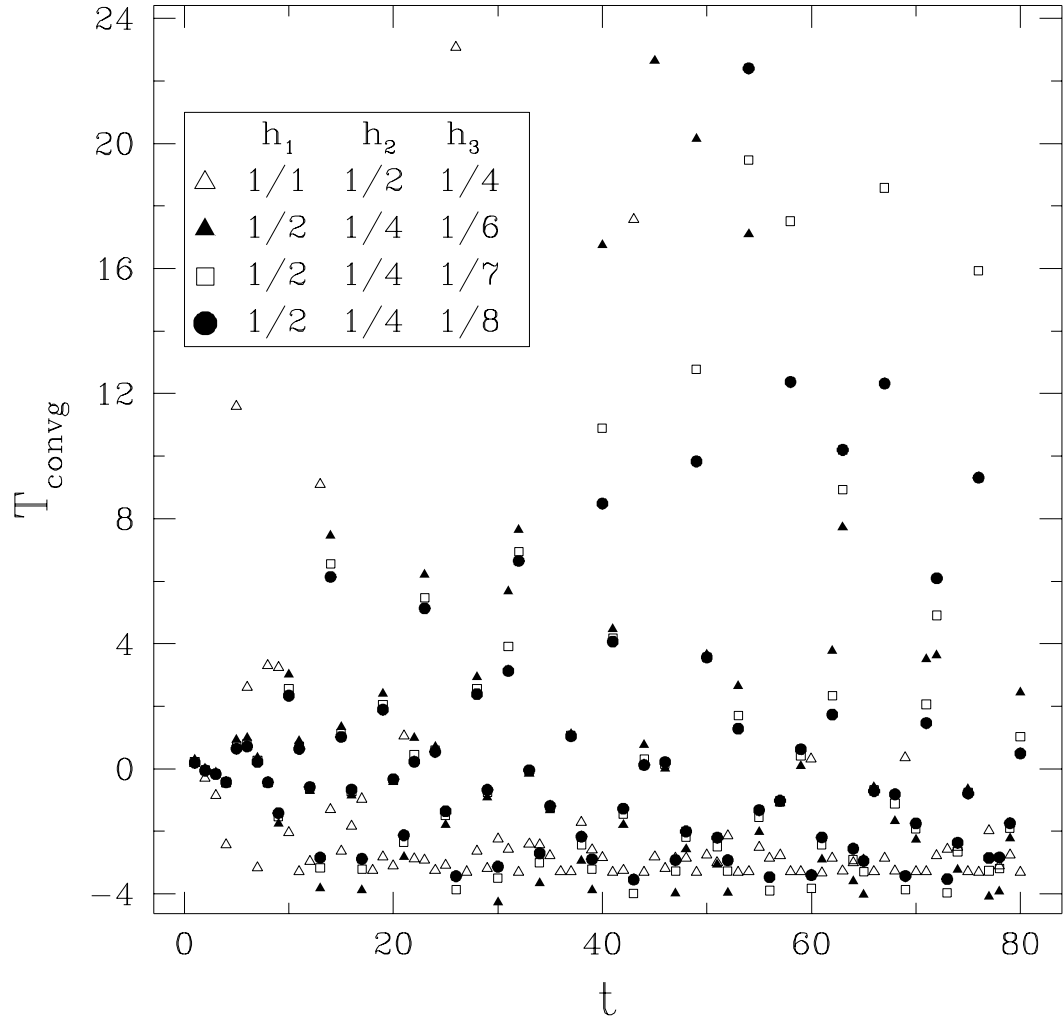
Figure 3.7: Convergence factors, T_{convg}, for the real part of the scalar field ϕ from the solution of the spherically symmetric difference equations.
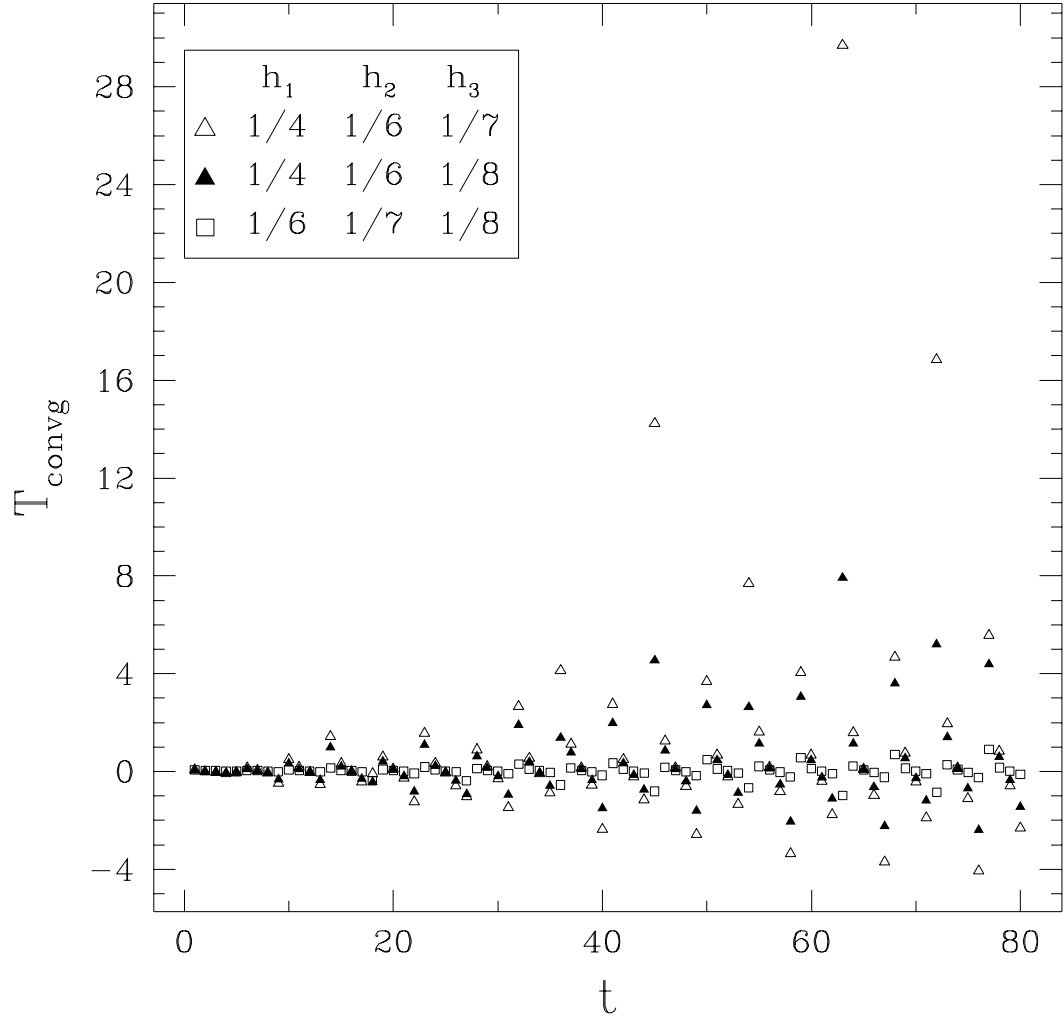
Figure 3.8: Convergence factors, T_{convg}, for the real part of the scalar field ϕ from the solution of the spherically symmetric difference equations.
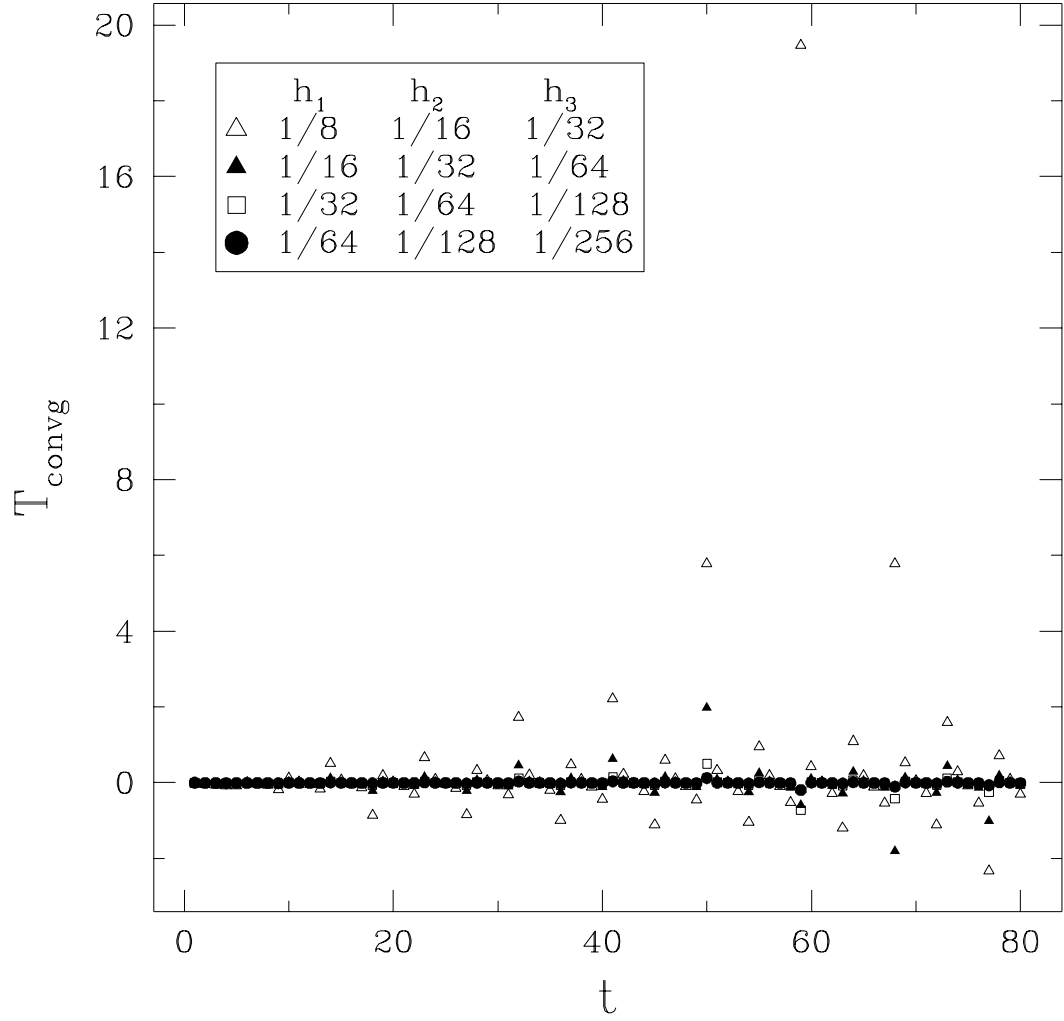
Figure 3.9: Convergence factors, T_{convg}, for the real part of the scalar field ϕ from the solution of the spherically symmetric difference equations.

48
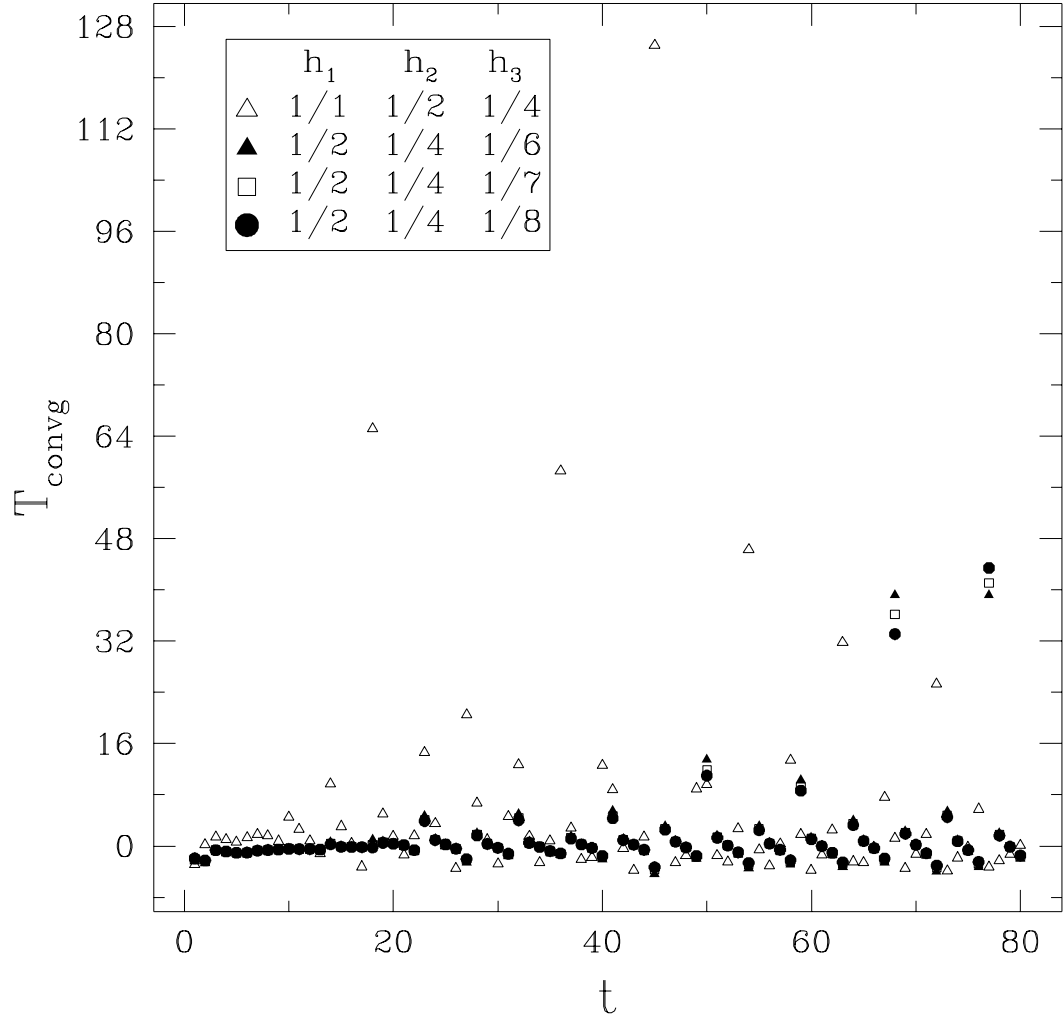
Figure 3.10: Convergence factors, T_{convg}, for the real part of the scalar field ϕ from the solution of the three dimensional difference equations.
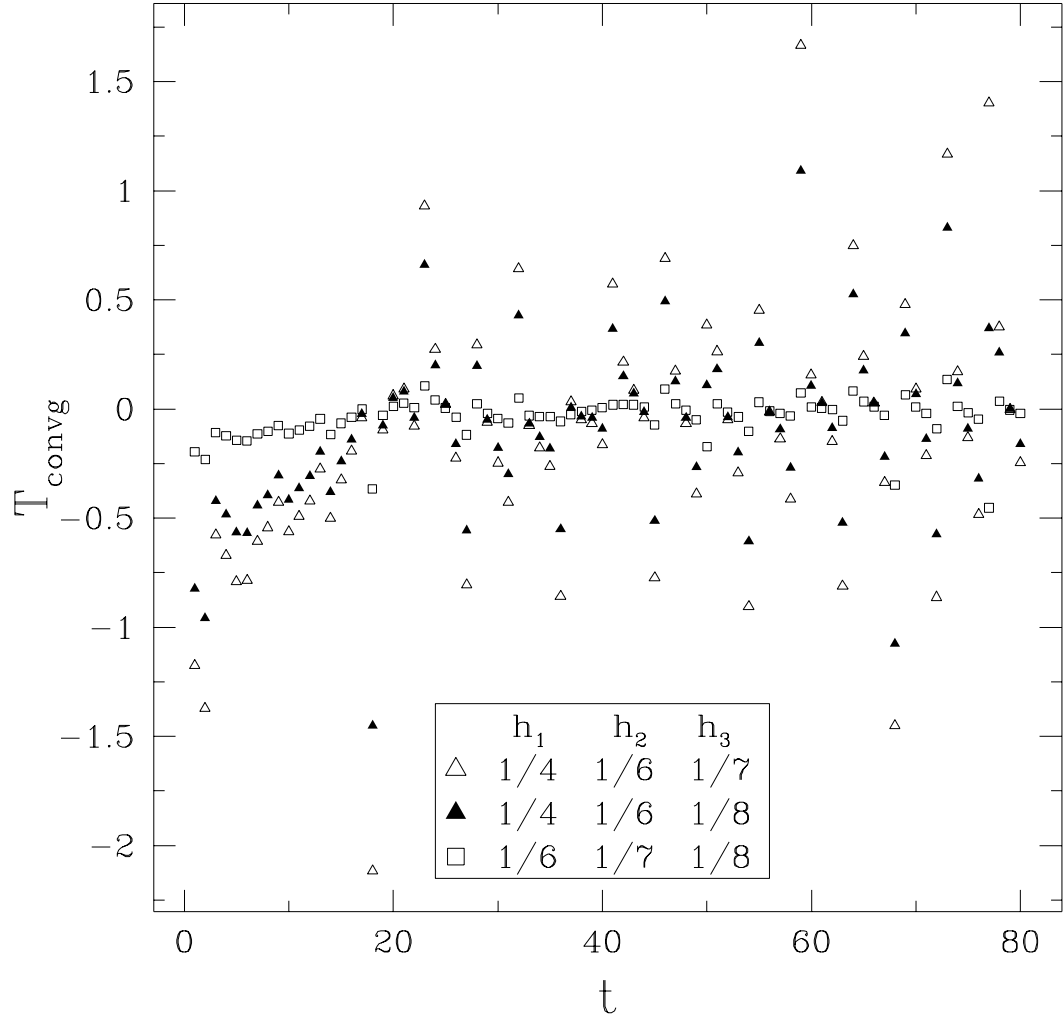
Figure 3.11: Convergence factors, T_{convg}, for the real part of the scalar field ϕ from the solution of the three dimensional difference equations.

Chapter 4

Annihilation Boundary Layers

The boundary conditions (3.30) and (3.30) are effective only when the solution of ϕ is smooth near the boundaries. When a distribution of matter comes in contact with the computational boundary, the matter is reflected off the boundary as shown in figure 4.14 This reflection causes gross computational errors at subsequent times in the simulation. Thus there is a need to find boundary conditions which minimize the amount of matter reflected at the computational boundaries.

Baskakov and Popov [1] found a method of computing the boundary condition at a finite point for the one spatial dimension Schrödinger equation:

$$i\frac{\partial \phi}{\partial t} + \frac{\partial^2 \phi}{\partial x^2} + V(x,t)\phi = 0 \tag{4.1}$$

in a region where the potential, $V(x,t)$ is nearly zero. By use of a Green's function technique, they found that at a point $x = \pm a$:

$$i\frac{\partial \phi(\pm a, t)}{\partial x} = \mp \frac{\exp^{-i\pi/4}}{\sqrt{\pi}} \frac{\partial}{\partial x} \int_0^t \phi(\pm a, \xi) \frac{d\xi}{\sqrt{t - \xi}} \tag{4.2}$$

where they assume $V(\pm a, t) = 0$. This type of boundary condition has one major drawback. Although there is a way to generalize this boundary condition to three dimension [36], one cannot assume that the potential will be zero at the

computational boundaries for the time-dependent Schrödinger problem coupled with Newtonian gravity.

Another possible finite boundary condition for the Schrödinger equation is to use the "absorbing boundary conditions" of Israeli and Orszag [23]. They suggest equating the Schrödinger equation with the wave equation in operator form:

$$\frac{\partial^2 \phi}{\partial x^2} = \left(-i\frac{\partial}{\partial t} + V \right) \phi \equiv L^2 \phi \qquad (4.3)$$

where the operator:

$$L = \sqrt{\left(-i\frac{\partial}{\partial t} + V - \omega_o \right) + \omega_o} \qquad (4.4)$$

can be approximated by:

$$L \simeq \frac{1}{2}\sqrt{\omega_o} + \frac{1}{2\sqrt{\omega_o}} \left(-i\frac{\partial}{\partial t} + V \right). \qquad (4.5)$$

This approximation of L can be used in the boundary conditions:

$$\left(\frac{\partial}{\partial x} \pm L \right) \phi = 0, \ \text{at} \ x = \pm a \qquad (4.6)$$

to allow only the outgoing parts of ϕ. One of the problems with these boundary conditions is that the solution must consist only of waves with oscillation frequency near ω_o. Another problem is that in multi-dimensions, only waves with normal incidence are absorbed effectively. The annihilation boundary conditions discussed in this chapter perform nearly as well as the transparent boundary conditions for the time dependent one dimensional Schrïnger equation and better than the absorbing boundary condions. However, the annihilation boundary conditions do not incur the problems that transparent and absorbing boundary conditions incur when used with the multi dimensional time dependent Schrödinger equation.

4.1   One Dimensional Annihilation Boundary Layer

The discussion of annihilation boundary layers begins with the one dimensional Schrödinger equation (4.1) with $V = 0$:

$$\frac{\partial \phi}{\partial t} = i \frac{\partial^2 \phi}{\partial x^2} \tag{4.7}$$

which given the Fourier analyzed initial data:

$$\phi(x, 0) = \sum_{k=-\infty}^{\infty} A_k e^{ikx} \tag{4.8}$$

has the solution:

$$\phi(x, t) = \sum_{k=-\infty}^{\infty} A_k \exp\left[-ik^2 t + ikx\right] \tag{4.9}$$

If one adds the term $-\nu\phi$ to the one dimensional Schrödinger equation:

$$\frac{\partial \phi}{\partial t} = i \frac{\partial^2 \phi}{\partial x^2} - \nu\phi, \text{for } \nu \geq 0. \tag{4.10}$$

Then given the initial data (4.8), this equation has the solution:

$$\phi(x, t) = \sum_{k=-\infty}^{\infty} A_k \exp\left[\left(-ik^2 - \nu\right) t + ikx\right] \tag{4.11}$$

So now the solution is damped exponentially in time. One might wonder what the solution is for a nonconstant ν:

$$\nu(x) = \begin{cases} 0 & \text{for } |x| \leq |x_{bd}| - (w + \Delta) \\ 0 \rightarrow H & \text{as } |x| : |x_{bd}| - (w + \Delta) \rightarrow |x_{bd}| - (w - \Delta) \\ H & \text{for } |x| \geq |x_{bd}| - (w - \Delta) \end{cases} \tag{4.12}$$

where x_{bd} is the computational boundary and w, Δ and H are all positive constants. The solution of (4.10) using (4.12) can be computed computationally using the implicit difference equation:

$$\Delta_+^t \phi_j^n = \left(i\Delta_+^x \Delta_-^x - \nu_j\right) \mu_+^t \phi_j^n \tag{4.13}$$

Reflection Coefficient

$$R\left(t_{init}, t_{fin}, x_{lly}, x_{rly}, w, \Delta, H\right) \equiv \frac{M_{tst}\left(t_{fin}, x_{lly}, x_{rly}\right) - M_{con}\left(t_{fin}, x_{lly}, x_{rly}\right)}{M_{con}\left(t_{init}, x_{lly}, x_{rly}\right) - M_{con}\left(t_{fin}, x_{lly}, x_{rly}\right)}$$

Variable Definitions

$$M\left(t, x_{lft}, x_{rht}\right) \equiv \sum_{j=Nx_{lft}}^{Nx_{rht}} \phi_j^n \phi_j^{n*} h$$

$$x_{lft} \equiv x_o + Nx_{lft}h$$

$$x_{rht} \equiv x_o + Nx_{rht}h$$

$$x_{lly} \equiv x_o + Nx_{lft}h + w + \Delta$$

$$x_{rly} \equiv x_o + Nx_{rht}h - w - \Delta$$

$$t \equiv n\lambda h$$

Table 4.1: Definition of the reflection coefficient

with the extrapolation boundary conditions:

$$\phi_{j\pm1}^n = \chi_{\pm}^x \phi \tag{4.14}$$

where the operators: $\Delta_+^t, \Delta_{\pm}^x, \mu_+^t$ and $\chi_{\pm}^x$ are defined in table 3.2.

The movies 4.1-4.4 show numerically what happens to $\phi\phi^*$ when this form of ν is used in (4.10). The movies depict three solutions all starting with the same initial data with the first frame of each movie starting at $t_{init} = 0$ and advancing in increments of 16 to $t_{final} = 240$ with each frame having an x domain from 0 to 256 and a $\phi\phi^*$ range from 0 to 1. The dark lined solution has been computed on a computational domain from -512 to 512 with 1025 points on the computational grid while the lighter line solutions have been computed on a computational domain from -128 to 128 using 257 grid points. Thus the computational solutions should appear identical until the pulse comes in contact with the smaller computational boundary at $x = 128$.

The dotted vertical lines in the figures give the location of the boundary of the *test* computational domain, and the dashed vertical lines indicate where the annihilation boundary layers begin. Movie 4.1 shows just the $\phi\phi^*$ pulse of the dark lined solution moving across the frame. The next movie 4.2 shows the dark line solution and a light line solution with $\nu(x) = 0$. The different behavior of the solutions becomes apparent when the pulse comes in contact with the computational boundary of the light line solution at $x = 128$. With $\nu(x) = 0$, the light line pulse reflects off the boundary due to the extrapolation boundary condition and essentially becomes a mirror reflection of the dark line solution. In movie 4.3, a ν defined by (4.12) with $w = 16$, $\Delta = 8$ and $H = 0.3$ is used. Thus ν becomes nonzero at $x = 112$ and ramps up to 0.3 at $x = 128$. The movie shows what effect this has on the light line pulse as the pulse moves into the region with nonzero ν. As one can see, the pulse is quickly damped out with no visible reflection. The obvious question now to ask is what effect does this have on the numerical solution of (4.10) in the region where $\nu(x) = 0$. Movie 4.4 shows the dark line solution of movie 4.1 and the light line solution of movie 4.3. As one can see the solutions only appear to differ in the region where $\nu \neq 0$. Thus this region acts as an annihilation layer which quickly forces the solution to zero within the layer while apparently having little effect on the solution interior to the annihilation layer.
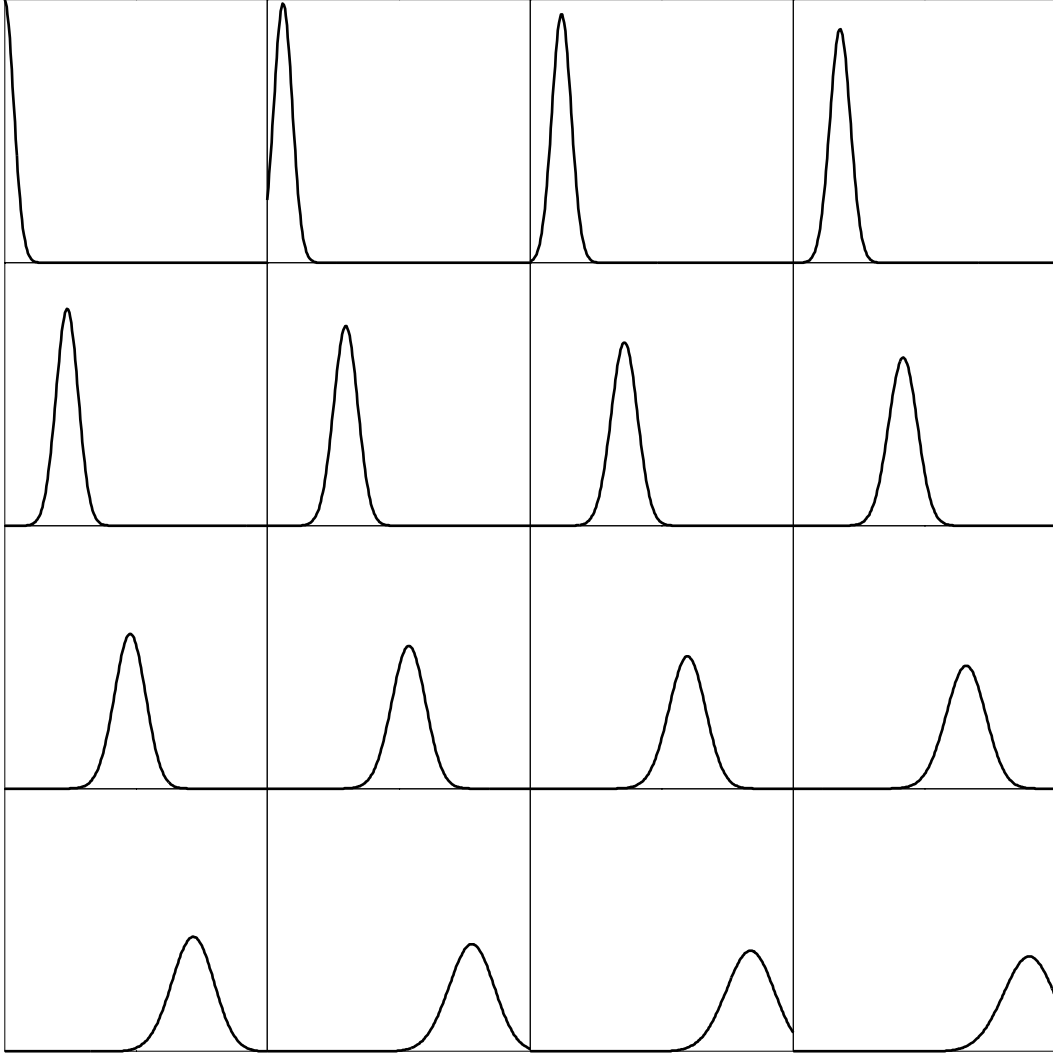
Figure 4.1: Time evolution of the matter distribution, $\phi\phi^*$, for the one dimensional Schrödinger equation on the larger computational domain. Limits: computational domain (x: -512 to 512); frame domain (x: 0 to 256); frame range (ρ: 0 to 1).

Figure 4.2: Time evolution of the matter distribution, $\phi\phi^*$, for two solutions of the one dimensional Schrödinger equation, one on the larger computational domain and the other on the smaller computational domain without an annihilation layer. Limits: computational domain-thin line (x: -128 to 128) -thick line (x: -512 to 512); frame domain (x: 0 to 256); frame range (ρ: 0 to 1).
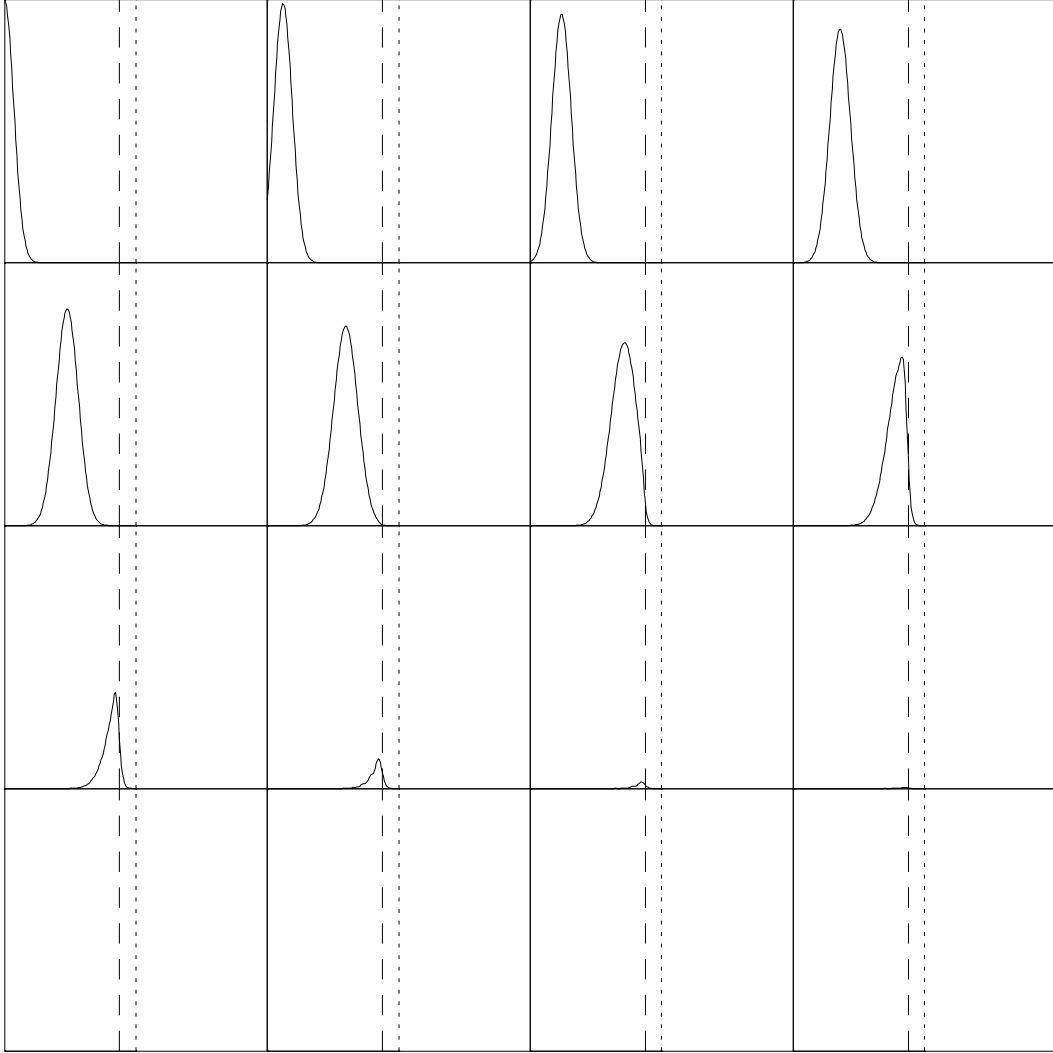
Figure 4.3: Time evolution of the matter distribution, $\phi\phi^*$, for the one dimensional Schrödinger equation on the smaller computational domain with an annihilation layer. Limits: computational domain (x: -128 to 128); frame domain (x: 0 to 256); frame range (ρ: 0 to 1); boundary layer begins at x=112

58

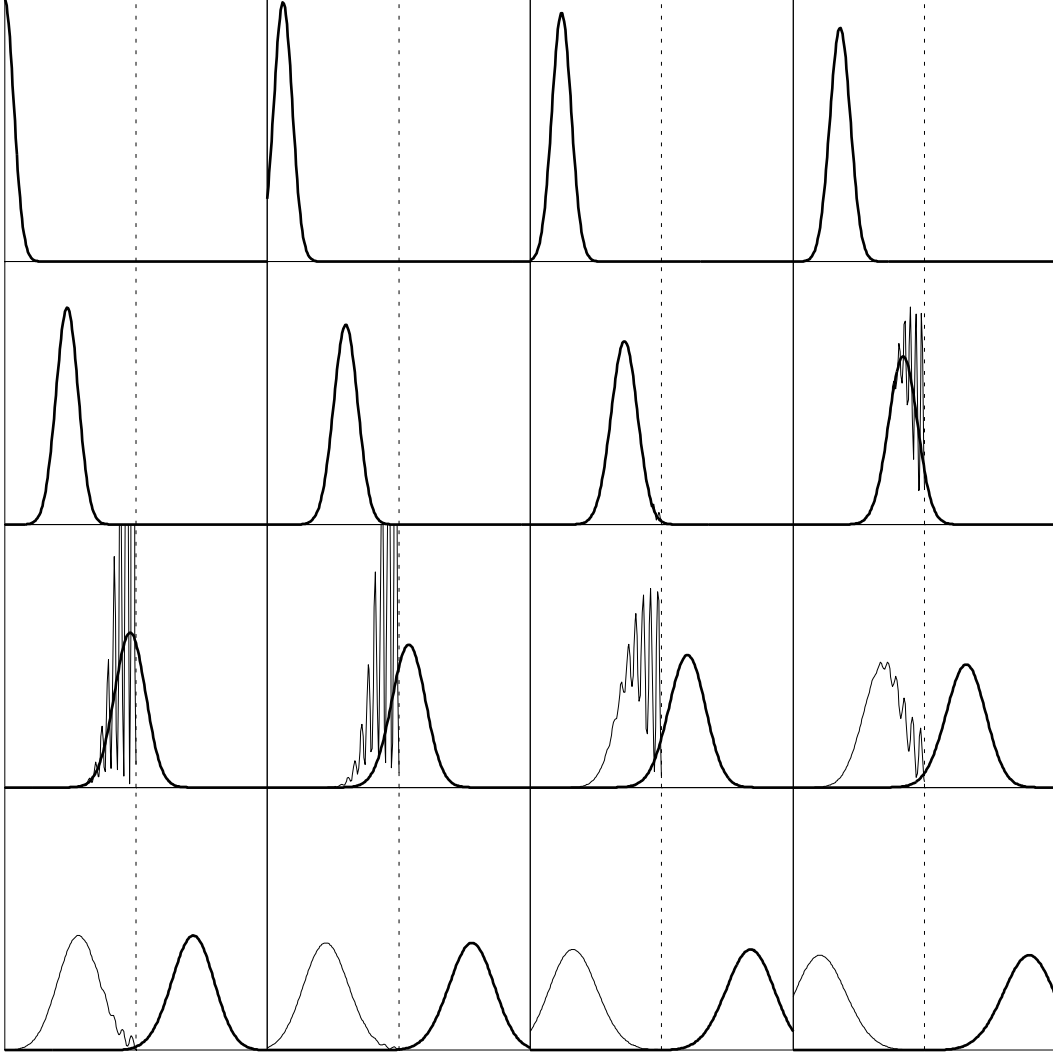Figure 4.4: Time evolution of the matter distribution, $\phi\phi^*$, for two solutions of the one dimensional Schrödinger equation, one on the larger computational domain and the other on the smaller computational domain with an annihilation layer. Limits: computational domain-thin line (x: -128 to 128) -thick line (x: -512 to 512); frame domain (x: 0 to 256); frame range (ρ: 0 to 1); boundary layer begins at x=112
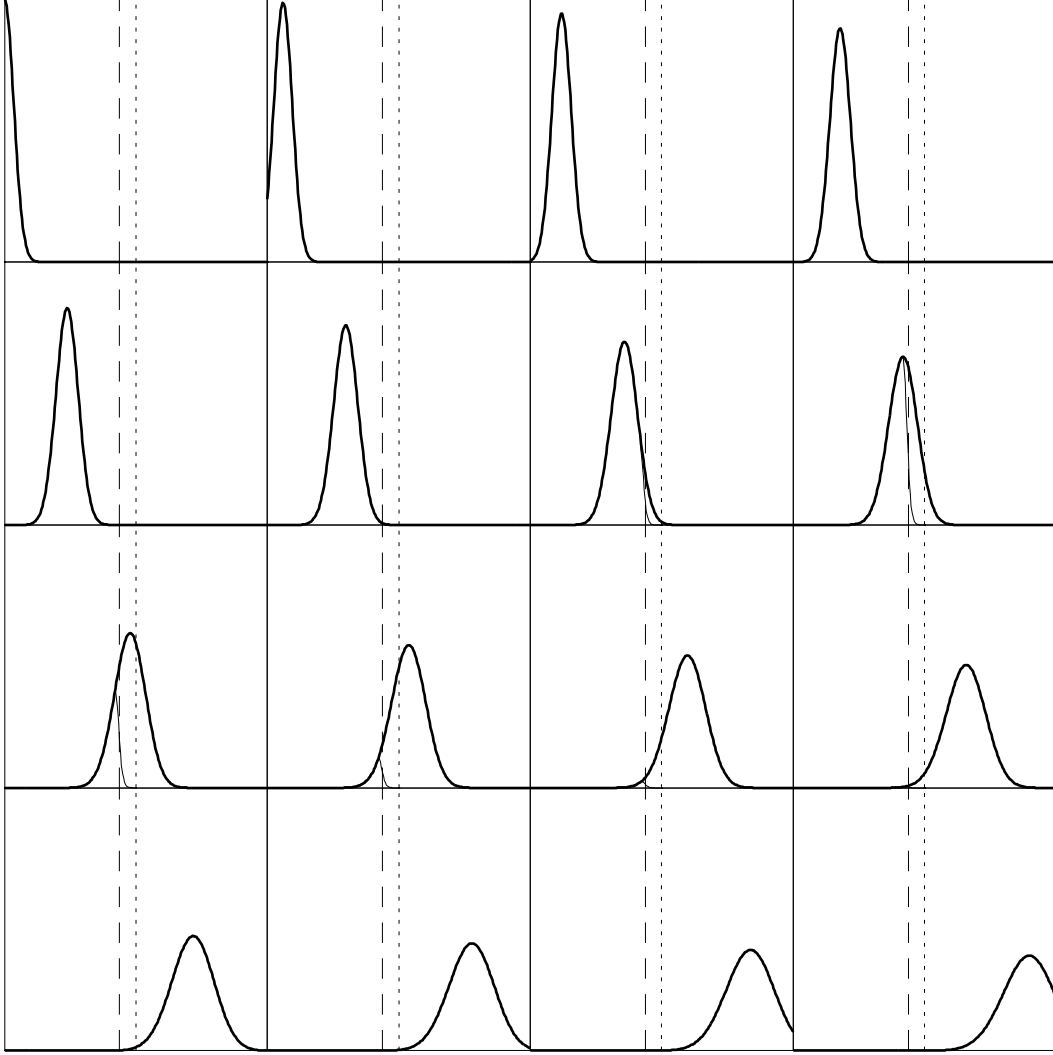
A quantitative analysis of the performance of the annihilation boundary layers can be made by calculating the amount of reflection of the initial pulse. Since the spatial integral of $\phi\phi^*$ is conserved over time, this integral quantity will be used to calculate the amount of reflection due in part to the extrapolation boundary condition for various cases of $\nu(x)$. The reflection coefficient for this calculation is defined in table 4.1. The quantity $M(t, x_{left}, x_{right})$ is just the amount of mass contained with the left and right x boundaries, x_{left} and x_{right}, at time t. The subscripts on M in the definition of R refer to the two types of solutions shown in the previous movies. The *test* subscript refers to the solutions with a computational range from $x = -128$ to $x = 128$ for which ν is varied to test the behavior of the annihilation layers. The *control* subscript refers to the solution with a computational range from $x = -512$ to $x = 512$ to which the *test* solutions are compared. Thus R measures the amount of mass that remains in interior region where $\nu(x) = 0$ due to the pulse's interaction with the boundary as a fraction of the amount of mass that leaves the region in the control computation.

Figures 4.5-4.7 give a comparison of the reflection coefficient versus H for various values of w and Δ for the problem discussed above. Figure 4.5 compares various values of Δ for $w = 4$. As Δ increases from $0 \rightarrow 4$, the amount of reflection for each value of H decreases dramatically. This is due to the decrease in the gradient of the ramp up of ν from $0 \rightarrow H$ with increasing Δ. All three figures show that the reflection coefficient decreases when increasing w which is due to the increased damping of pulses entering the annihilation layer before they hit the boundary and are reflected. The last figure shows that one can make annihilation layers that allow less than 0.1% reflection but these
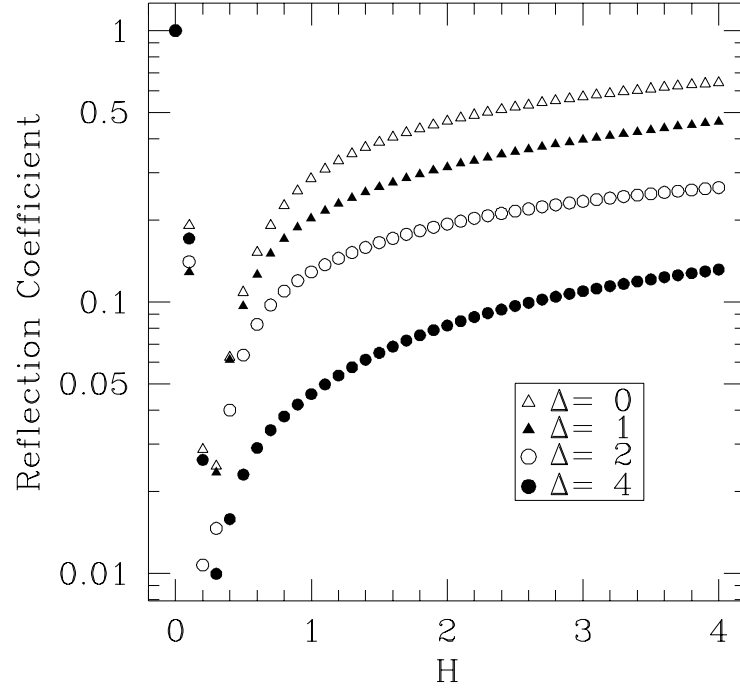
Figure 4.5: One Dimensional Schrödinger Equation: Reflection Coefficient versus H for $w = 4$.

layers take up almost 40% of the computational domain. In one dimension this is not a severe restriction as the domain size can usually be increased without worrying about computational memory.
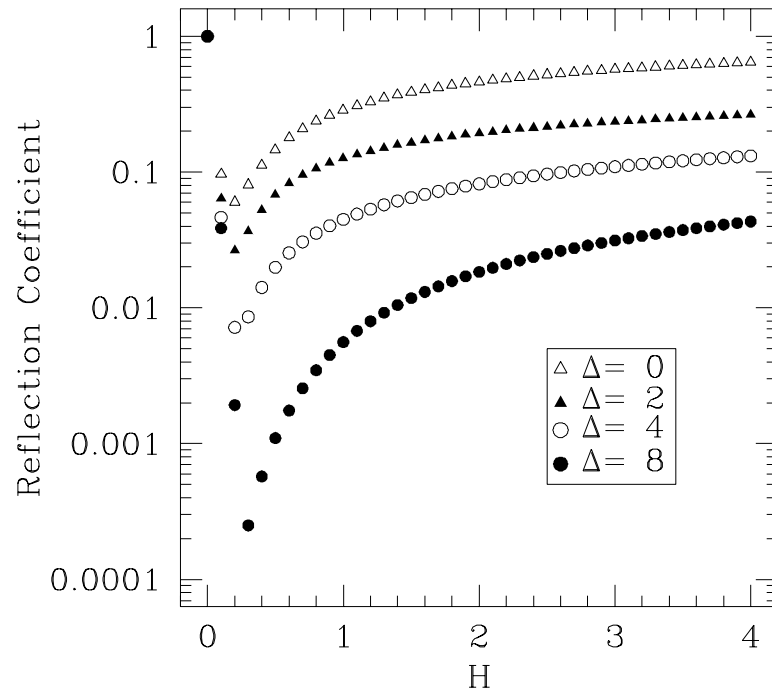
Figure 4.6: One Dimensional Schrödinger Equation: Reflection Coefficient versus H for $w = 8$.
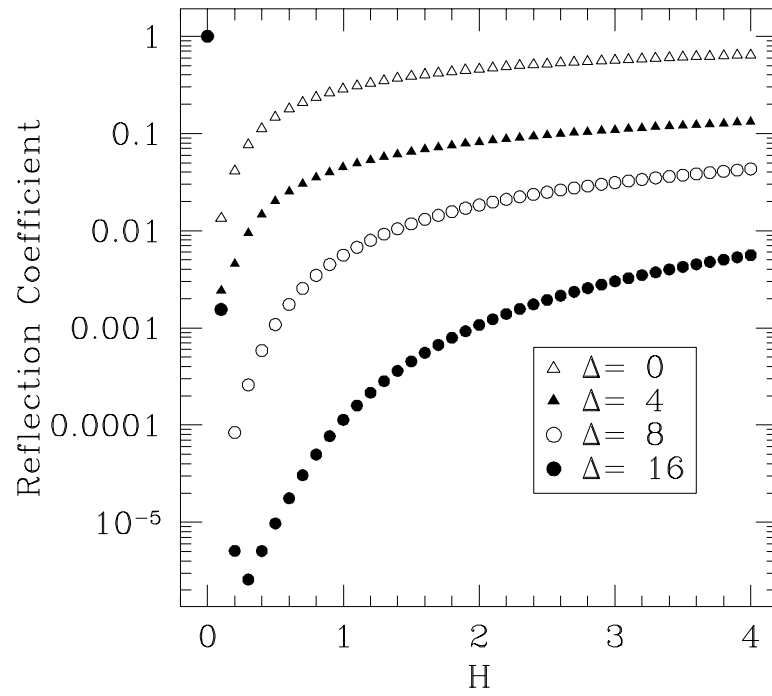
Figure 4.7: One Dimensional Schrödinger Equation: Reflection Coefficient versus H for $w = 16$.

4.2 Annihilation Boundary Layers for the Spherically Symmetric Problem

The annihilation boundary layer has been shown to work quite well with the one dimensional Schrödinger equation with no potential term, but for this study, they must also work well with the three dimensional time dependent Schrödinger equation coupled with Newtonian gravity. As an initial test of these layers, I incorporate the annihilation layers into the spherically symmetric equations:

$$\frac{\partial \phi}{\partial t} = \frac{3i}{2} \frac{\partial}{\partial r^3} \left(r^2 \frac{\partial \phi}{\partial r} \right) - iV\phi - \nu\phi \qquad (4.15)$$

$$3 \frac{\partial}{\partial r^3} \left(r^2 \frac{\partial V}{\partial r} \right) = \phi\phi^* \qquad (4.16)$$

where the $-\nu\phi$ term has been added to cause exponential damping in regions where $\nu \neq 0$ and the partial derivatives with respect to r^3 are used so that the regularity condition at $r = 0$ automatically satisfied by the difference equations:

$$\Delta_+^t \phi_j^n = i \left[\frac{1}{2} \left(\alpha_+^r \Delta_+^r - \alpha_-^r \Delta_-^r \right) - \chi_+^t V_j^n - \nu_j \right] \mu_+^t \phi_j^n \qquad (4.17)$$

$$\left(\alpha_+^r \Delta_+^r - \alpha_-^r \Delta_-^r \right) V_j^n = \phi_j^n \phi_j^{n*} \qquad (4.18)$$

Again, the difference operators used above are defined in table 3.2. The conditions at the computational boundary, r_J, are:

$$\phi_{J+1}^n = \xi_+^r \phi_J^n \qquad (4.19)$$

$$V_{J+1}^n = V_{J-1}^n - \frac{h}{r_J} V_J^n. \qquad (4.20)$$

and ν_j is:

$$\nu(r_j) = \begin{cases} 0 & \text{for } r_j \leq r_{bd} - (w + \Delta) \\ 0 \rightarrow H & \text{as } r_j : r_{bd} - (w + \Delta) \rightarrow r_{bd} - (w - \Delta) \\ H & \text{for } r_j \geq r_{bd} - (w - \Delta) \end{cases} \qquad (4.21)$$

These difference equations were used to evolve a given set of initial data; results are shown in figures 4.8-4.9. These movies depict the radial density of matter, $r^2\phi\phi^*$, within a given shell at radius r. Again, the dotted vertical lines in the movie frames give the location of the boundary of the *test* computational domain, and the dashed vertical lines indicate where the annihilation boundary layers begin. Each movie starts with the same initial data at $t_{init} = 0$ and advances in increments of $\delta t = 1$ to $t_{final} = 15$. Each frame has a domain from 0 to 32 and an $r^2\phi\phi^*$ range from 0 to 2. The dark lined solution has been computed on a computational domain from 0 to 128 with $h = 1/32$ while the lighter line solutions have been computed on a computational domain from 0 to 32 using the same value of h. Thus the computational solutions should be identical until the matter distribution comes in contact with the smaller computational boundary at $r = 32$. Movie 4.8 shows only the matter distribution for the control solution which first implodes quite violently and subsequently moves out across the frame. The next movie 4.9 shows a light line solution computed with $\nu(r) = 0$. The different behavior of the solutions becomes apparent when the pulse comes in contact with the computational boundary of the solution at $r = 32$. The pulse clearly reflects off the boundary due to the extrapolation boundary condition. Movie 4.10 shows the control solution (dark line) with computational boundary at $r = 128$ and a test solution (light line) with a ν defined by (4.12) and $w = 4$, $\Delta = 2$ and $H = 3.0$. Thus clearly for the test calculation ν becomes nonzero at $r = 26$ and ramps up to 3.0 at $x = 32$. The movie shows the effect of the boundary layer. As one can see, the distribution is damped with only a small amount of reflection off the boundary. Also one can see that the dark and light line solutions differ

by only relatively small features in the interior region. Thus the annihilation boundary layer works quite well for the spherically symmetric time-dependent Schrödinger equation coupled with Newtonian gravity.
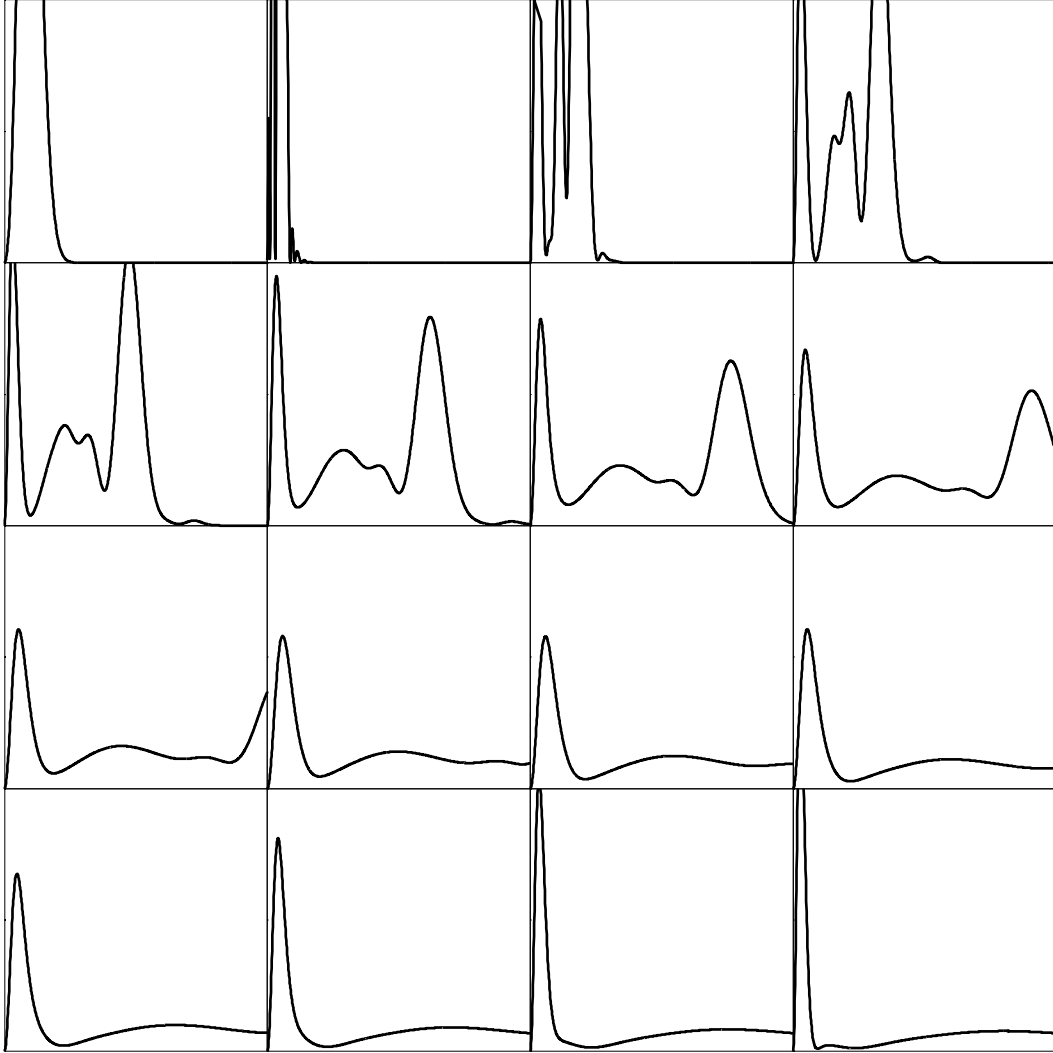
Figure 4.8: Time evolution of the matter distribution, $r^2\phi\phi^*$ for the spherically symmetric Schrödinger equation on the larger computational domain. Limits: computational domain (r: 0 to 128); frame domain (r: 0 to 32); frame range ($r^2\phi\phi^*$: 0 to 2)
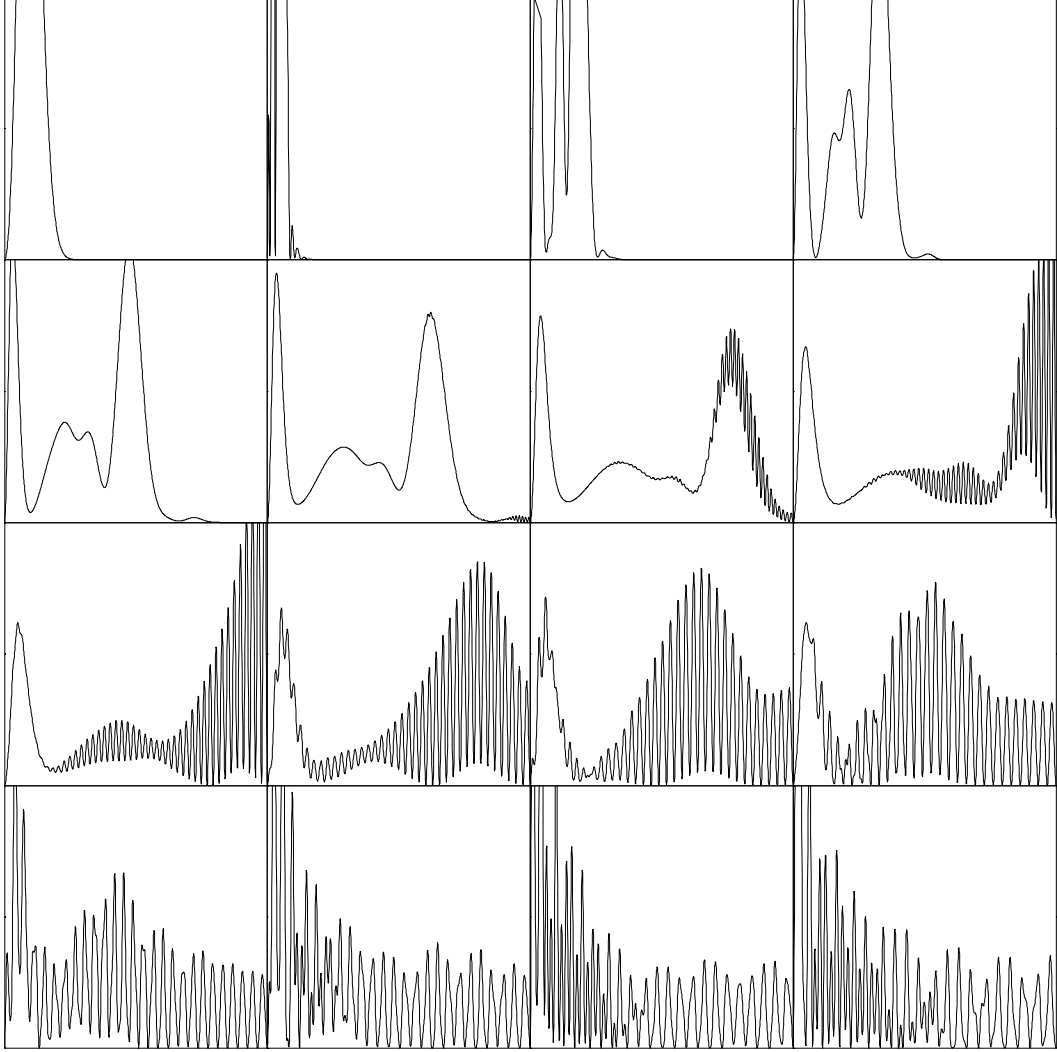
Figure 4.9: Time evolution of the matter distribution, $r^2\phi\phi^*$, for the spherically symmetric Schrödinger equation on the smaller computational domain without an annihilation layer. Limits: computational domain (r: 0 to 32); frame domain (r: 0 to 32); frame range ($r^2\phi\phi^*$: 0 to 2)
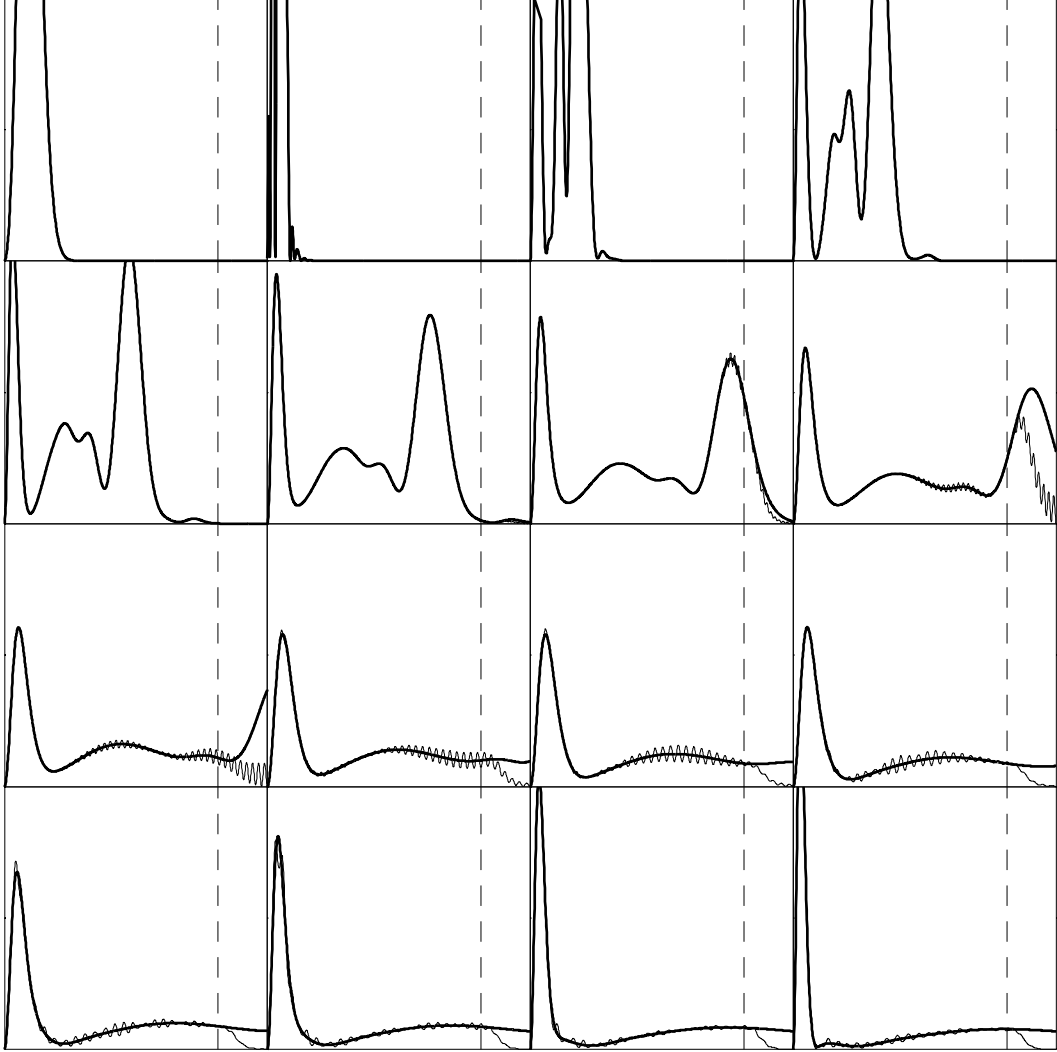
Figure 4.10: Time evolution of the matter distribution, $r^2\phi\phi^*$ for the spherically symmetric Schrödinger equation on the smaller computational domain with an annihilation layer. Limits: computational domain-thin line (r: 0 to 32); thick line (r: 0 to 128);frame domain (r: 0 to 32); frame range ($r^2\phi\phi^*$: $0 to 2$); boundary layer begins at $x=26$

A quantitative analysis of these boundary layers for this problem are given in figures 4.11-4.13. Again, I use the reflection coefficient defined in table 4.1 where the amount of matter contained within a sphere of radius r_{outer} is calculated from the numerical integral:

$$M(t, r_{outer} = Jh) \equiv 4\pi \sum_{j=1}^{J} \phi_j^n \phi_j^{n*} r_j^2 h. \qquad (4.22)$$

Figures 4.11-4.13 are plots which indicate the dependence of the reflection coefficient on H, w and Δ for the problem discussed above. In terms of the reflection coefficient versus Δ for a given value of w and H, the results are similar to those of the previous section. Decreases in the reflection of matter are seen as Δ increases. Also there is a dramatic decrease in the reflection coefficient as w is increased. As seen in figure 4.13, one can easily obtain reflections less than 1% for an annihilation layer that takes up less than 20% of the computational domain.
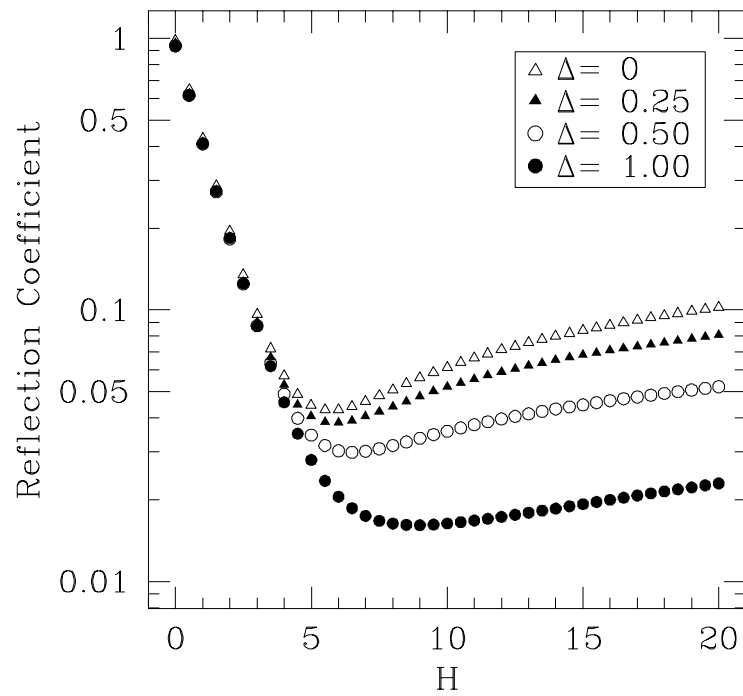
Figure 4.11: Spherically Symmetric Schrödinger Equation: Reflection Coefficient versus H for $w = 1$.
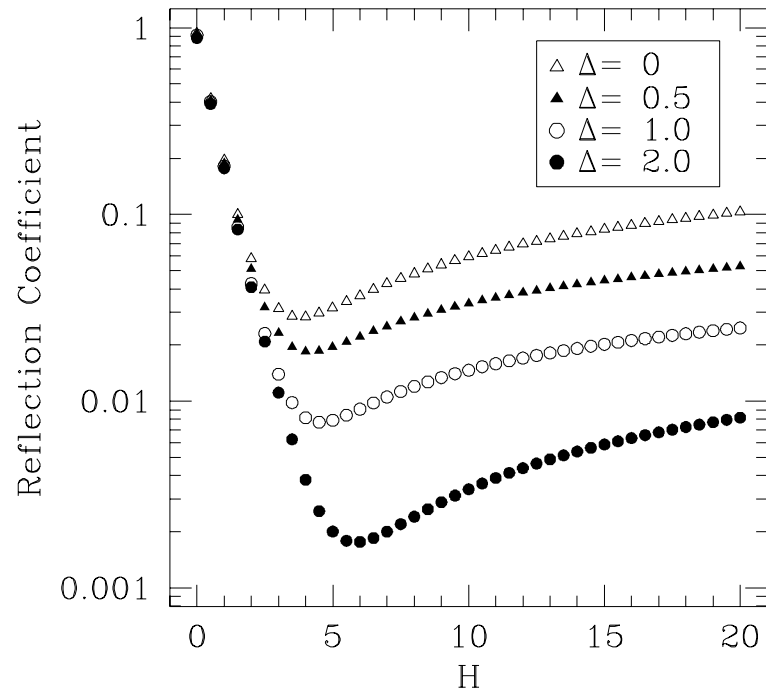
Figure 4.12: Spherically Symmetric Schrödinger Equation: Reflection Coefficient versus H for $w = 2$.
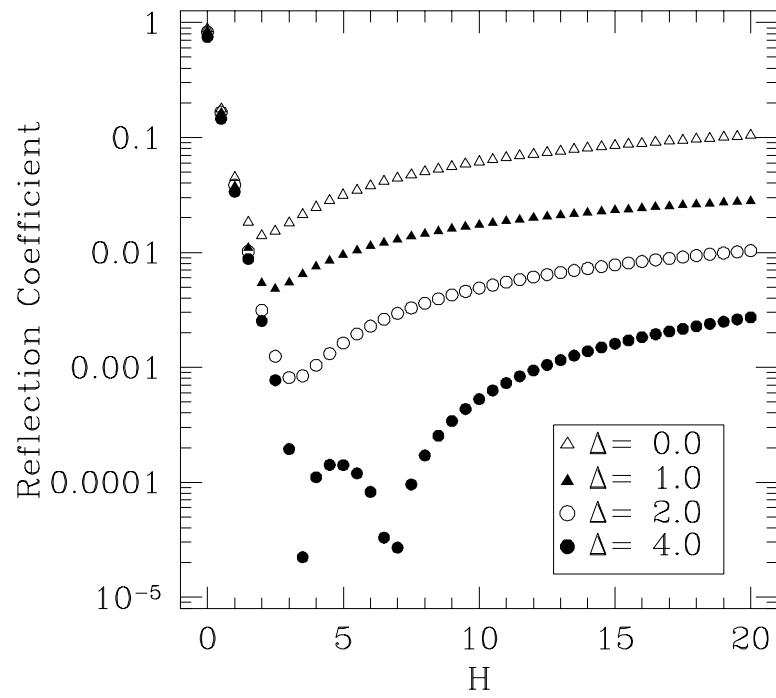
Figure 4.13: Spherically Symmetric Schrödinger Equation: Reflection Coefficient versus H for $w = 4$.

4.3 Annihilation Boundary Layers for the Three Dimensional Problem

This section is a discussion of the application of annihilation boundary layers to the three dimensional time-dependent Schrödinger equation coupled with Newtonian gravity. Given the pattern of the previous two examples, the Schrödinger equation with an annihilation layer is:

$$\frac{\partial \phi}{\partial t} = \frac{i}{2} \nabla^2 \phi - (iV + \nu) \phi. \tag{4.23}$$

In finite difference ADI form, the only change to equations (3.24)- (3.27) is to equation (3.27) which becomes:

$$\left(1 + \frac{\lambda h}{2} \left(i \chi_+^t V_{ijk}^n + \nu_{ijk}\right)\right) \phi_{ijk}^{n+1} = \left(1 + \frac{\lambda h}{2} \left(i \chi_+^t V_{ijk}^n + \nu_{ijk}\right)\right). \tag{4.24}$$

Here ν_{ijk} is:

$$\nu(x_i, y_j, z_k) = \begin{cases} 0 & \begin{array}{l} \text{for } |x_i| \leq |x_{bd}| - (w + \Delta) \text{ or} \\ \text{for } |y_j| \leq |y_{bd}| - (w + \Delta) \text{ or} \\ \text{for } |z_k| \leq |z_{bd}| - (w + \Delta), \end{array} \\ 0 \rightarrow H & \begin{array}{l} \text{as } |x_i| : |x_{bd}| - (w + \Delta) \rightarrow |x_{bd}| - (w - \Delta) \text{ or} \\ \text{as } |y_j| : |y_{bd}| - (w + \Delta) \rightarrow |y_{bd}| - (w - \Delta) \text{ or} \\ \text{as } |z_j| : |z_{bd}| - (w + \Delta) \rightarrow |z_{bd}| - (w - \Delta), \end{array} \\ H & \begin{array}{l} \text{for } |x_i| \geq |x_{bd}| - (w - \Delta) \text{ or} \\ \text{for } |y_j| \geq |y_{bd}| - (w - \Delta) \text{ or} \\ \text{for } |z_k| \geq |z_{bd}| - (w - \Delta). \end{array} \end{cases}$$

$$\tag{4.25}$$

Figures 4.14-4.16 display nine cases of the numerical solution of the time dependent Schrödinger equation coupled with Newtonian gravity using an annihilation boundary layer. The dotted vertical lines in the movie frames give the location of the boundary of the *test* computational domain, and the dashed vertical lines indicate where the annihilation boundary layers begin. The first movie uses the initial data for a single boson star which is given momentum

in the x direction and shows three solutions generated on two computational domains. One domain has physical dimensions -32 to 0 in the x, y and z directions and uses $65 \times 65 \times 65$ grid points [1] while the other domain has dimensions of -32 to 32 along the x direction and -32 to 0 along the y and z directions and contains $129 \times 65 \times 65$ grid points. Thus any data displayed from these two computational domains should appear similar until the star begins to interact with the smaller computational boundary at $x = 0$. The data displayed in this movie is the mass distribution along the x direction:

$$\frac{dM_i^n}{dx} \equiv \sum_{j=1}^{ny} \sum_{k=1}^{nz} \phi_{ijk}^n \phi_{ijk}^{n*} h^2. \tag{4.26}$$

Each frame has an x domain from -32 to 16 and a mass distribution range from 0 to 12. The first frame is at $t_{init} = 0$. $\Delta t = 1$ so that the final frame is at $t_{final} = 15$. The lighter two solutions are for $\nu_{ijk} = 0$ with one generated on the smaller computational domain and the other on the larger domain. Thus as the pulse approaches the smaller computational physical boundary at $x = 0$, the solution computed on the smaller domain is reflected while the larger domain solution continues onward. The darkest solution was generated on the smaller computational domain with a nonzero ν with $w = 2$, $\Delta = 2$ and $H = 0.3$, As the pulse for its solution enters the annihilation layer, the pulse is damped and very little is reflected.

Figure 4.15 shows results from a computation for a single boson star given the same amount of momentum in the positive x and y directions. Again, the figure shows three solutions generated on two computational domains. One

---

[1]Computational grids are defined in the form $nx \times ny \times nz$ where nx, ny and nz are the number of grid points along the x, y and z directions respectively.

domain has physical dimensions -32 to 0 in the x, y and z directions and uses $65 \times 65 \times 65$ grid points while the other domain has dimensions of -32 to 32 along the x and y directions and -32 to 0 along the z direction and contains $129 \times 129 \times 65$ grid points. Thus any data displayed from these two computational domains should appear similar until the star begins to interact with the smaller computational boundary at $x = 0$ and $y = 0$ along the z-axis. The data displayed in this movie is the mass distribution along the y direction:

$$\frac{dM_j^n}{dy} \equiv \sum_{i=1}^{nx} \sum_{k=1}^{nz} \phi_{ijk}^n \phi_{ijk}^{n*} h^2. \tag{4.27}$$

Each frame has an y domain from -32 to 16 and a mass distribution range from 0 to 12 with the first frame starting at $t_{init} = 0$ and with each successive frame advancing in time increments of 1.5 until the final frame at $t_{final} = 22.5$. The lighter two solutions are for $\nu_{ijk} = 0$ with one generated on the smaller computational domain and the other on the larger domain. Thus as the pulse approaches the smaller computational physical boundary at $y = 0$, the solution computed on the smaller domain is reflected while the larger domain solution continues onward. The darkest solution was generated on the smaller computational domain with a nonzero ν with $w = 2$, $\Delta = 2$ and $H = 0.3$, As the pulse for its solution enters the annihilation layer, the pulse is damped and even less of the original pulse is reflected when compared to the damped pulse in the previous movie, 4.14. This is due to the larger volume of the annihilation layer near an edge of the computational box than there is near the center of a side of the computational box.

The third movie, figure 4.16, uses initial data of a single boson star given the same amount of momentum in the positive x, y and z directions and shows

three solutions generated on two computational domains. One domain has physical dimensions -32 to 0 in the x, y and z directions[2] and uses $65 \times 65 \times 65$ grid points while the other domain has dimensions of -32 to 32 along the x y and z directions and contains $129 \times 129 \times 129$ grid points. Thus any data displayed from these two computational domains should appear similar until the star begins to interact with the boundary of the smaller computational domain near $(x, y, z) = (0, 0, 0)$. The data displayed in this movie is the mass distribution along the z direction:

$$\frac{dM_k^n}{dz} \equiv \sum_{i=1}^{nx} \sum_{j=1}^{ny} \phi_{ijk}^n \phi_{ijk}^{n*} h^2. \tag{4.28}$$

Each frame has an z domain from -32 to 16 and a mass distribution range from 0 to 12 with the first frame starting at $t_{init} = 0$ and with each successive frame advancing in time increments of 2 until the final frame at $t_{final} = 30$. The lighter two solutions are for $\nu_{ijk} = 0$ with one generated on the smaller computational domain and the other on the larger domain. Thus as the pulse approaches the smaller computational physical boundary at $z = 0$, the solution computed on the smaller domain is reflected while the larger domain solution continues onward. The darkest solution was generated on the smaller computational domain with a nonzero ν with $w = 2$, $\Delta = 2$ and $H = 0.3$, As the darkest pulse enters the annihilation layer, the pulse is damped. Even less of the original dark pulse is reflected when compared to the damped pulse in the previous movie, 4.15. This is due too the larger amount of volume containing the annihilation layer near a corner of the computational box than there is near along an *edge* of the computational box.

---

[2] i.e. toward a corner of the computational domain

77

Figure 4.14: Three solutions of dM/dx showing the matter distribution colliding with and going through a *side* of the smaller computational box. Limits: computational domain: reflection and absorption solutions (x, y, z: -32 to 0), *test* solution on larger computational domain (x: -32 to 32; y, z: -32 to 0); frame domain: (x: -32 to 16); frame range (dM/dx: 0 to 12); boundary layer starts at $x = -4$

Figure 4.15: Three solutions of dM/dy showing the matter distribution colliding with and going through an *edge* of the smaller computational box. Limits: computational domain: reflection and absorption solutions: $(x, y, z$: -32 to 0), *test* solution on larger computational domain $(x, y$: -32 to 32; z: -32 to 0); frame domain: $(y$: -32 to 16); frame range $(dM/dy$: 0 to 12); boundary layer starts at $y = -4$

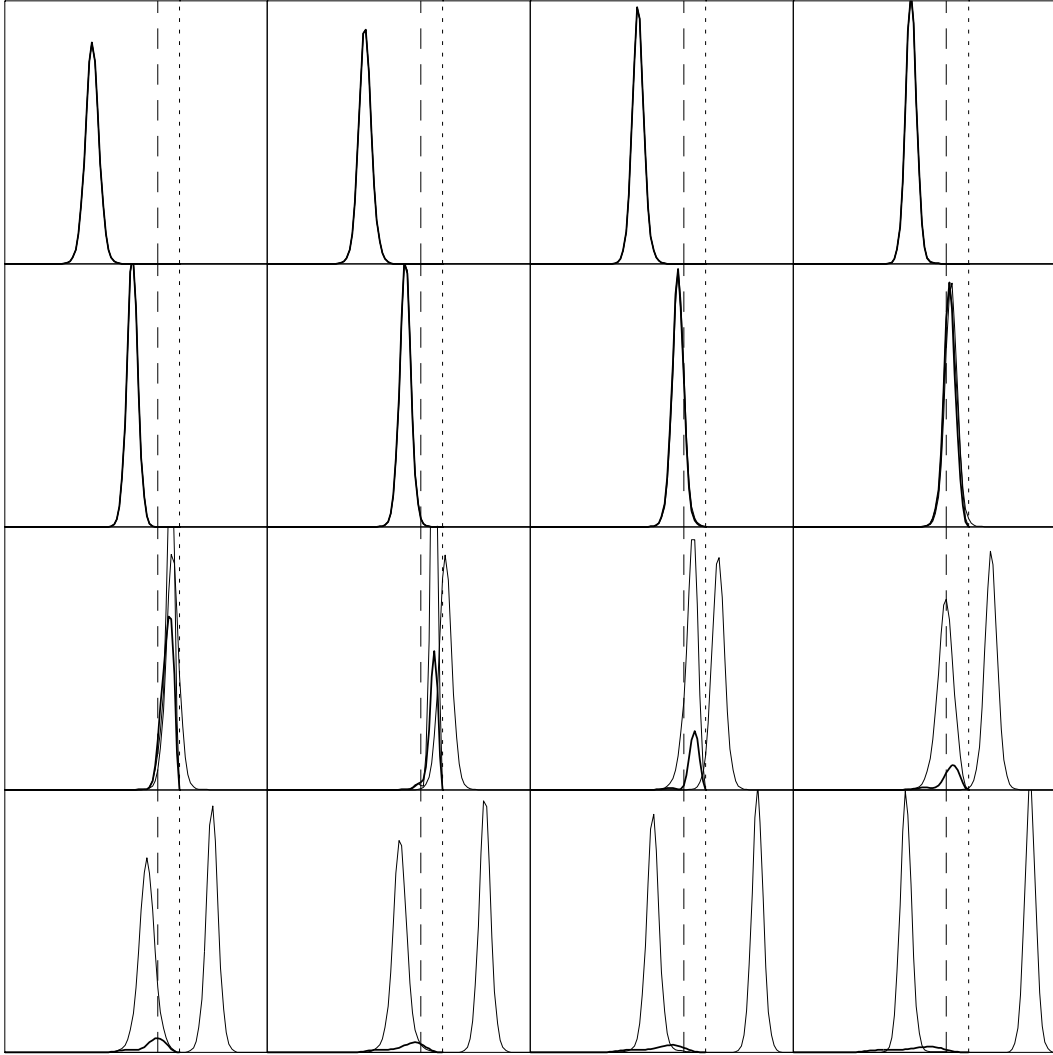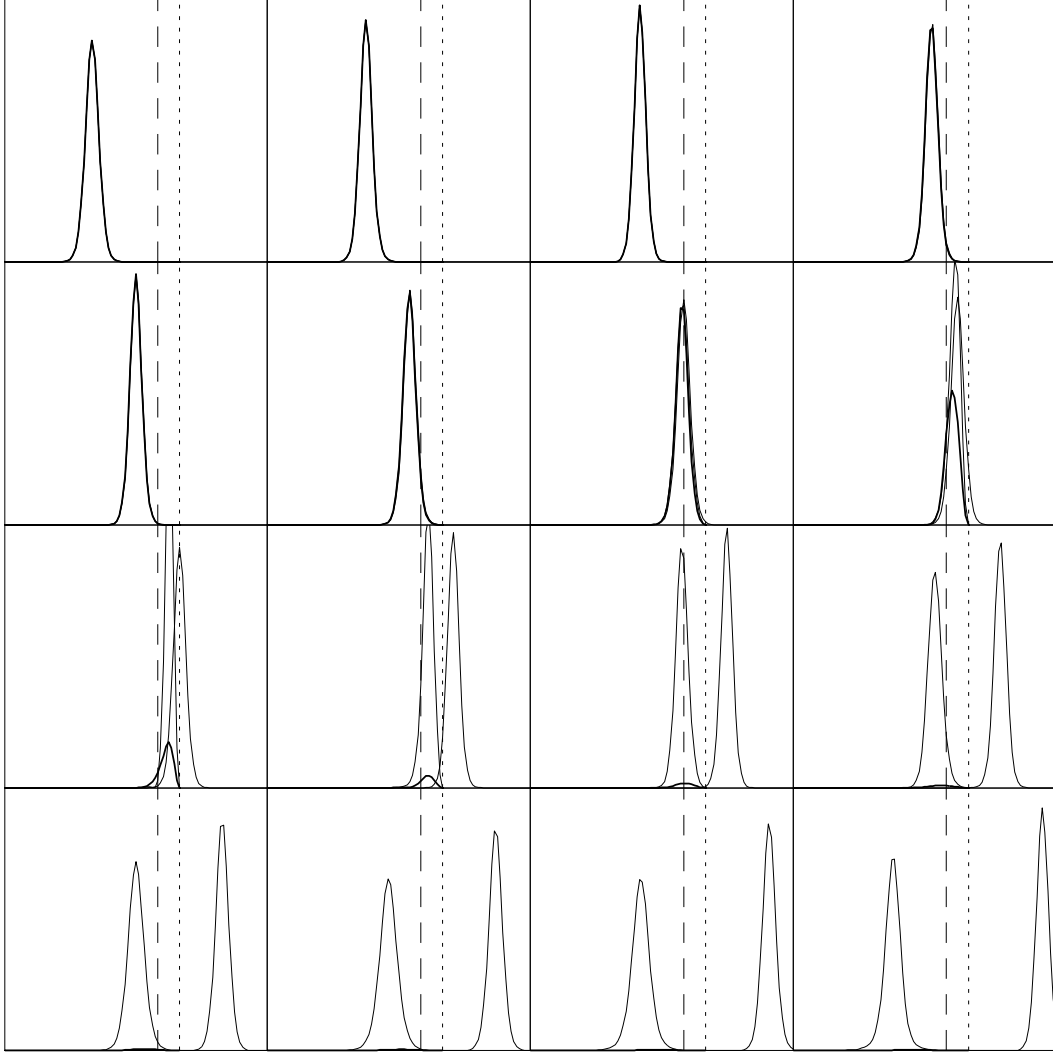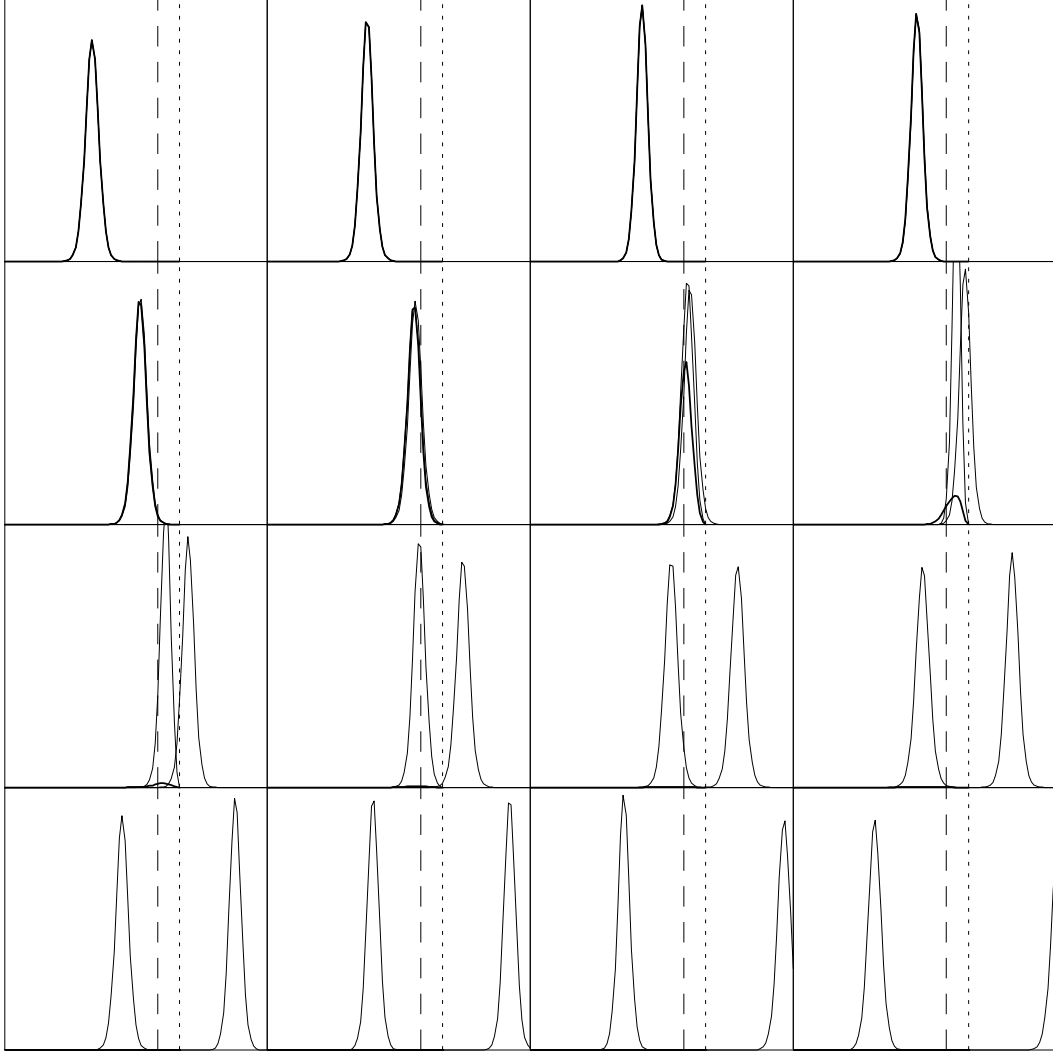Figure 4.16: Three solutions of dM/dz showing the matter distribution colliding with and going through a *corner* of the smaller computational box. Limits: computational domain: reflection and absorption solutions: $(x, y, z$: -32 to 0), *test* solution on larger computational domain $(x, y, z$: -32 to 32); frame domain: $(z$: -32 to 16); frame range $(dM/dz$: 0 to 12); boundary layer starts at $z = -4$

Figures 4.17-4.25 give a quantitative analysis of the qualitative results displayed above. The reflection coefficient is computed using the same definition given in table 3.2 but now the mass is defined to be:

$$M\left(t, \mathbf{x}_{lft}, \mathbf{x}_{rht}\right) \equiv \sum_{i=Nx_{lft}}^{Nx_{rht}} \sum_{j=Ny_{lft}}^{Ny_{rht}} \sum_{k=Nz_{lft}}^{Nz_{rht}} \phi_{ijk}^{n} \phi_{ijk}^{n*} h^3 \qquad (4.29)$$

Figures 4.17-4.19 show the amount of reflection from the matter distribution hitting the *side* of the computational domain for various values of w and Δ. As in previous sets of reflection graphs, the amount of reflection drops rapidly with increases in w and Δ for a given value of H. Figures 4.20-4.22 show the amount of reflection from the matter distribution hitting the *edge* of the computational domain. The amount of reflection is even less than that of the previous set of graphs due to the increased volume of the annihilation layer which the matter distribution encounters. Figures 4.20-4.22 show the amount of reflection from the matter distribution hitting the *corner* of the computational domain. As expected, the amount of reflection is even less than the previous two cases of the matter distribution colliding with the side and the edge of the computational domain.

Thus the annihilation boundary layer is quite effective in preventing refections off computational boundaries for the multidimensional Schrödinger equation. The major problem with these boundary layers is that the layers can easily consume a large amount of the computational volume. In the example movie shown above, the layer had a width of 4 along all sides of the computational box and thus the computational volume where the original Schrödinger equation is being solved is reduced from $32^3 = 32768$ to $24^3 = 13824$. Thus the annihilation layer takes up almost 68% of the computational volume. A solution would be to enlarge the physical size of the computational volume while

Figure 4.17: Three Dimensional Schrödinger Equation: Reflection Coefficient versus H for $w = 2$ and matter distribution hitting *side* of computational box.

keeping the number of grid points constant, but then one loses resolution. Thus with the computer resources used to perform the calculations in Chapter 5, this method can only be truly useful if used in conjunction with an adaptive mesh refinement technique.

Figure 4.18: Three Dimensional Schrödinger Equation: Reflection Coefficient versus H for $w = 4$ and matter distribution hitting *side* of computational box.
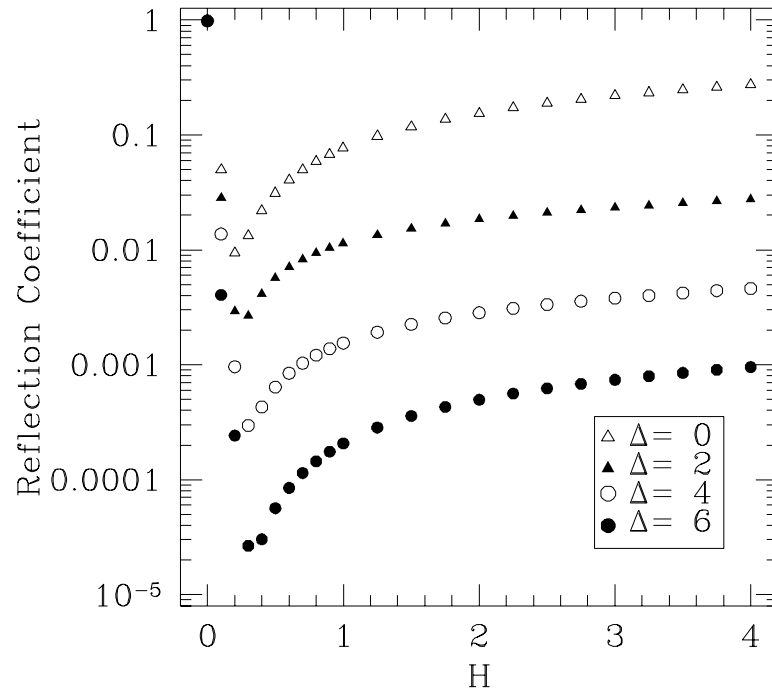
Figure 4.19: Three Dimensional Schrödinger Equation: Reflection Coefficient versus H for $w = 6$ and matter distribution hitting *side* of computational box.
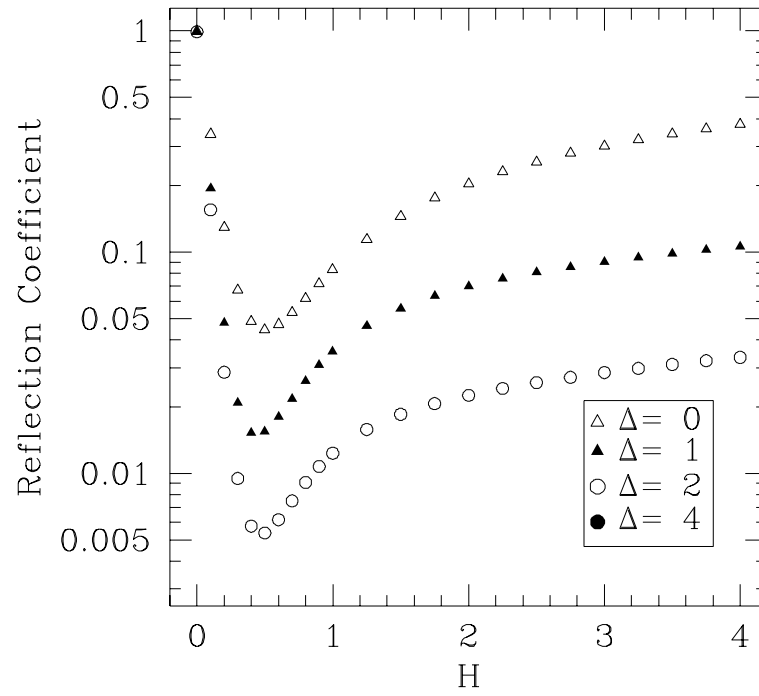
Figure 4.20: Three Dimensional Schrödinger Equation: Reflection Coefficient versus H for $w = 2$ and matter distribution hitting *edge* of computational box.
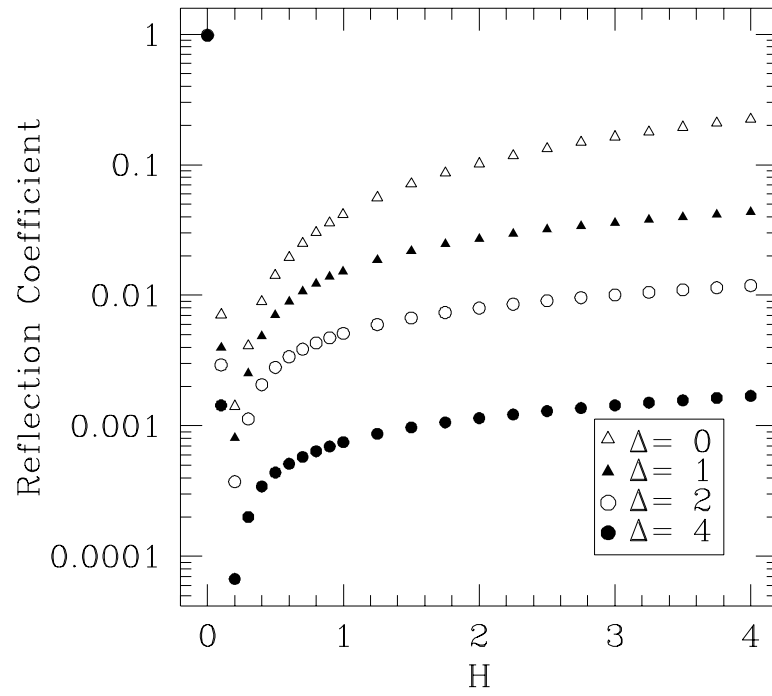
Figure 4.21: Three Dimensional Schrödinger Equation: Reflection Coefficient versus H for $w = 4$ and matter distribution hitting *edge* of computational box.
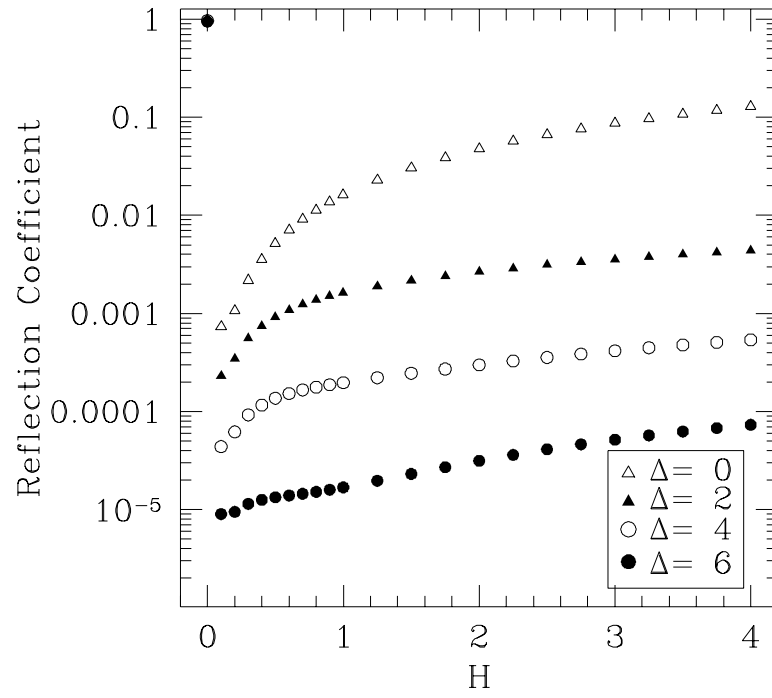
Figure 4.22: Three Dimensional Schrödinger Equation: Reflection Coefficient versus H for $w = 6$ and matter distribution hitting *edge* of computational box.
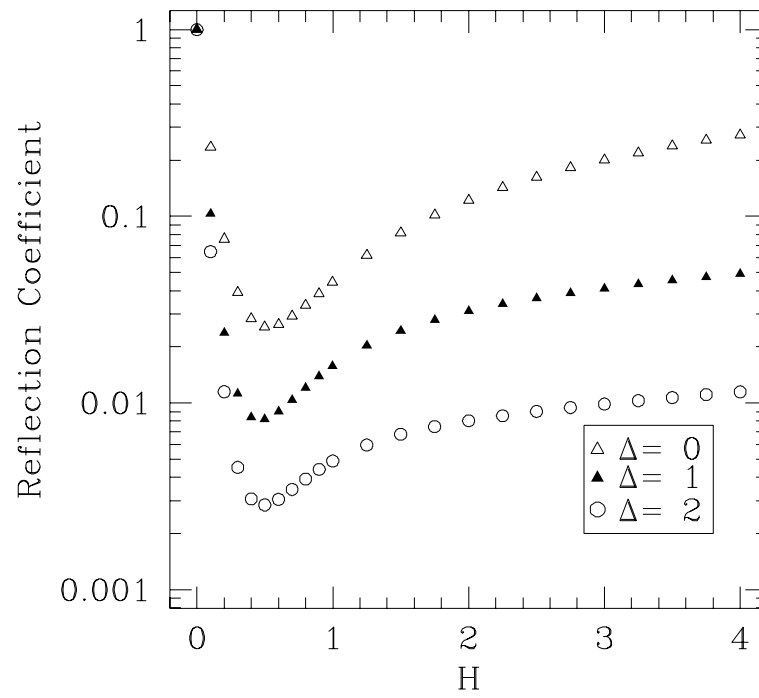
Figure 4.23: Three Dimensional Schrödinger Equation: Reflection Coefficient versus H for $w = 2$ and matter distribution hitting *corner* of computational box.
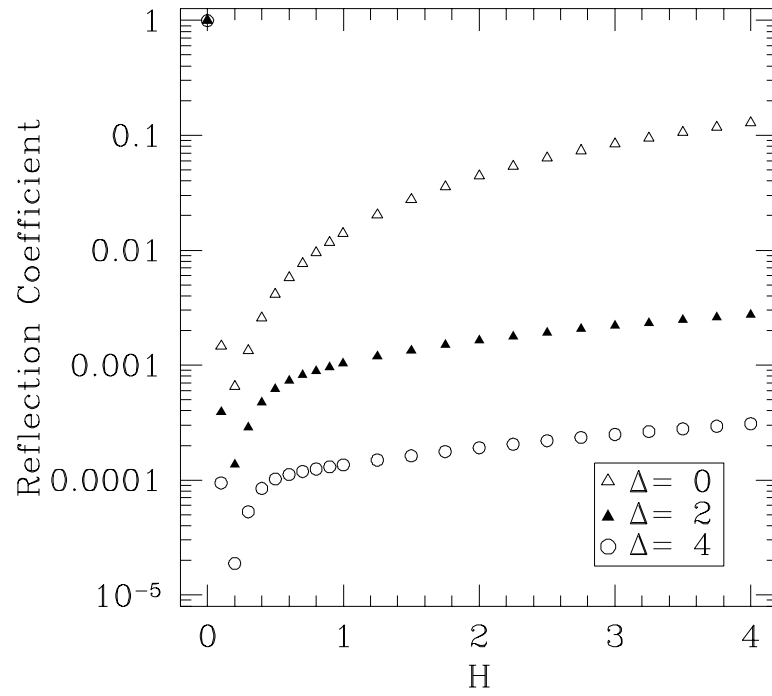
Figure 4.24: Three Dimensional Schrödinger Equation: Reflection Coefficient versus H for $w = 4$ and matter distribution hitting *corner* of computational box.
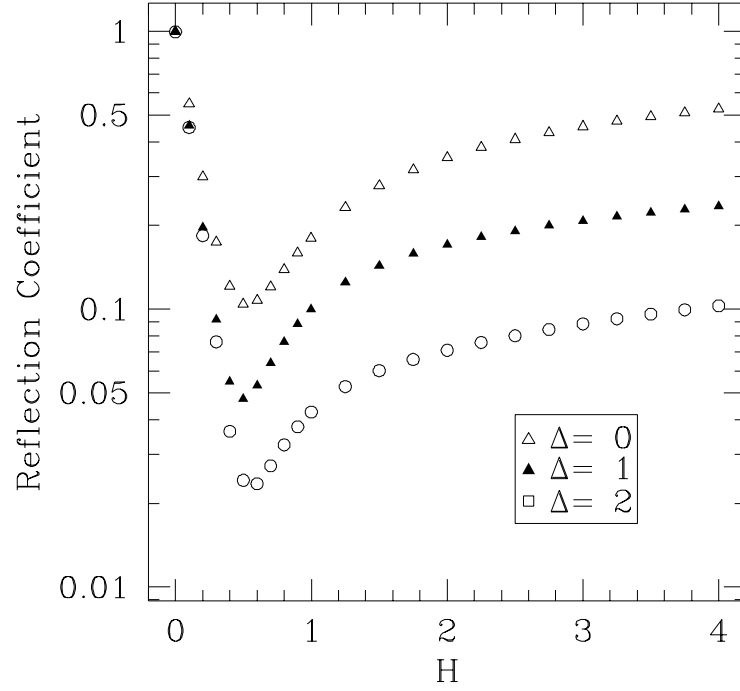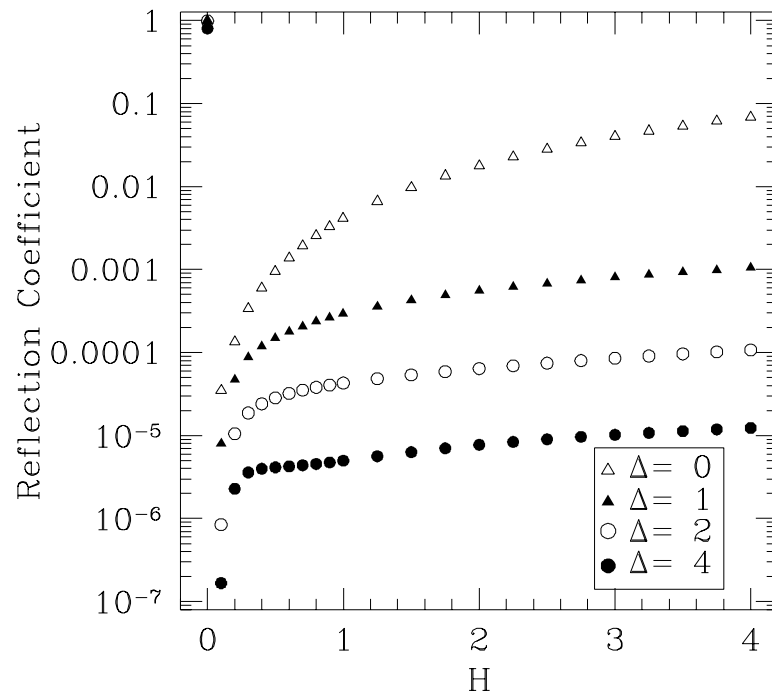
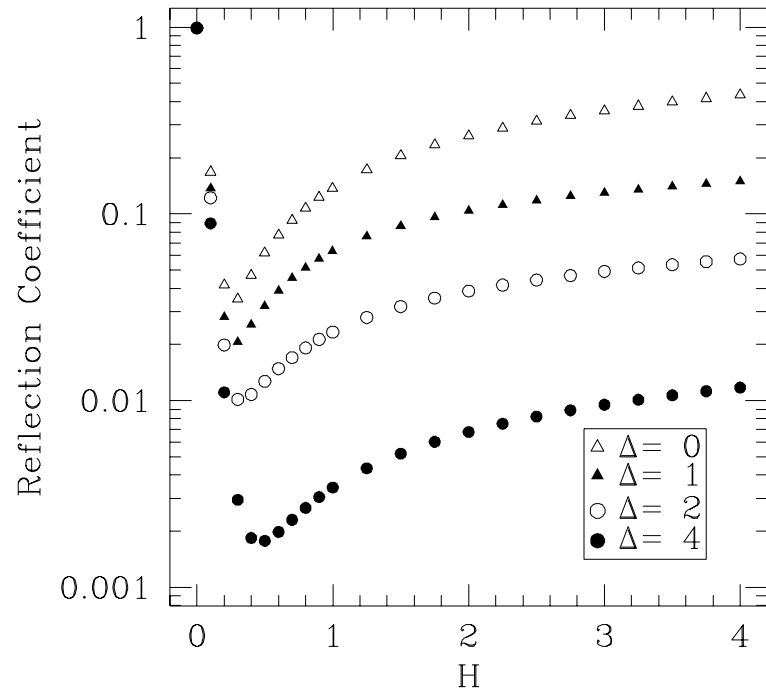Figure 4.25: Three Dimensional Schrödinger Equation: Reflection Coefficient versus H for $w = 6$ and matter distribution hitting *corner* of computational box.

Chapter 5

Physical Results

This chapter discusses the initial results of a study of Newtonian boson stars using the numerical techniques presented in the previous chapters. There were three questions I wanted to answer about the dynamical behavior of the stable solutions to the Schrödinger equation. One was: if the boson stars were given linear momentum how similarly would they behave to Newtonian point masses? The next question, which depends on the answer to the first, was: can I make a boson star orbit about a fixed central potential? The final question was: how do boson stars, which have been altered so that they can satisfy the 'quantum whirlpool'[14] condition discussed in Chapter 2, behave? The answers were quite interesting but not unexpected. Before I describe these results , I give the results of a Newtonian scaling law which shows that no matter how massive a boson star is, the evolution of the star will always be the same when the rescaling is taken into account.

5.1 Radial and Mass Scaling of Boson Stars

Since the physics for boson stars discussed in this thesis lies in the Newtonian regime, no matter what the central density of the eigenvalue solution for a boson star, the time dependent behavior of any initial set of data will always

give a solution which is the same after rescaling. In order to assure this, one must scale the dynamical parameters, such as momentum, in relation to the central density of the boson star. This is because the central density determines the mass and size of the star. For these purposes I define the size of a boson star to be the radius of a star which contains 99% of the total mass of the scalar field.

Thus I seek a scaling law for the radius of a boson star which tells how to scale computational parameters such as the overall size of the computational domain and the resolution of the mesh and dynamical parameters such as momentum in order to obtain similar results when changing the initial central density of the boson stars. Through a computational study of solving the eigenvalue problem, (3.10) and (3.11), for different central densities, I found that the radius which contains 99% of the mass of a boson star scales as:

$$R_{star} = 4.82 \left(\rho(r = 0) \right)^{-\frac{1}{4}} \tag{5.1}$$

and the mass contained within that radius scales as:

$$M_{star} = 25.6 \left(\rho(r = 0) \right)^{\frac{1}{4}}. \tag{5.2}$$

Figure 5.1 shows a logarithmic plot of the radius of a boson star from which the above scaling law was determined. The plot is over a large range of densities with a slope of $-\frac{1}{4}$ which is how the above scaling law was determined. Figure 5.2 shows the scaling law of the mass of a Newtonian boson star for a large range of densities. The plot has a slope of $\frac{1}{4}$ which gives the scaling law for the mass of a star. This is the same result found by Ruffini and Bonazzola in 1969 [48]. However, they were looking at the problem from the opposite

standpoint. They wanted to determine the central density of a self gravitating bose condensate in its ground state given the number of boson which comprise the condensate.

With the large range of densities given in the plots, one might wonder where the densities become relativistic. This would then give a regime for which the results of this chapter are valid. As one will recall from chapter 2, the density is dependent on the square of the mass of the boson particle making up the self gravitating bose condensate. Thus whatever one chooses for the mass of the particle will determine where the dynamics of boson stars must be described by Einstein's equations coupled with the massive Klein-Gordon equations. Thus the results of this chapter are physically meaningful because of the similar behavior of the scalar field in the Newtonian regime and because the mass of a particular boson being studied will determine the regime in which a Newtonian approximation is valid.
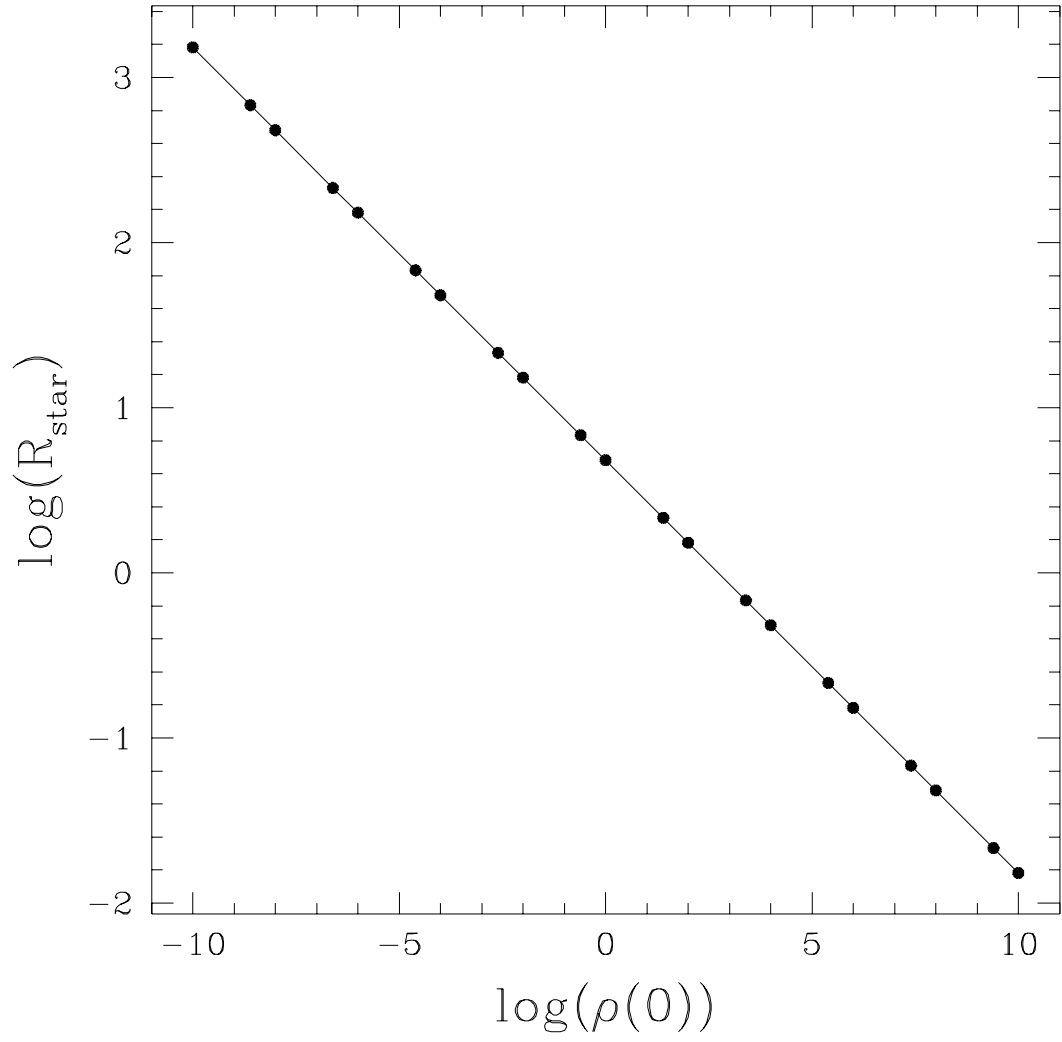
Figure 5.1: Scaling of the radius of a boson star as a function of the central density.
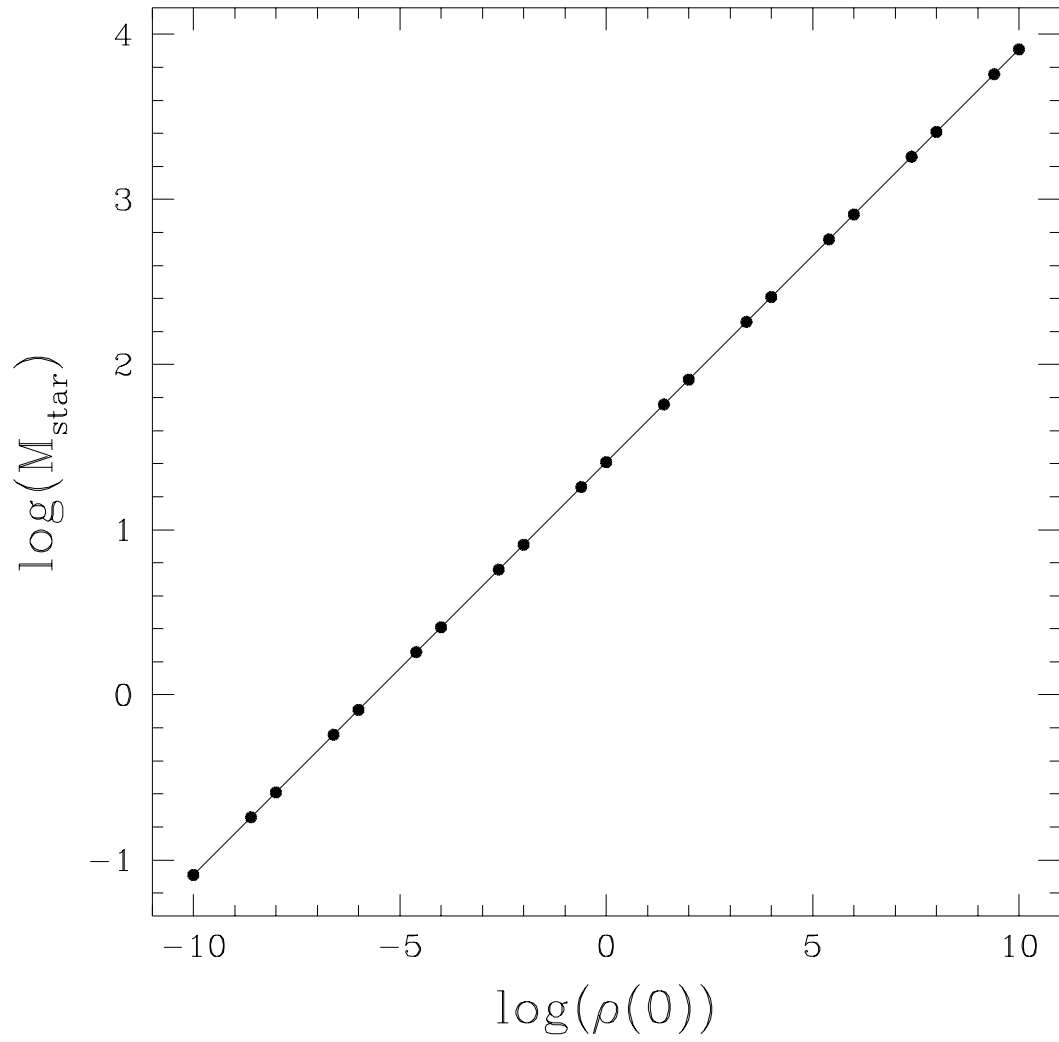
Figure 5.2: Scaling of the mass of a boson star as a function of the central density.

5.2 Boson Stars with Linear Velocity

A short description of how to give a boson star initial momentum was discussed in Chapter 3. There it is stated that to give a momentum, $\mathbf{p}$, to an initial state, one simply convolves the complex wave function $\phi(\mathbf{x}, 0)$ by the factor $\exp(i\mathbf{p}\cdot\mathbf{x})$. However, one must realize that the initial data is evolved by the difference form of the differential equation:

$$i\frac{\partial \phi}{\partial t} = -\frac{1}{2m}\nabla^2 \phi + mV\phi \qquad (5.3)$$

where in this case $m = 1$. Thus $\mathbf{p}$ is actually a velocity, $\mathbf{v}$, and so the initial momentum of a boson star is $M_{star}\mathbf{v}$.

The three plots of position versus time, Figures 5.3-5.5, show two cases discovered when giving boson stars an initial velocity in the x direction. They show the center of mass trajectory of a boson star with $\phi(r = 0, t = 0) = 1.0$ given an initial velocity together with the trajectory of a point like Newtonian mass with the same mass and initial velocity of the boson star computed on 257×129 computational mesh with physical width $64.0 \times 32.0 \times 32.0$. In figure 5.3 the star has been given an initial velocity of $v_x = 0.1$. The trajectory of the center of mass of the star is shown in comparison with that of a point like Newtonian particle with the same mass. As one can see the initial parts of the trajectories are quite similar, but as time goes on the center of mass of the boson star begins to accelerate. In figure 5.4, the boson star is given an initial velocity of $v_x = 1.0$ which from equations (3.3) and (3.4) means that it is traveling at the speed of light. As one can see, its initial trajectory is nearly the same as the Newtonian point mass but in time the center of mass accelerates slightly. In figure 5.5, the star has been given a velocity of $v_x = 10$. The plot

shows that the velocity of the center of mass is substantially less than that of the point Newtonian mass but does stay constant in time.

The results for the $v = 0.1$ and $v = 1.0$ show that the errors acquired from the integration of the difference equations become unacceptably large. One can see this by realizing that the trajectory plot for $v = 0.1$ has over three times as many time integration steps on the same computational grid as the $v = 1$ trajectory plot. In both plots the trajectories of the point mass and the boson star are initially quite similar but begin to diverge in time, and it is apparent that this divergence of the paths becomes quite large around $t = 40.0$. The main source of these errors are probably due the boundary conditions for the finite difference equations.

To understand what is occurring in the $v = 10.0$ plot, figure 5.5, one needs to refer back to the hydrodynamical analogy discussed at the end of chapter 2 and refer to the contour plots, 5.6, 5.7 and 5.8. Figure 5.6 is a contour plot of the density of the boson star, $\rho = \phi\phi^*$, for $v_x = 0.1$ with contours at $\rho = 0.5, 0.1, 0.05, \ldots, 5 \times 10^{-5}$. This shows the boson star moving in the positive x direction, and as one can see the shape of the star is virtually the same at $t = 0.0$, $t = 50.0$ and $t = 100.0$ except at the $\rho = 1.0 \times 10^{-5}$ contour. Contour plot 5.7 for $v = 1.0$ shows that the contours down to $\rho = 1.0^{-4}$ remain virtually the same at $t = 0.0$, $t = 10.0$ and $t = 20.0$. Contour plot 5.8 shows that the density of the boson star is initially symmetrical but becomes quite distorted and flattened in time with the $\rho = 0.5$ contour no longer present at $t = 5.0$ and the $\rho = 0.01$ contour no longer present at $t = 10.0$. Physically, this should not be possible as there should be no difference between a boosted boson star and a boosted observer. The velocity $v = 10.0$ means that the initial data

for the scalar field was convolved by the complex function, $\exp(i10x)$. Thus in the x direction the complex and imaginary parts have 10 times as many oscillations as the $\mathbf{v} = (1, 0, 0)$ case. Thus the mesh width of $h = 0.25$ used for these calculations can not smoothly resolve the real and imaginary parts of $\phi(\mathbf{x}, t)$. This causes the error which is seen in the distortion of the density. It also means that the potential will be distorted which as one can see from the right hand side of equation (2.58) can cause the star to dissipate in time. This explains why the velocity of the star is not actually 10.0 and why the star flattens out in time.

These results show that at velocities around and less than $v = 1.0$, boson stars behave like point masses. However, as the integration continues, the computational errors accumulate and begin to dominate the velocity of the star. Figure 5.9 shows the difference between the trajectories of the star and the point mass for three different mesh resolutions. As one can see, at later times, the difference between the point mass trajectory and the boson star trajectory grow smaller for the finer resolution runs. This indicates that the errors in the computational solution are due to the finite difference errors discussed in Chapter 3.

At this point, it is appropriate to give a caveat for the use of approximate boundary conditions. The runs for the above figures needed the solution of Poisson's equation for the Newtonian potential. The first time these calculations were done, Dirichlet boundaries were used in the numerical solution of Poisson's equation. This did not appear to affect the solution of the $v = 1.0$ and $v = 10.0$ cases. However, for the long time solution of $v = 0.1$, the trajectory is shown in figure 5.10 along with that of a point mass. As one can

see, the boson star actually slows down and begins moving in the negative x direction. Thus the error due to the approximate boundary condition causes the computational results to have no physical relevance. The previous runs were done using a Robin boundary condition:

$$\frac{\partial V}{\partial r} = -\frac{V}{r} \tag{5.4}$$

which is really only valid as $r \rightarrow \infty$ but is obviously a better approximate boundary condition than the Dirichlet boundary condition.

Figure 5.3: Trajectories of a Newtonian point mass and a boson star with initial central density of $\rho = 1$. Both have an initial velocity $v = v_x = 0.1$.

Figure 5.4: Trajectories of a Newtonian point mass and a boson star with initial central density of $\rho = 1$. Both have an initial velocity $v = v_x = 1.0$.

Figure 5.5: Trajectories of a Newtonian point mass and a boson star with initial central density of $\rho = 1$. Both have an initial velocity $v = v_x = 10.0$.
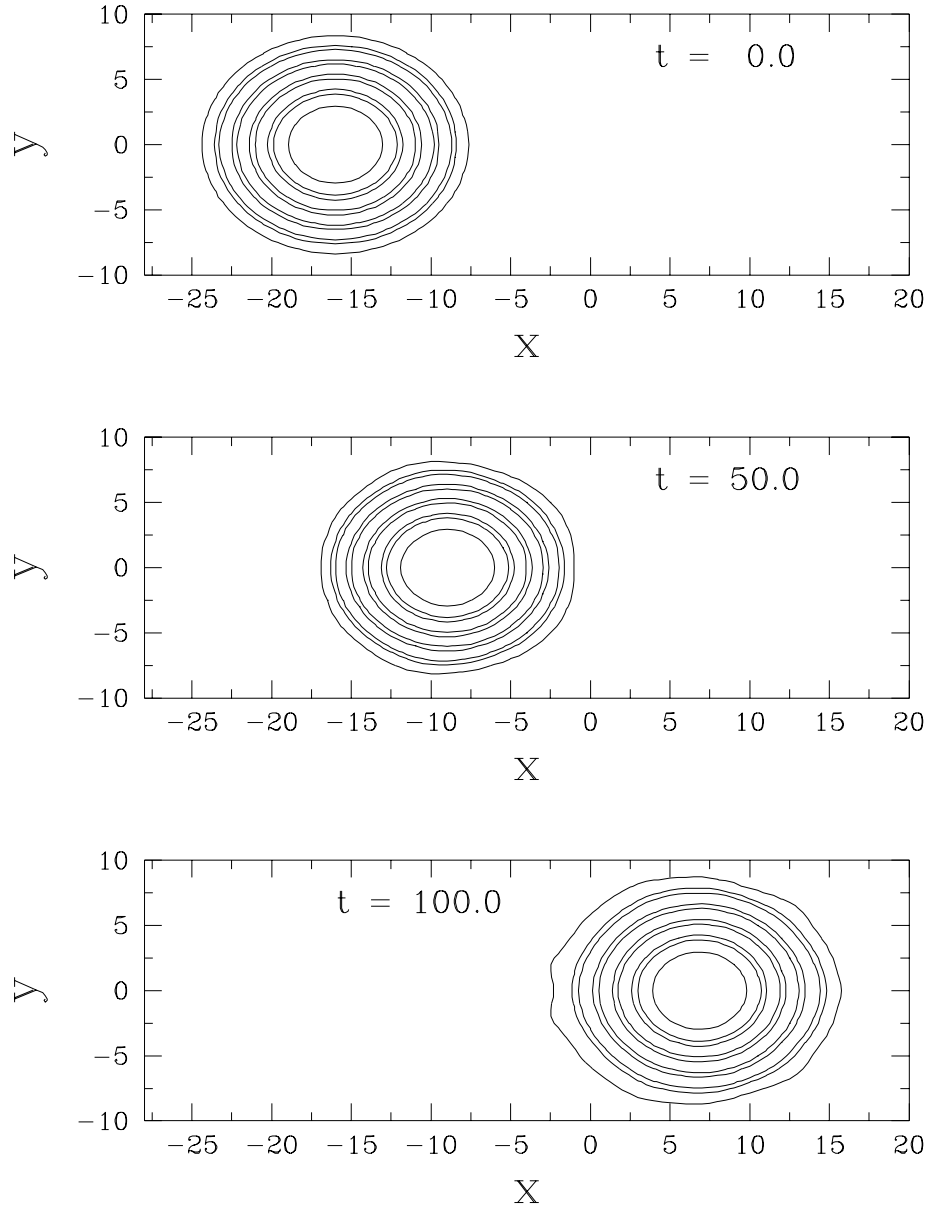
Figure 5.6: Contour plots of mass density at different times for a boson star given initial velocity $v_x = 0.1$. The contours are at densities of $0.5, 0.1, 0.05, \ldots 5 \times 10^{-6}$ and are highest in the center of the star.
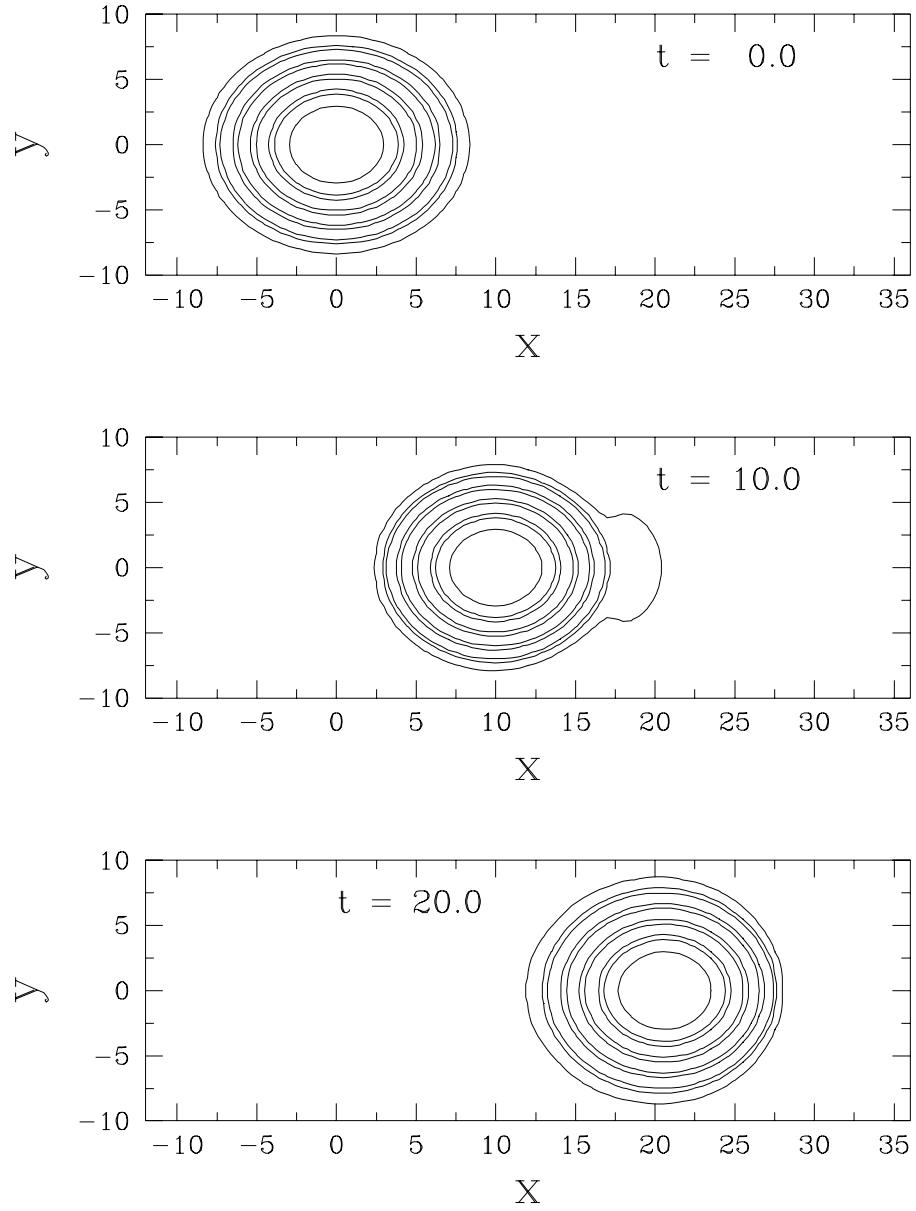
Figure 5.7: Contour plots of mass density at different times for a boson star given initial velocity $v_x = 1.0$. The contours are at densities of $0.5, 0.1, 0.05, \ldots 5 \times 10^{-6}$ and are highest in the center of the star.
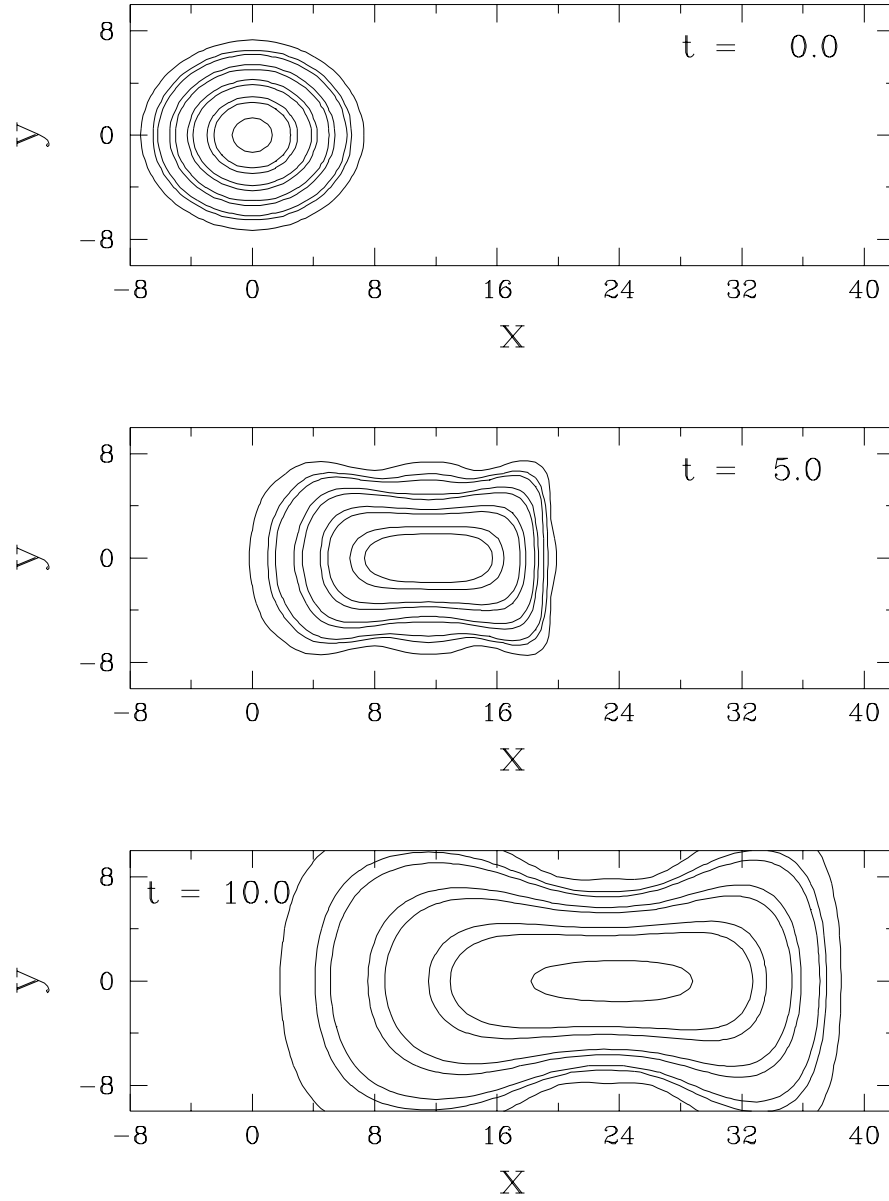
Figure 5.8: Contour plots of mass density at different times for a boson star given initial velocity $v_x = 10.0$. The contours are at densities of $0.5, 0.1, 0.05, \ldots 5 \times 10^{-6}$ and are highest in the center of the star.
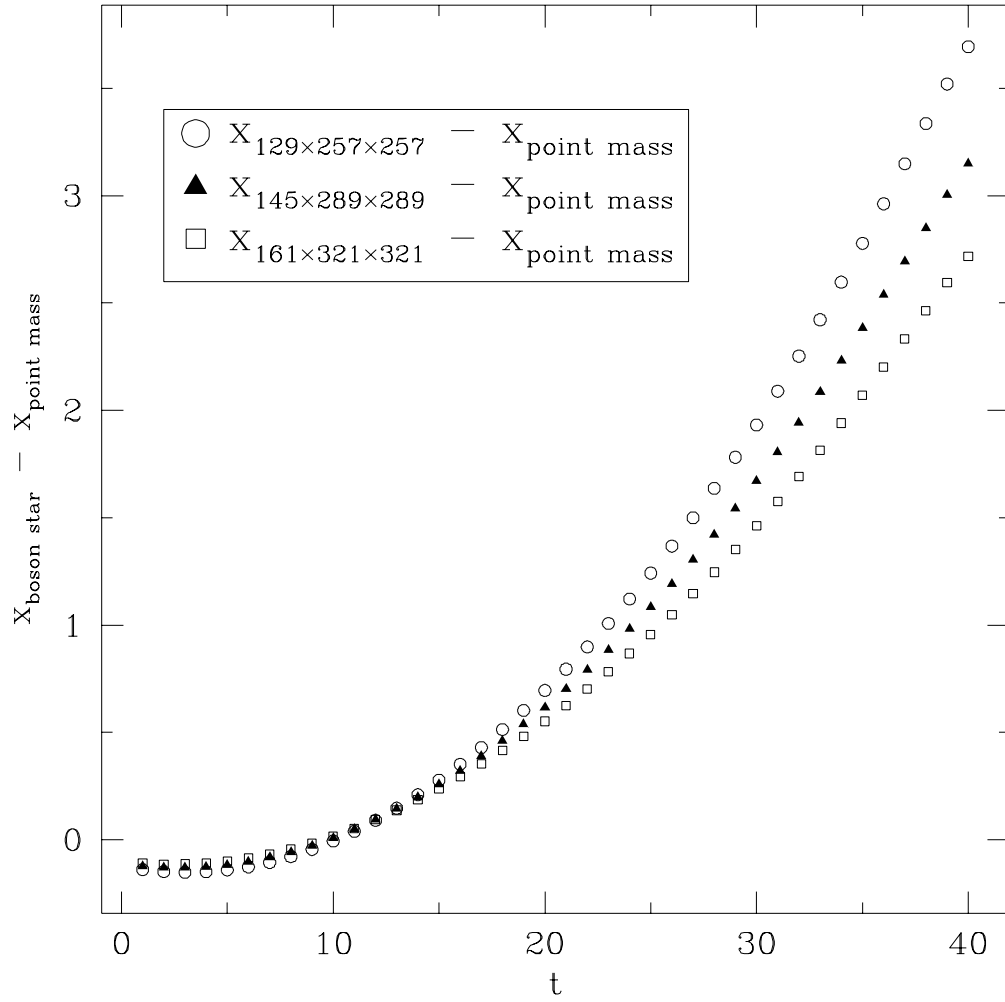
Figure 5.9: Difference of the trajectory of a Newtonian point mass and a boson star with an initial central density of $\rho = 1$ and an initial velocity $v = v_x = 1.0$ for three different computational mesh resolutions.
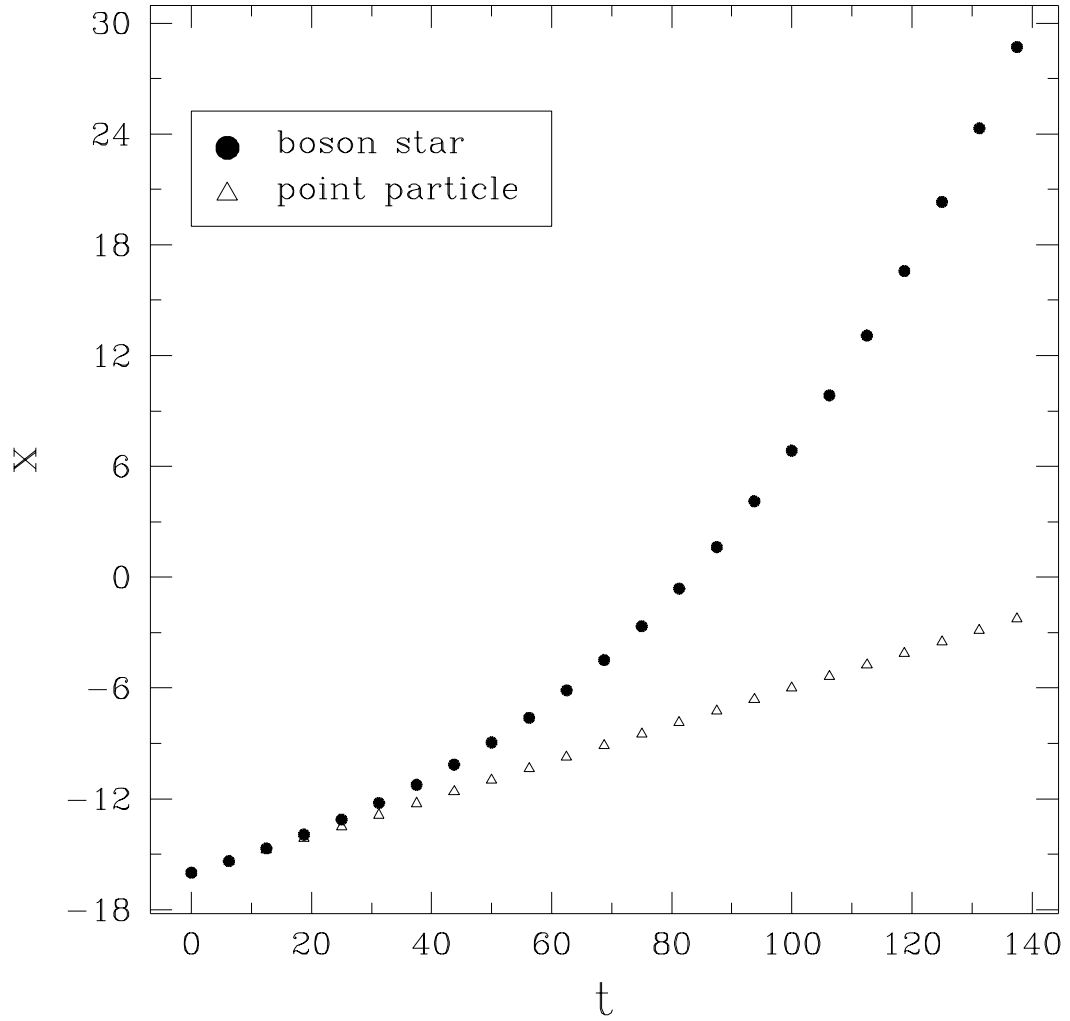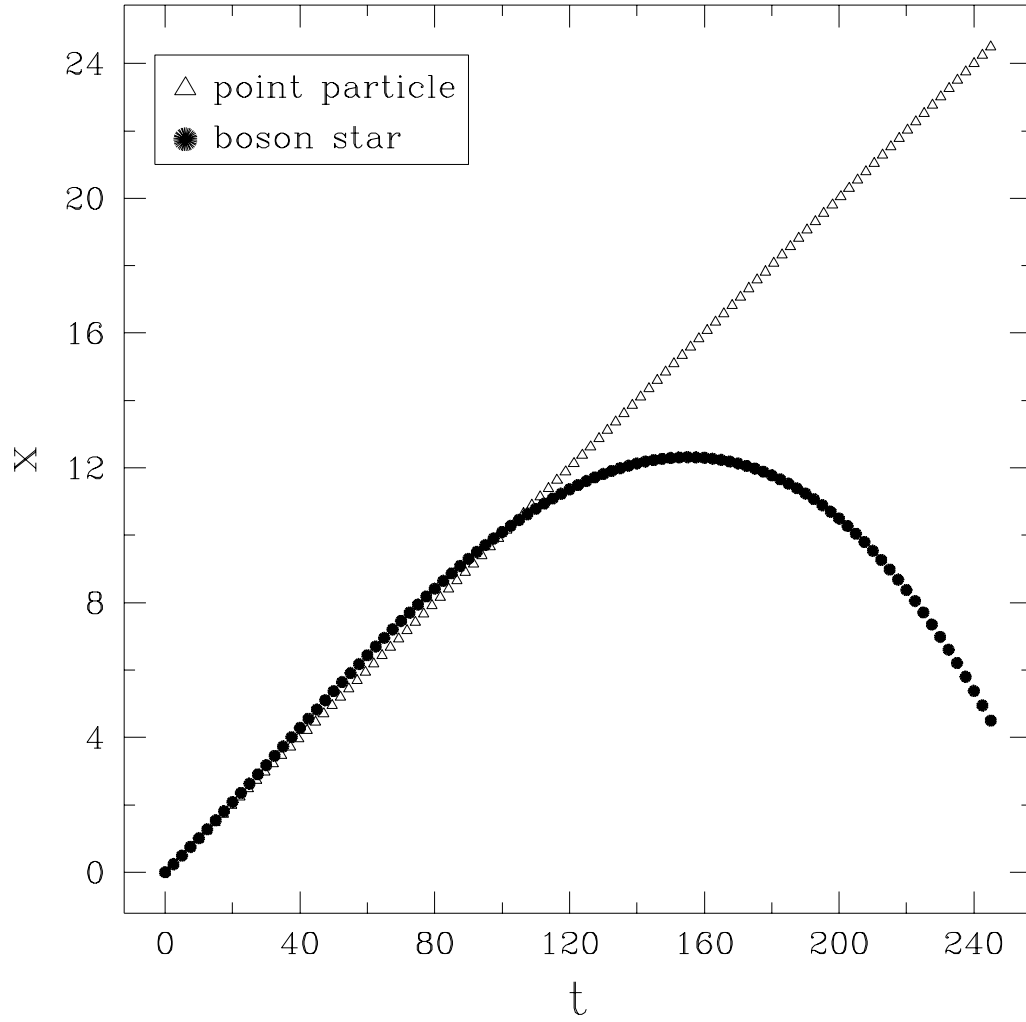
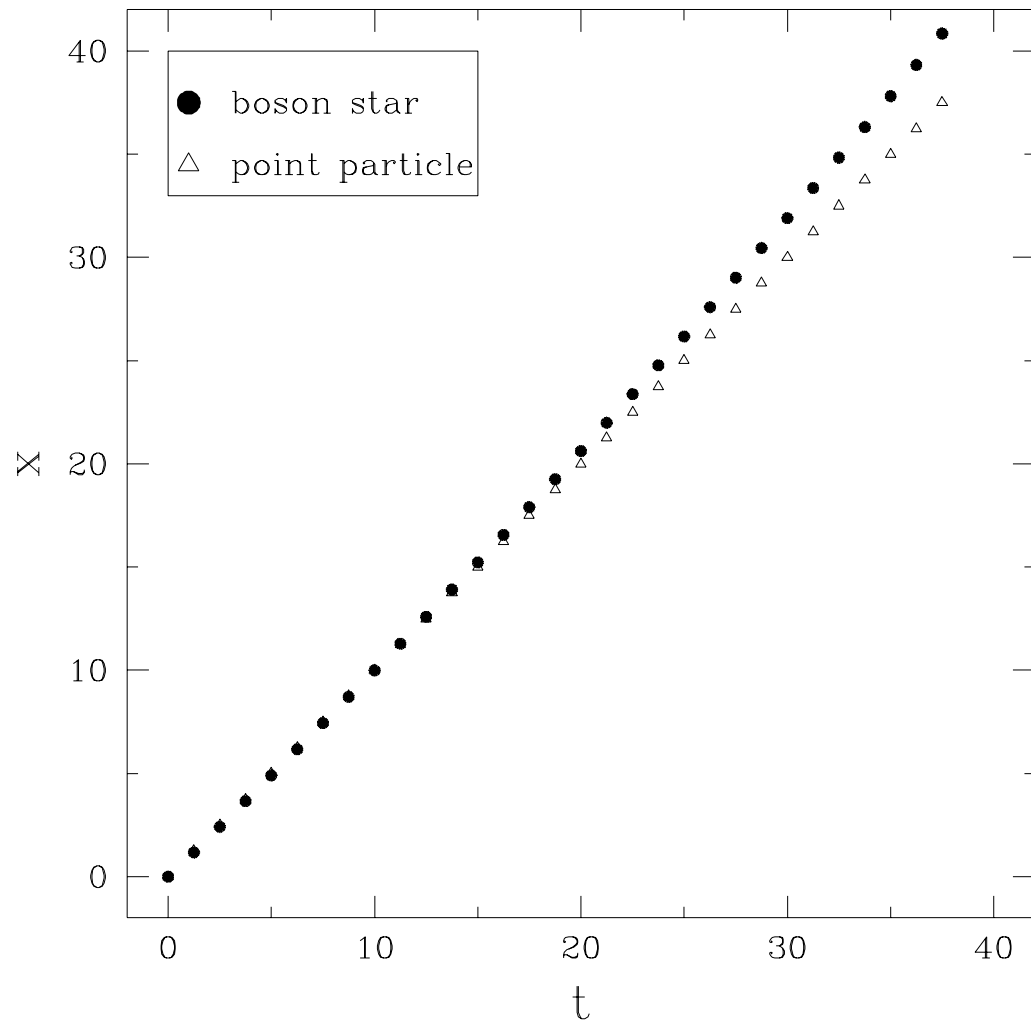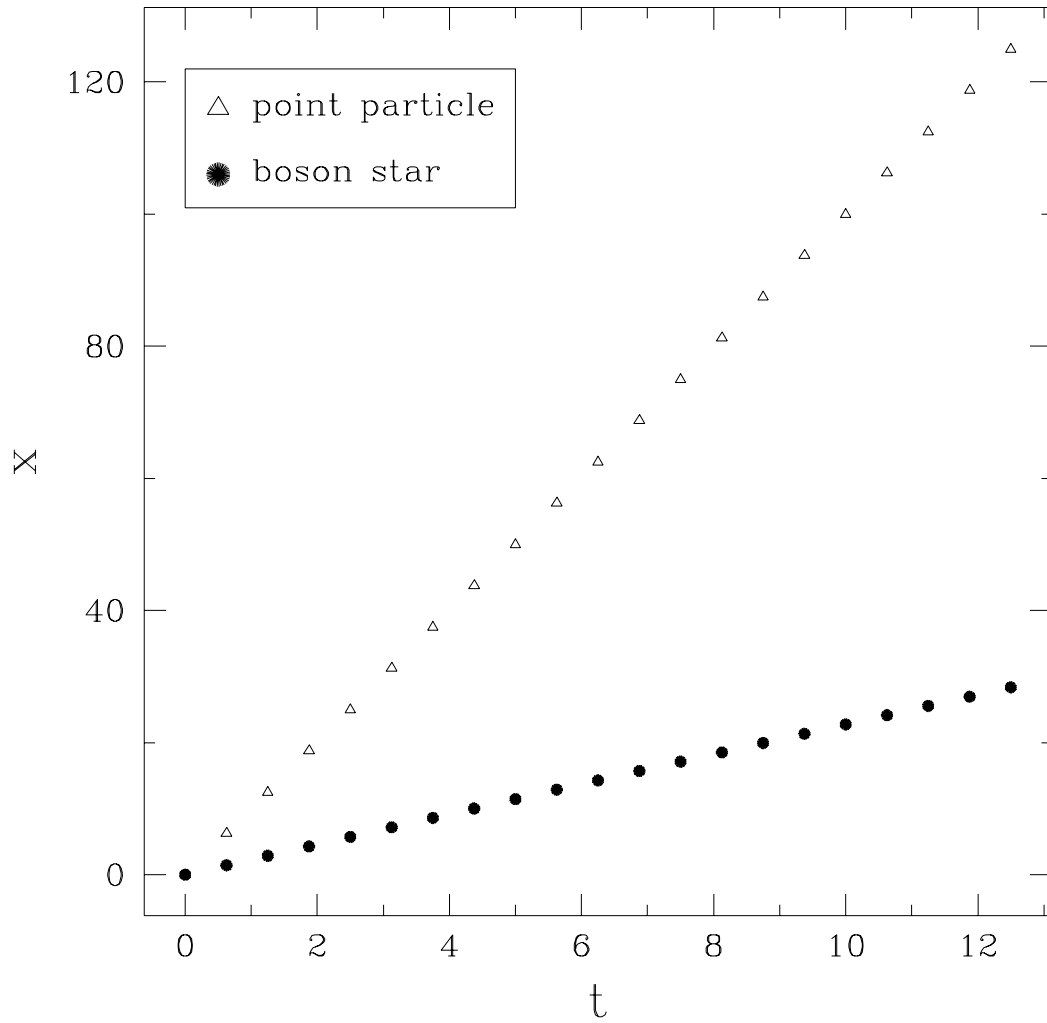Figure 5.10: Trajectories of a Newtonian point mass and a boson star with initial central density of $\rho = 1$. Both have an initial velocity $v_x = 0.1$. The trajectory of the boson star was made from a computation using a Dirichlet boundary condition.

5.3   Boson Stars in a Central Potential

This section discusses the case of stars given an initial velocity as in the previous section but now the stars are under the influence of not only their own potential but also a constant central potential:

$$V_{central} = -\frac{M_{central}}{r_{central}} \tag{5.5}$$

where $M_{central}$ is a constant and $r_{central}$ is the distance from a point on the computational grid to the center of the potential. The value of $V_{central}(r_{central} = 0)$ is a 1st order extrapolation from two radial points near the center of the potential.

The results in this section are from three cases. The central potential for all three cases is centered at the origin of the spatial grid with $M_{central} = 100$,[1] and the initial central densities of the boson stars are 1. The boson star of the first case is centered initially at the point $(x = 0, y = 1000, z = 0)$ with an initial velocity $\mathbf{v} = (0.25, 0.0, 0.0)$. The figure 5.11 shows a comparison of two y versus x trajectories for this case. One trajectory is for the center of mass of the boson star while the other is for a point mass with the same initial velocity and position as the boson star. As the plot, shows the initial part of the trajectories are very similar, but the boson star moves further in the x direction than the point mass while moving less in the y direction. Thus the central potential does have a definite effect on the boson star but the errors of the difference scheme seen in the previous section are dominating the motion of the star.

---

[1] This mass is roughly four times that of the mass of the boson star for these three cases.

The 2nd case studied in this section is of a boson star centered at $(x = 0, y = 100, z = 0)$ with an initial velocity, $\mathbf{v} = (1.0, 0.0, 0.0)$. The figure 5.12 shows a comparison of the trajectories of the center of mass of the boson star and a point mass with the same initial position and velocity. In this plot, the star moves further in the y direction than the point mass. Thus the influence of the central potential on the motion of the boson star is greater than the in the first case. This is expected since the star is closer to the origin in this case.

The third case is of a boson star centered at $(x = 0, y = 16, z = 0)$ with an initial velocity of 2.5 in the x direction. This is the velocity for a circular orbit of a point mass in the central potential described above. As one sees from the plot of the trajectories of the center of mass of the the boson star and the point mass, the boson star appears to follow the trajectory of the point mass quite closely for the first third of the orbit. Afterwards the tidal forces on the star begin to dominate and the center of mass quickly spirals towards the center of the central potential.

The two sets of contour plots of density in the $z = 0$ plane give an indication of how the central potential begins to dominate the dynamics of the boson star. Figure 5.14 shows $\rho = 0.5, 0.05, \ldots, 5 \times 10^{-5}$ contours of the boson star for the 2nd case at times $t = 0$ and $t = 25$. As one sees, the boson star is slightly distorted from its original shape in a similar fashion to the $v_x = 1$ linear momentum case in the previous section. Thus one can again conclude that the central potential has a smaller effect on the trajectory of the boson star than the point mass because of errors occuring in the finite difference equations used to evolve of the star.

The second set of contour plots, 5.15, shows the domination of the tidal

forces of the central potential on the boson star. At time $t = 12.5$, the exterior contours are quite distorted from their $(t = 0)$ original shape. The two interior contours still have a somewhat circular shape. At $t = 25$ the boson star is quite distorted from its original shape, and the central contour, $\rho = 0.5$, is now gone. At the time $t = 62.5$, most of the mass of the star has spiraled to the center of the fixed potential while a large fraction of the mass has come in contact with the boundaries of the computational domain at $y = -32$.

Another interesting set of data from the third case is the average momenta of the system as a function of time. This can be calculated in the usual quantum mechanical way:

$$< \mathbf{p} >= -i \int \phi^* \nabla \phi d^3 x \tag{5.6}$$

which for the computational data ϕ^n_{ijk} is approximated via:

$$< p_x >= -\frac{ih^2}{2} \Sigma_{ijk} \ \phi^{n*}_{ijk} \left(\phi^n_{i+1jk} - \phi^n_{i-1jk} \right) \tag{5.7}$$

$$< p_y >= -\frac{ih^2}{2} \Sigma_{ijk} \ \phi^{n*}_{ijk} \left(\phi^n_{ij+1k} - \phi^n_{ij-1k} \right) \tag{5.8}$$

where h is the grid spacing of the computational grid. Figure 5.16 shows plots of the average momenta of the scalar field versus time. For $t < 20$ the x and y momenta follow the standard sinusoidal trajectories of an orbiting point mass, but as the tidal effects begin to dominate the solution, the momenta loose the sinusoidal patterns.

These results along with those of the previous section show that it may be impossible to have a stable boson star orbit about a central potential. The errors dominate the solution when the star is far from the central potential while tidal forces from the central potential cause disruptive tidal effects on the star

when the star is close to the central potential. A better study could be made with an adaptive mesh computational scheme which will allow one to resolve the high density parts of the star while using relatively few computational grid points in areas of little physical activity.
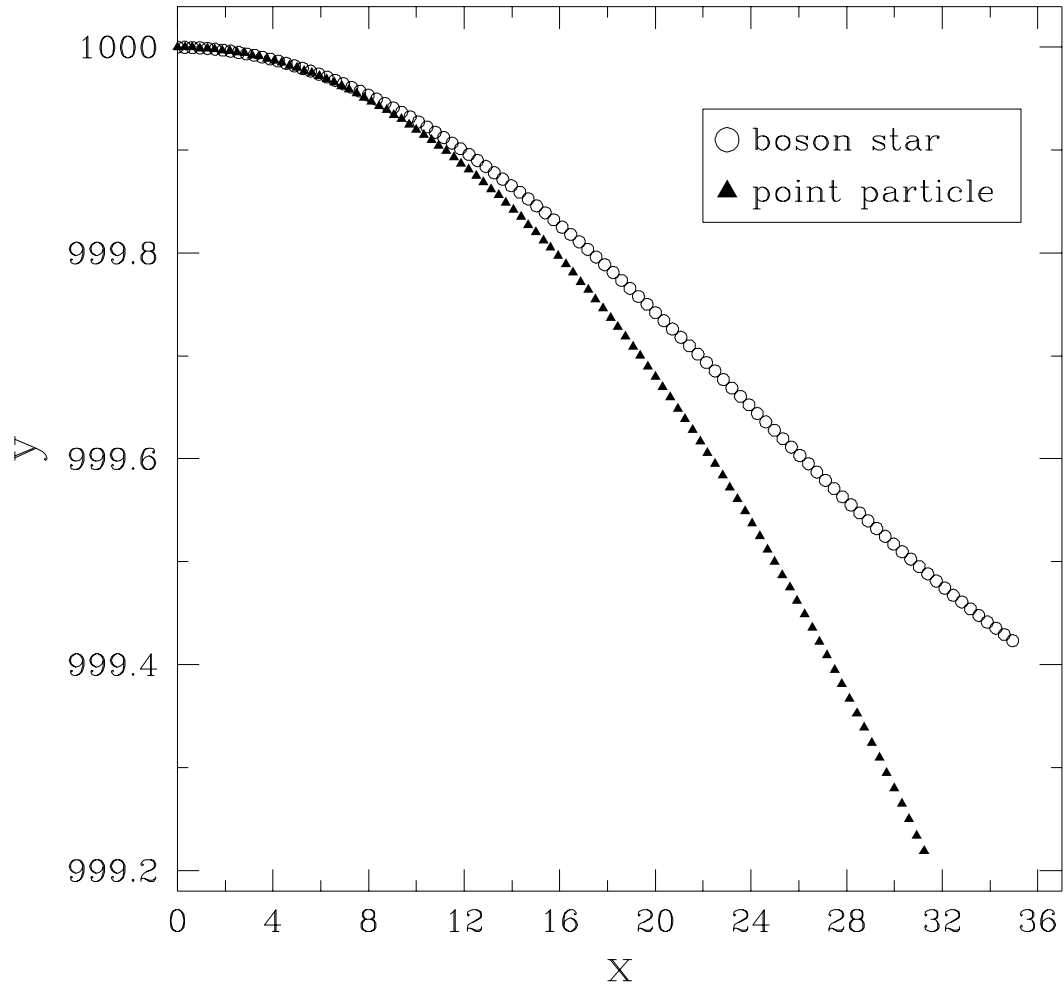
Figure 5.11: Trajectories in the xy plane of a boson star with an initial central density, $\rho = 1$ and a Newtonian point mass whose trajectories are curved because of the central potential centered at the origin. Both the star and point mass star start with an initial velocity of $v_x = 0.25$.
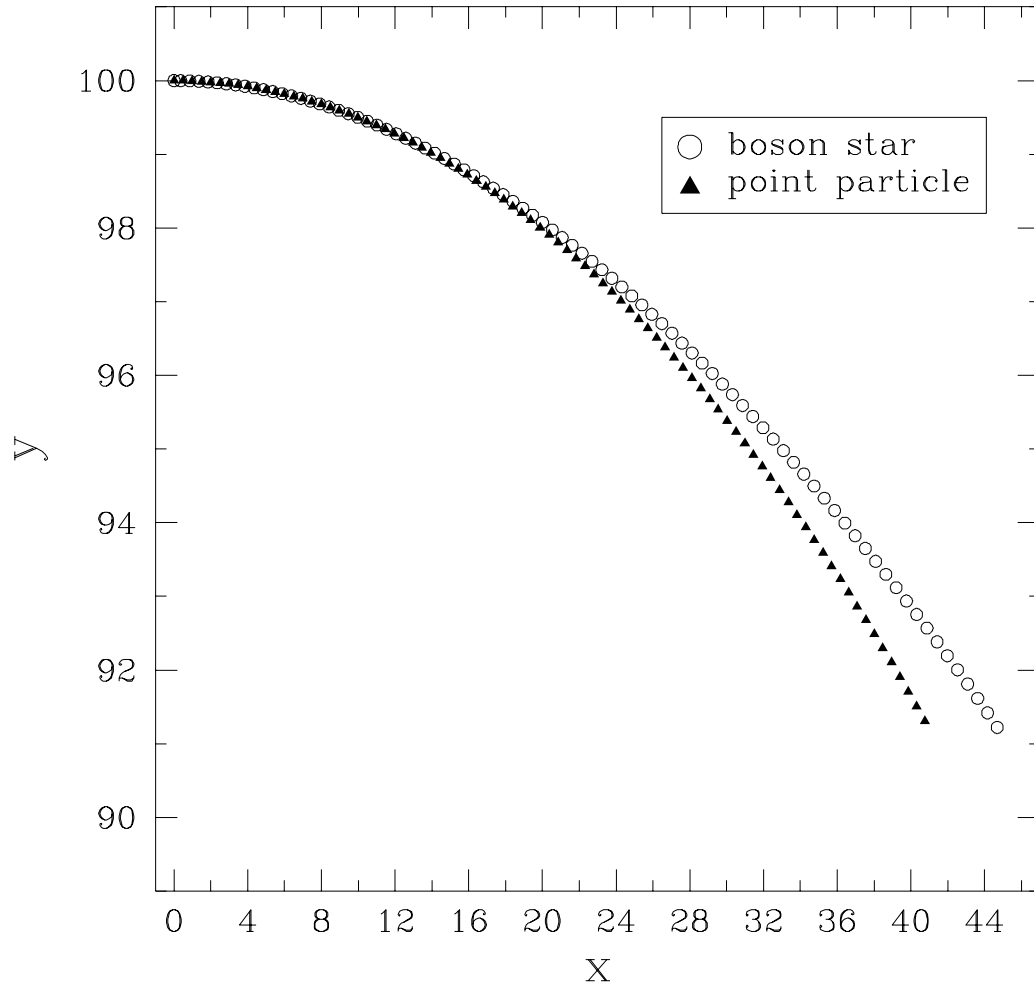
Figure 5.12: Trajectories in the xy plane of a boson star with an initial central density, $\rho = 1$ and a Newtonian point mass whose trajectories are curved because of the central potential centered at the origin. Both the star and point mass star start with an initial velocity of $v_x = 1.0$.
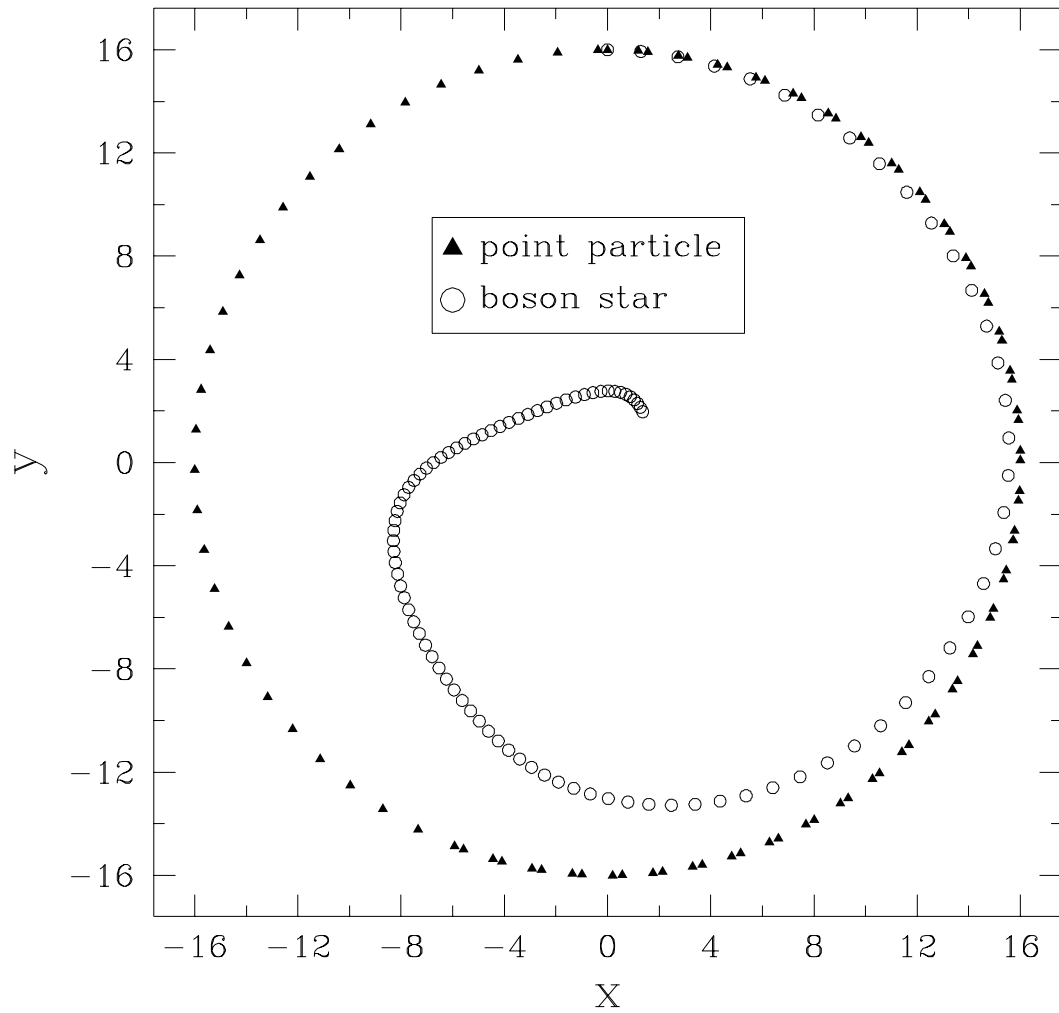
Figure 5.13: Trajectories in the xy plane of a boson star with an initial central density, $\rho = 1$ and a Newtonian point mass whose trajectories are curved because of the central potential centered at the origin. Both the star and point mass star start with an initial velocity of $v_x = 2.5$.
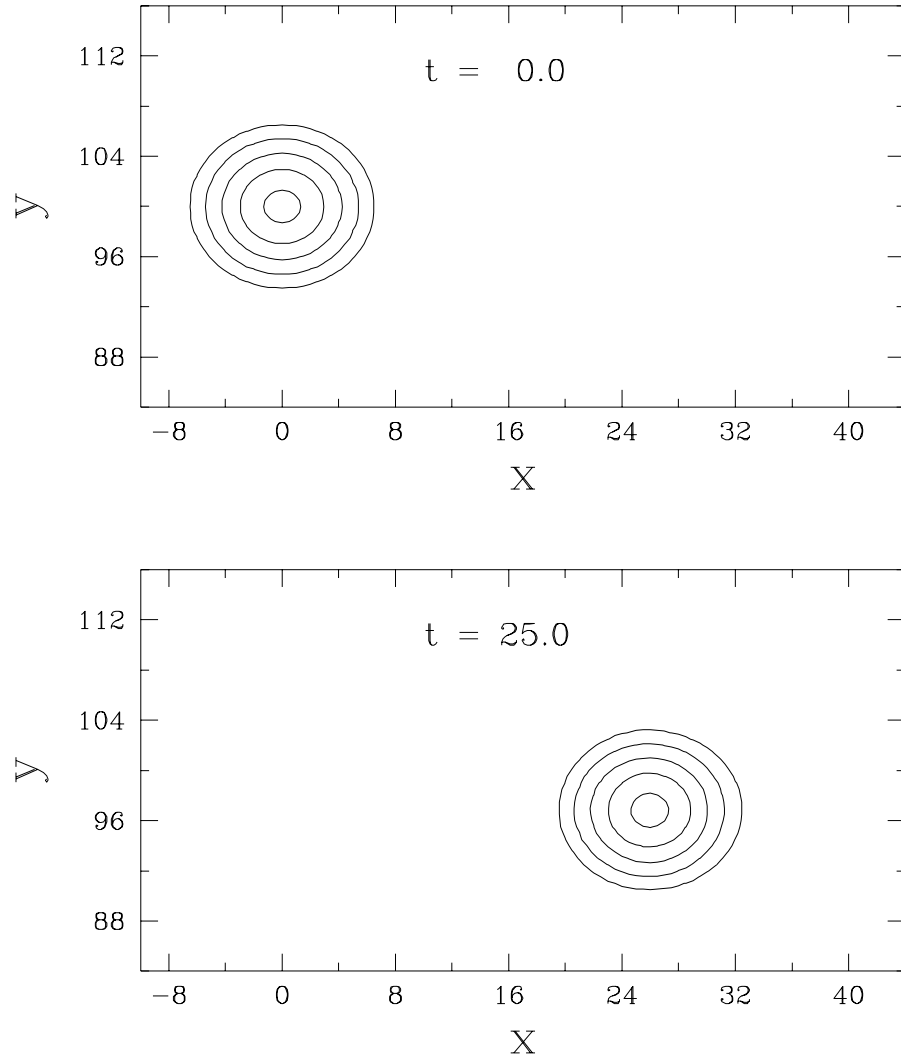
Figure 5.14: Contour plots of mass density at different times for a boson star given initial velocity $v_x = 1.0$ whose trajectory is influenced by the central potential centered at the origin. The contours are at densities of $0.5, 0.05, \ldots 5 \times 10^{-5}$ and are highest in the center of the star.
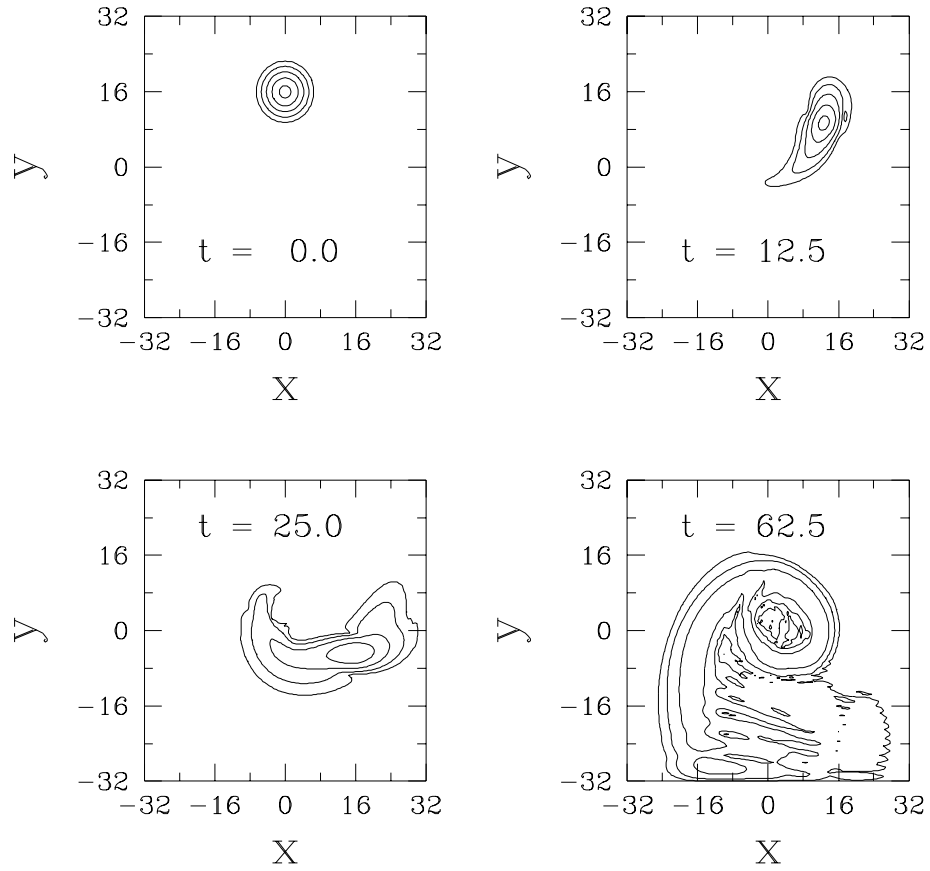
Figure 5.15: Contour plots of mass density at different times for a boson star given initial velocity $v_x = 2.5$ whose trajectory is influenced by the central potential centered at the origin. The contours are at densities of $0.5, 0.05, \ldots 5 \times 10^{-5}$ and are highest in the center of the star.
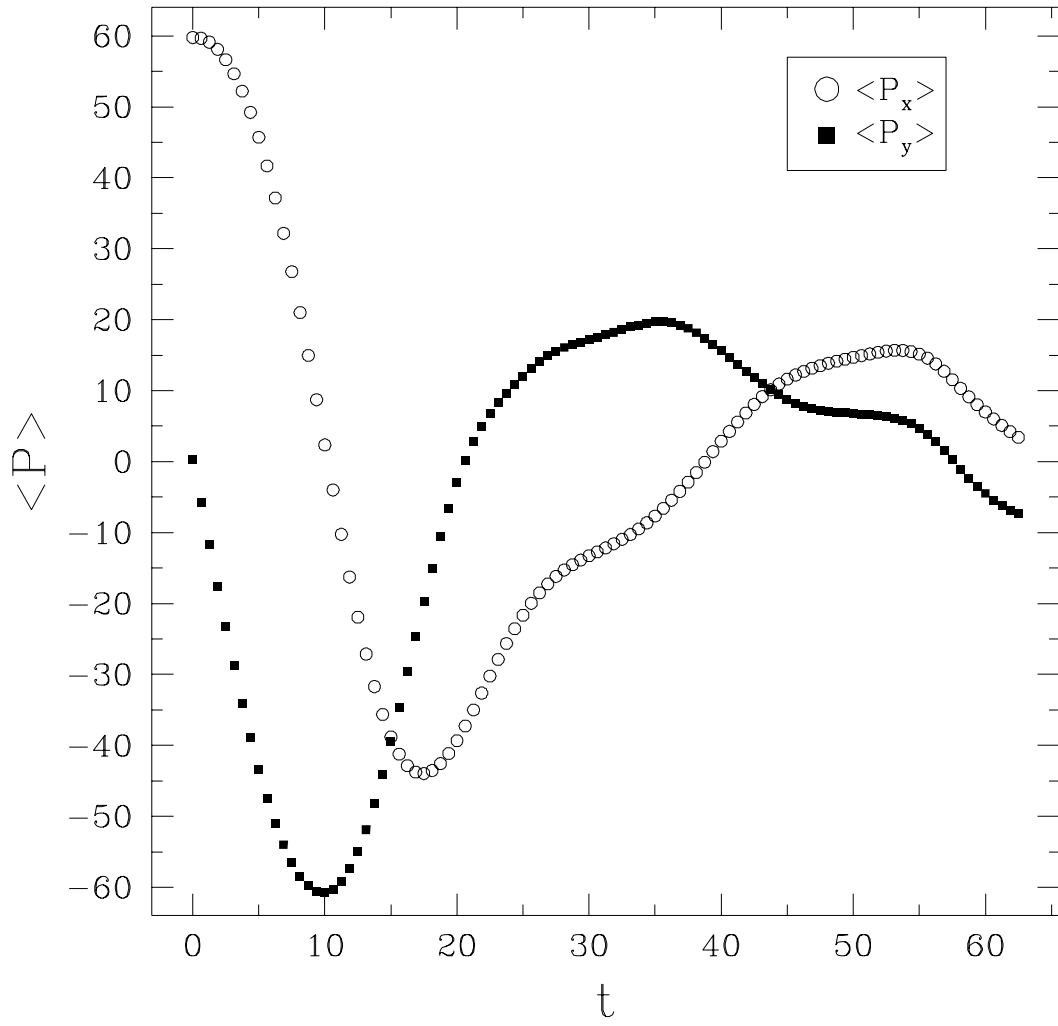
Figure 5.16: Plots of the average x and y momenta as a function of time for the boson star with an initial distance of 16 from center of the central potential and an initial velocity in the x direction of $v_x = 2.5$.

5.4   Boson Stars with Angular Momenta

As mentioned in the section 2.3, the hydrodynamical equations of the Schrödinger equation do allow rotational solutions but they must have quantized angular momenta and the central density must be zero in order to have a single-valued solution. The results for this section are for the two dimensional equivalent to the three dimensional version of equations (1.1) and (1.2). This is because it was found that smooth resolution of the dynamics of the problem is impossible even for grids with 257^3 points.[2] For the two dimensional equivalent problem a maximum of 4097^2 points is allowed.

The only part that changes in the solution of the computational differencing scheme [3] is that the eigenvalue solution to the potential V has a solution of $-C_{2d} \ln(r)$ at infinity instead of $-C_{3d}/r$. So the Dirichlet boundary condition used in solving Poisson's equation for the Newtonian potential is much more prevalent and causes the difference scheme to have $O(h)$ convergence instead of $O(h^2)$ convergence.

As one will recall from the chapter 3, to give a boson star an angular momentum $J_z = N$ in the z direction, one simply convolves the complex scalar field with the function $\exp(iN\phi)$. As in section 5.2, the Schrödinger equation being solved, equation (5.3), is for a particle mass of $m = 1$ so that N actually determines the angular velocity of the scalar field. Also since a single valued solution of the Schrödinger equation with nonzero rotation must have a central density of zero, the initial data are multiplied by the function, $1 - \exp(-r^2)$.

---

[2] This is the largest computational domain allowed for the three dimensional computational difference problem discussed in this dissertation.

[3] Besides from no longer differencing in the z direction.

Thus the initial data for a boson star with angular velocity, N, are given by:

$$\phi(\mathbf{x}, t = 0) \equiv \phi_{eigen} \left(r = (x^2 + y^2)^{\frac{1}{2}} \right) e^{iN\varphi} \left(1 - e^{-r^2} \right) \qquad (5.9)$$

where ϕ_{eigen} is the initial value solution to the two dimensional eigenvalue problem and $\varphi = \tan^{-1} y/x$.

The plot 5.17 shows the average angular momentum of a boson star with $\phi_{eigen}(r = 0) = 1$ for various values of initial angular momentum. The average angular momentum was calculated using the quantum mechanical angular momentum operator:

$$J_z = x \frac{\partial}{\partial y} - y \frac{\partial}{\partial x}. \qquad (5.10)$$

On the computational domain, the average angular momentum is calculated from:

$$< J_z > = -\frac{ih}{2} \sum_{ij} \phi_{ij}^{n*} \left(x_i \left(\phi_{ij+1} - \phi_{ij-1} \right) - y_j \left(\phi_{i+1j} - \phi_{i-1j} \right) \right). \qquad (5.11)$$

The plot shows that the average angular momentum is initially constant but drops off towards zero for all cases except for $N = 1$. The reason for this is computational, not physical, as one can see from the three sets of movies, 5.18, 5.19 and 5.20. The movies show density data for $N = 1, 2$ and 5 along the x axis from $x = -32$ to $x = 32$ with the initial data centered at the origin. The first movie shows the $N = 1$ case. Successive frames are separated by $\Delta t = 12.5$ from $t = 0.0$ to $t = 187.5$. The range of each frame is from a density of $\rho = 0.0$ to a density of $\rho = 0.09$ while the data in the initial frame has a maximum $\rho_{max} = 0.29$. The behavior of these 'quantum whirlpools' is quite interesting. There is a nearly periodic ringing of the data in which density flattens out due to the centripetal acceleration but then gravitational forces

pull the matter back and then the process repeats itself. This all occurs while the average angular momentum stays nearly constant.

Figures 5.19 and 5.20 show the evolution of density profiles with $N = 2$ and $N = 5$ respectively. The domains of each frame are the same as in figure 5.18 while the range goes from $\rho = 0.00$ to $\rho = 0.01$. In figure 5.19 the time steps of each successive frame are in increments of 1.25 with the first frame starting at time $t = 0.0$ and the last frame ending at time $t = 18.75$. As one sees, the matter distribution begins to flatten out as in the first movie, but the larger angular velocity forces more matter out to the computational boundary. Subsequent frames show that matter is reflected off the computational boundary. The annihilation boundary layer takes up 23% of the computational domain for these runs but appears to have little effect. Actually, in this case, it would be better to increase the size of the computational domain than to use annihilation boundary layers but that would increase the amount of computational resources needed for these runs by a factor of n_new^2/n_old^2 for the amount of memory needed and n_new^3/n_old^3 for the amount of computational time where n_new and n_old are the new and old number of grid points in one spatial dimension.

Figure 5.20 shows that the behavior of the mass distribution is quite similar when comparing the same initial density distributions with different values of N. In figure 5.20, the time steps of each successive frame are in increments of 0.5 with the first frame starting at time $t = 0.0$ and the last frame ending at time $t = 7.5$. Each frame shows a density distribution which is very similar to its respective frame in movie 5.19. This is to be expected, as the average angular momentum for the $N = 5$ figure is initially 2.5 times

that of the $N = 2$ figure while the time step from one frame in the $N = 5$ figure is a factor of 2.5 times shorter than the time step for the $N = 2$ movie. The major difference is that the density distributions are not as smooth as for the $N = 2$ distributions. This means that one not only needs a larger computational domain but also greater resolution to obtain results which are not dominated by errors incurred from the finite difference approximation of the original differential equations.
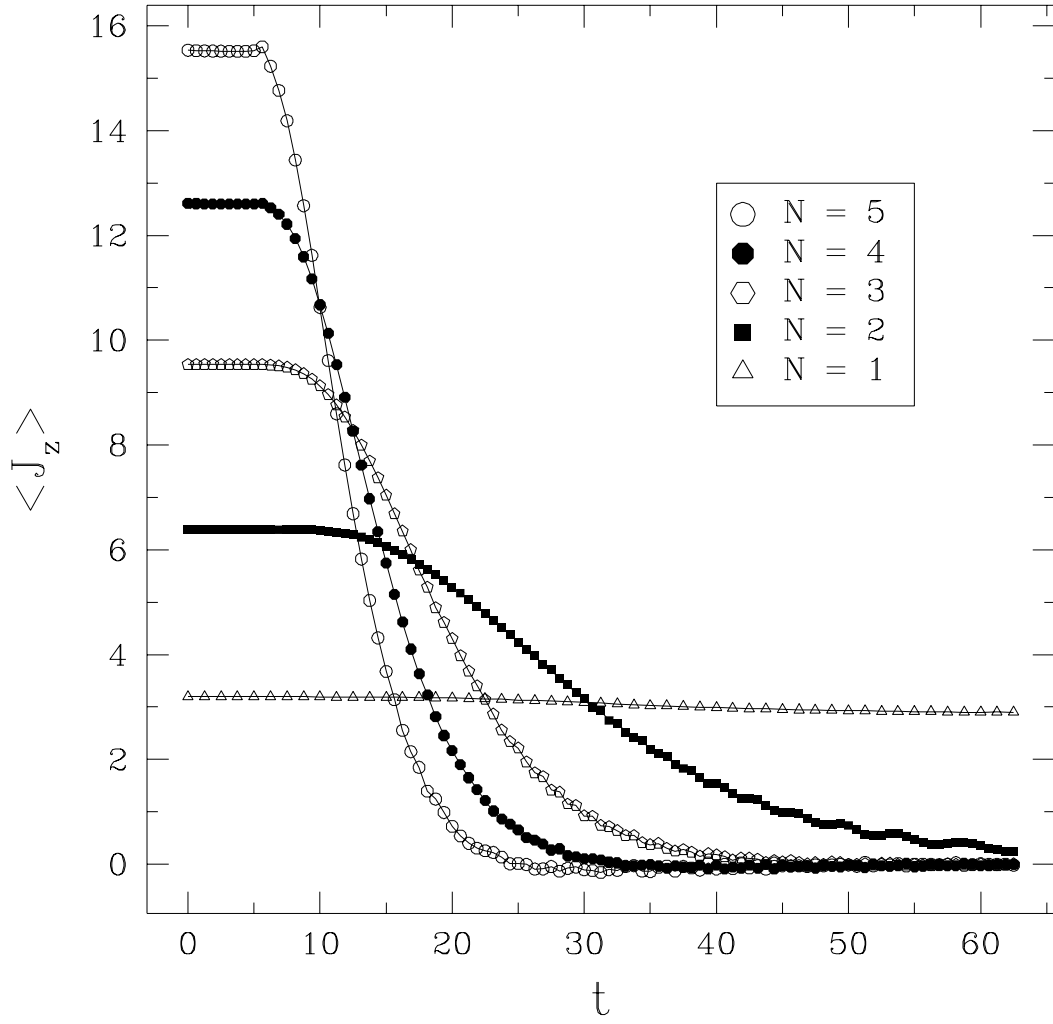
Figure 5.17: Plot of the average angular momentum as a function of time for a boson star set up initially as a 'quantum whirlpool' for quantized values of angular momenta.
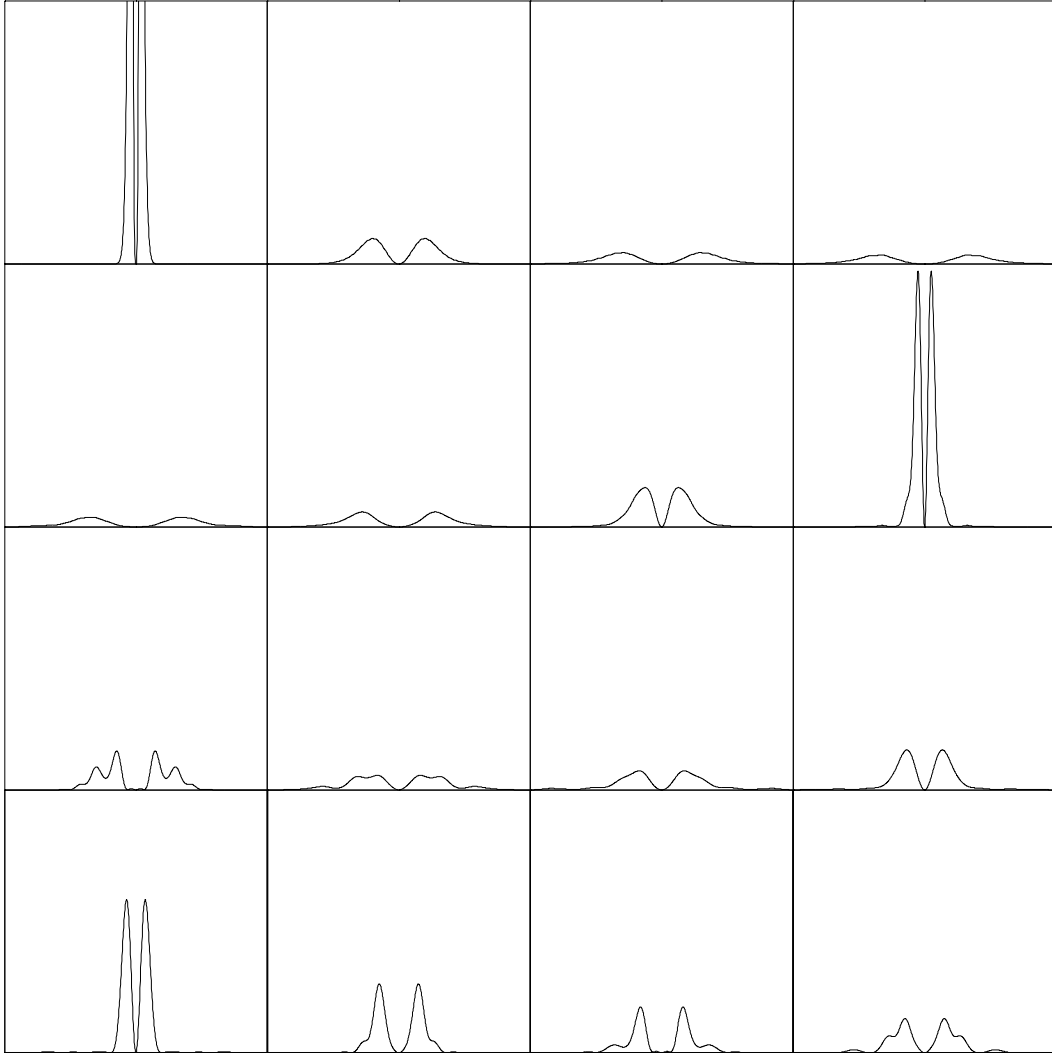
Figure 5.18: Movie of the density distribution of the $N = 1$ 'quantum whirlpool' along the x-axis at successive times with time step size of 12.5. The first frame is $t = 0.0$, and the last frame is $t = 187.5$. The domain goes from $x = -32$ to $x = 32$ and the range extends from $\rho = 0.0$ to $\rho = 0.09$.
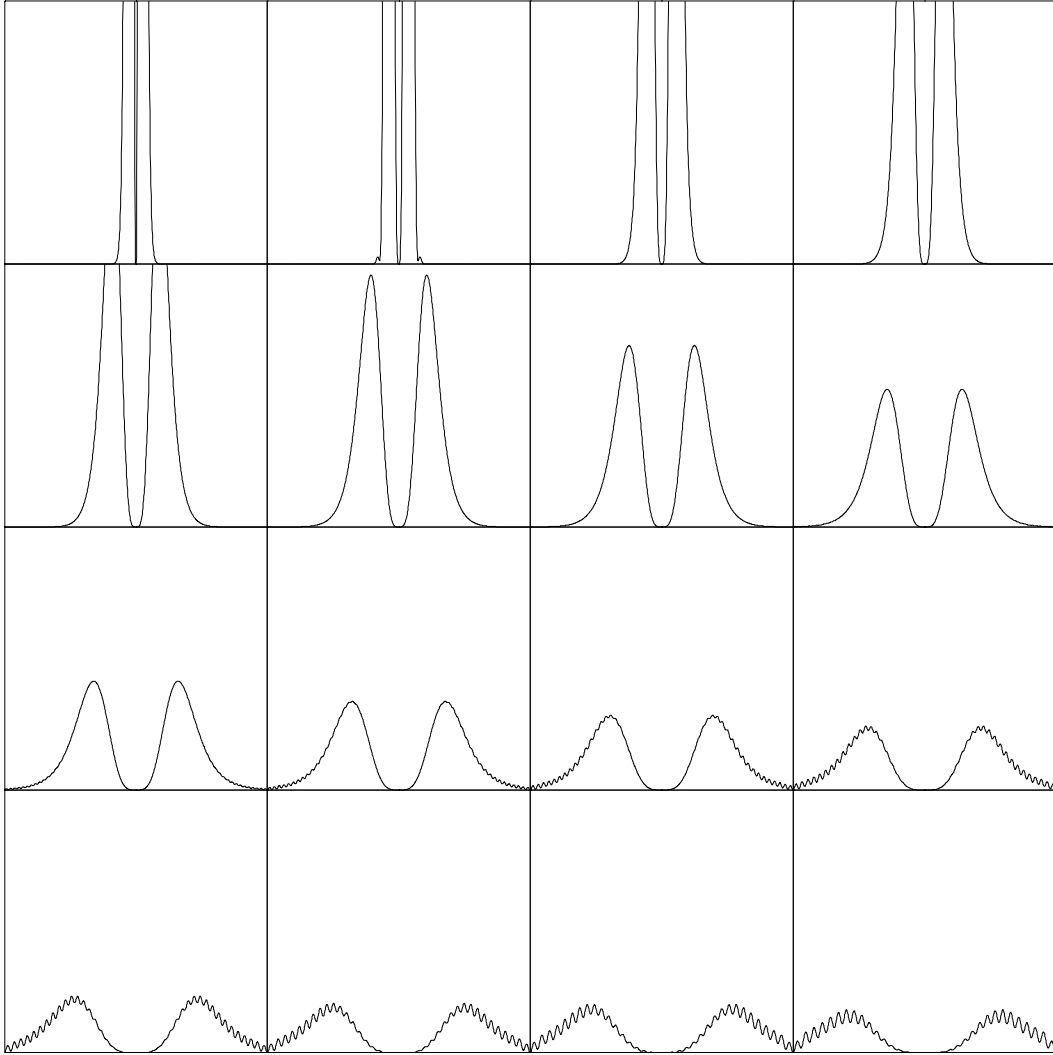
Figure 5.19: Movie of the density distribution of the $N = 2$ 'quantum whirlpool' along the x-axis at successive times with time step size of 1.25. The first frame is $t = 0.0$, and the last frame is $t = 18.75$. The domain goes from $x = -32$ to $x = 32$ and the range extends from $\rho = 0.0$ to $\rho = 0.01$.
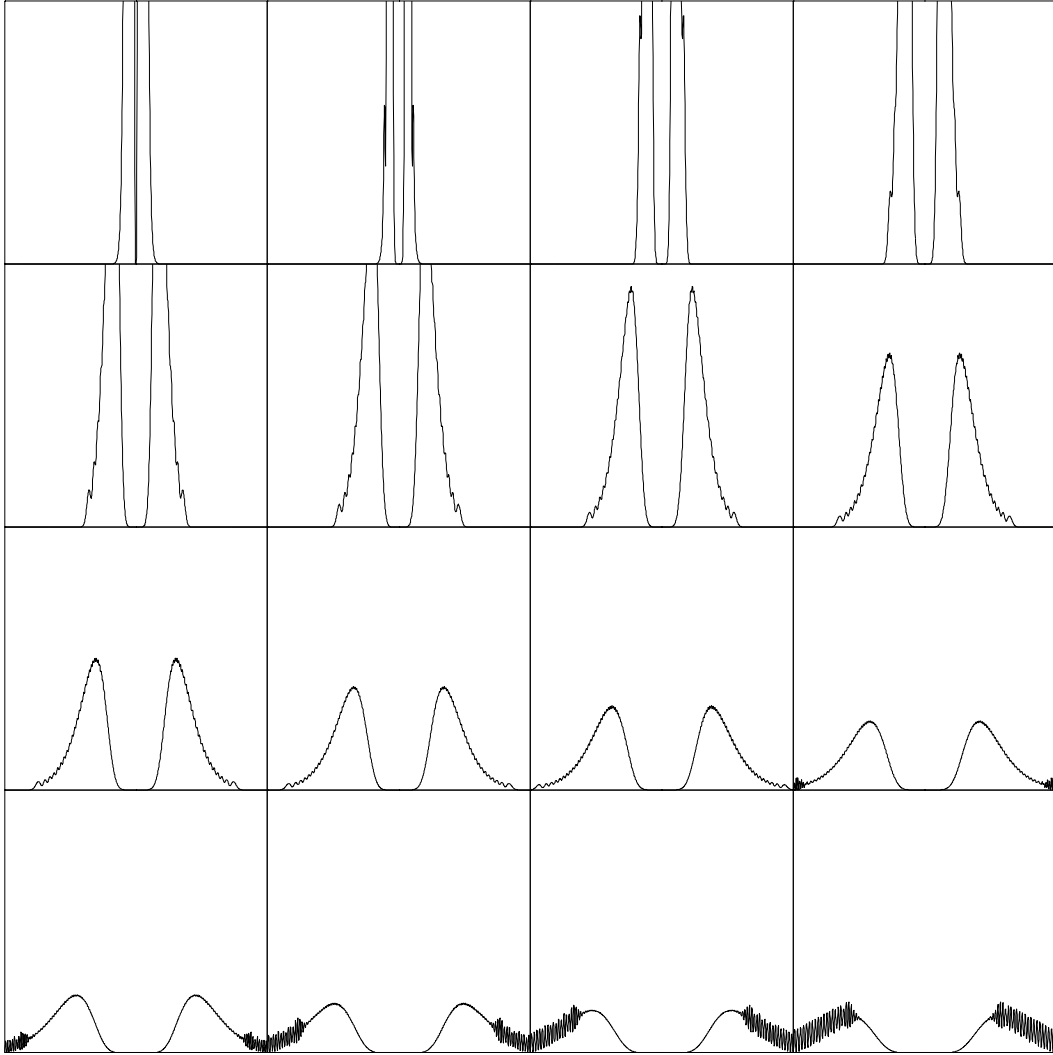
Figure 5.20: Movie of the density distribution of the $N = 5$ 'quantum whirlpool' along the x-axis at successive times with time step size of 0.5. The first frame is $t = 0.0$, and the last frame is $t = 7.5$. The domain goes from $x = -32$ to $x = 32$ and the range extends from $\rho = 0.0$ to $\rho = 0.01$.

Chapter 6

Conclusion

There are several conclusions from this work. One is that time dependent numerical solutions of three dimensional PDEs require careful planning and study. As one has seen, the coupling of the Schrödinger and Newtonian gravity equations lead to added algorithm complexities. Thus, there is a need to understand the errors of the difference scheme used in solving this coupled system of equations. By choosing a Crank-Nicolson scheme, the difference technique is guaranteed to be unconditionally stable. However, unconditionally stable difference schemes for solving time dependent problem are usually implicit methods which means that one will have to solve large systems of linear equations. Thus optimal[1] techniques for solving these sets of linear equations are needed. After one has a difference scheme in hand, it must be rigorously tested through convergence checking. Convergence tests need to be performed to ensure that for a given spatial and temporal spacing, the solution given by the difference scheme is a good approximation of the analytic solution of the PDEs being studied.

Another conclusion is the need to implement absorbing or other well be-

---

[1]By optimal it is meant that the number of calculations to solve N linear equations is of $O(N)$.

haved boundary conditions when fitting a finite computational domain within an infinite physical domain for time dependent problems. Invariably, this means the difference equations will use approximate boundary conditions. Chapter 4 showed that annihilation boundary layers are a good method to use when studying boson stars. They absorb outgoing matter with little reflection and preserve the validity of the difference solution in the interior of the computational domain. However, for effectiveness they require a large number of grid points which makes them quite expensive to use in currently practical uni-grid computations. This gives an argument for the use of an adaptive mesh refinement technique which would allow coarser grids near the boundaries and will reduce the computational cost of annihilation boundary layers.

The results of chapter 5 along with the hydrodynamic analogy given at the end of chapter 2 show that the errors due to solving the finite difference equations are quite apparent when boson stars are given linear momentum. The deceleration of boson stars seen in the linear momentum section can be explained by nonsymmetric contours in the density of the boson stars. The attempt to orbit a boson star was only partially successful. It would be interesting to perform a calculation on a much larger computational grid. There the tidal effects of the central potential are unimportant, but the current inability to precisely predict the motion of a boson star when given linear momentum could prevent attempts to have a star orbit around a fixed central potential. Again, this is an argument for the need of an AMR code to solve (1.1) and (1.2).

A parallel AMR code has been developed[21] using the Distributed Adaptive Grid Hierarchy (DAGH) structures developed by Manish Parashar[41].

The code uses an algorithm based on that of Berger and Oliger [7] with an adaptation which uses a shadow hierarchy of grids in calculating the local truncation error. [6] The clustering algorithm for regridding is described in [20] which discusses the Berger and Rigoutsos clustering method[2]. One current holdup to determining how well this method works are multiple grid input/output parallel data structures. Without these data structures, detailed analysis of the performance of the three dimensional parallel adaptive code would be extremely tedious.

The possibilities for future research based on the results of this dissertation are quite numerous. As mentioned in the introduction this code can be adapted to study large structure formation by solving equations:

$$\frac{\partial \phi}{\partial t} = \frac{i}{2a^2}\nabla^2 + V\phi \tag{6.1}$$

$$\nabla^2 V = \frac{1}{a}\left(\phi\phi^* - <\phi\phi^*>\right). \tag{6.2}$$

where $a(t) = (t/t_0)^{2/3}$ is the Robertson-Walker scale factor, t_0 is the current age of the universe in the computational dimensionless units described at the beginning of Chapter 3, and $a^3 < \phi\phi^* >= \rho_{crit}$ is the critical density at and above which the universe continues expanding. Thus, by incorporating the scale factor into the boson star code and using periodic boundary conditions, one can observe large scale structure formation dominated by dark matter from an initial density distribution of the dark matter. We believe that the adaptive code could be competitive with particle mesh codes [12, 10] and therefore worth trying out.

One could also use the boson star code to do simulations of collisionless matter. The code could be set up to do high resolution simulations of galaxy

formation from dark matter[27] which might allow one to correctly simulate the structure of dark matter haloes in dwarf galaxies which particle codes are unable to resolve correctly[5]. Of course this code would only be valid when two body interactions are unimportant[42].

At the current time there is a resurgence of interest in boson stars with recent preprints released on rotating boson stars[54], simulating galactic halos using boson stars[34] and axially symmetric boson stars[51]. Each of these papers only discusses stationary solutions. Thus given the data of there solutions, the boson star could quickly confirm the validity and stability of their solutions as well as lead to some interesting dynamical studies.

Bibliography

[1] V.A. Baskakov and A.V. Popov. Implementation of transparent boundaries for the numerical solution of the Schrödinger equation. *Wave Motion*, 14:123, 1991.

[2] M. Berger and I. Rigoutsos. An algorithm for point clustering and grid generation. *IEEE Transactions on Systems, Man and Cybernetics*, 21(5):1278–1286, 1991.

[3] M.J. Berger and J. Oliger. Adaptive mesh refinement for hyperbolic partial differential equations. *J Comp Phy*, 53:484–512, 1984.

[4] A. Brandt. *Multigrid Techniques: 1984 Guide with Applications to Fluid Dynamics*. Number 85. GMD-Studien, 1984.

[5] A. Burkett. The structure of dark matter haloes in dwarf galaxies. Max-Planck-Institut für Astronomie preprint, submitted to ApJ Letters to Editor, `http://xxx.lanl.gov/Archive/astro-ph/9504041` 1995.

[6] M. Choptuik. The Berger and Oliger algorithm using a shadow hierarchy for truncation error estimation. (unpublished), May 1995.

[7] M.W. Choptuik. Experiences with an adaptive mesh refinement algorithm in numerical relativity. In C.R. Evans, L.S. Finn, and D.W. Hobill, ed-

itors, *Frontiers in Numerical Relativity*, pages 206–221, New York, 1989. Cambridge University Press.

[8] M.W. Choptuik. "critical" behaviour in massless scalar field collapse. In Ray d'Inverno, editor, *Approaches to Numerical Relativity*, pages 202–222, New York, 1991. Cambridge University Press.

[9] M.W. Choptuik. *Phys Rev Lett*, 70:9, 1993.

[10] H.M.P. Couchman, P.A. Thomas, and F.R. Pearce
. An adaptive mesh implementation of $p^3m - sph$. preprint
, `http://xxx.lanl.gov/ps/astro-ph/9409058` 1994.

[11] Cray Research, Inc., Mendota Heights, MN. *CF77 Optimization Guide (SG-3773 6.0)*, 1993.

[12] M. Davis and et al. The evolution of large-scale structure in a universe dominated by cold dark matter. *The Astrophysical Journal*, 292:371–394, 1985.

[13] L. de Broglie. *An Introduction to the Study of Wave Mechanics*. Dutton, New York, 1930.

[14] P.A.M. Dirac. *Proc. R. Soc. Lond*, 133:60, 1931.

[15] D.J.D. Earn and S. Tremaine. *Physica D*, 56:1, 1992.

[16] A.K. Stagg et al. Parallel, scalable parabolized navier-stokes solver for large scale simulations. *AIAA Journal*, 33(1):102–108, 1995.

[17] S.M. Faber and J.S. Gallagher. *Annu. Rev. Astron. Astrophys.*, 17:135, 1979.

[18] D. Fisher, S. Klasky, and M. Parashar. Wake field acceleration simulation. Conference proceedings, 1995.

[19] N. Gouda, N. Sugiyama, and M. Sasaki. *Prog. Theor. Phys.*, 85:1023, 1991.

[20] R. Guenther. Clustering algorithm. (unpublished), 1995.

[21] R. Guenther and et al. A three dimensional adaptive parallel boson star code using a distributed adaptive grid hierarchy. (unpublished), 1995.

[22] J.O. Hirshfielder and K.T. Tang. *J. Chem. Phys.*, 65:470, 1976.

[23] M. Israeli and S.A. Orszag. Approximation of radiation boundary conditions. *J Comp Phy*, 41:115–135, 1981.

[24] J. J. Dongarra and et al. . The NETLIB repository at UTK and ORNL. `http://netlib.cs.utk.edu/`.

[25] J.D. Jackson. *Classical Electrodynamics*. John Wiley and Sons, New York, 2nd edition, 1975.

[26] P. Jetzer. Boson stars. *Physics Reports*, 220(4):163–227, 1992.

[27] R.E. Kates, E.V. Kotok, and A.A. Klypin. High-resolution simulations of galaxy formation in a cold dark matter scenario. *Astronomy and Astrophysics*, 243:295–308, 1991.

[28] S.A. Klasky. *Numerical techniques for the initial value problem for two black holes*. PhD thesis, University of Texas at Austin, December 1994.

[29] E. W. Kolb and M. S. Turner. *The Early Universe*. Addison-Wesley, 1990.

[30] H. Kreiss. *Numerical Methods for Solving Time-dependent Problems for Partial Differential Equations.* University of Montreal Press, 1978.

[31] H. Kreiss and J. Oliger. *Methods for the Approximate Solution of Time Dependent Problems.* Number Garp Publication Series No. 10. Unipub, Lanham, MD, 1973.

[32] L.D. Landau. *J. Phys.*, 5(133):71, 1941.

[33] L.D. Landau and E.M. Lifshitz. *Fluid Mechanics.* Pergamon Press, Elmsford, New York, 2nd edition, 1987.

[34] J. Lee and I. Koh. Galactic halos as boson stars
. `http://xxx.lanl.gov/Archive/astro-ph/9507385`, 1995.

[35] E. Madelung. *Z. Phys.*, 40:322, 1928.

[36] R. Matzner. Notes on "implementation of transparent boundaries for the numerical solution of the Schrödinger equation". (unpublished) Notes on Baskakov and Popov paper, 1994.

[37] R. Matzner and et al. Black hole binaries: Coalescence and gravitational radiation. (unpublished) Proposal for the Computational Grand Challenge Program, 1993.

[38] E. Merzbacher. *Quantum Mechanics.* Wiley, New York, 2nd edition, 1970.

[39] C.W. Misner and K.S. Thorne J.A. Wheeler. *Gravitation.* W.H. Freeman and Company, New York, 1973.

[40] A.R. Mitchell and D.F. Griffiths. *The Finite Difference Mehtod in Partial Differential Equations.* John Wiley & Sons, Chichester, 1980.

[41] M. Parashar and J.C. Browne. An infrastructure for parallel adaptive mesh refinement techniques
. http://godel.ph.utexas.edu/Members/parashar/toolkit.html.

[42] P.J.E. Peebles. *Principles of Physical Cosmology*. Princeton University Press, Princeton, New Jersey, 1993.

[43] W.H. Press and et al. *Numerical Recipes in Fortran*. Cambridge University Press, Cambridge, second edition, 1992.

[44] J.J. Quirk. An alternative to unstructured grids for computing gas dynamic dynamic flows around arbitrarily complex two-dimensional bodies. *Computers Fluids*, 23(1):125–142, 1994.

[45] L.F. Richardson. *Philos. Trans. R. Soc.*, 210:307, 1910.

[46] J. Riess and H. Primas. *Phys. Rev. D.*, 2:647, 1970.

[47] V.C. Rubin, W.K. Ford, and N. Thonnard. *ApJ*, 238:471, 1980.

[48] R. Ruffini and S. Bonazzola. Systems of self-gravitating particles in general relativity and the concept of equation of state. *Phys. Rev.*, 187:1767, 1969.

[49] R. Sancisi and T.S. van Albada. In A. Hewitt, G. Burbidge, and Fang Li Zhi, editors, *Observational Cosmology, IAU Symp. 124*, Dordrecht, 1987. Reidel.

[50] R. Sancisi and T.S. van Albada. In J. Kormandy and K.R. Knapp, editors, *Dark Matter in the Universe, IAU Symp. 124*, Dordrecht, 1987. Reidel.

[51] B. Schupp and J.J. van der Bij. An axially-symmetric newtonian boson star. Max-Planck-Institut für Astronomie preprint, `http://xxx.lanl.gov/Archive/astro-ph/ /9508017`, 1995.

[52] B.F. Schutz. *A first couse in general relativity*. Cambridge University Press, Cambridge, 1989.

[53] E. Seidel and Wai-Mo Suen. Dynamical evolution of boson stars: perturbing the ground state. *Phys. Rev. D*, 42(2):384, 1990.

[54] V. Silveria and C. de Sousa. Boson star rotation: a newtonian approximation. `http://xxx.lanl.gov/Archive/astro-ph/9508034`, 1995.

[55] R.T. Skodje, H.W. Rohrs, and J. VanBuskirk. Flux analysis, the correspondence principle, and the structure of quantum phase space. *Phys. Rev. A*, 40(6):2894, 1989.

[56] T. Takabayasi. *Prog. Theor. Phys.*, 14:283, 1955.

[57] M. Wang and S.P. Vanka. A paralllel ADI algorithm for high-order finite-difference solution of the unsteady heat conduction equation, and its implementation on the cm-5. *Numerical Heat Transfer, Part B*, 24:143–159, 1993.

[58] S. Weinberg. *Gravitation and Cosmology*. Wiley, New York, 1972.

[59] P. Wesseling. *An Introduction to Multigrid Methods*. John Wiley & Sons, Chichester, 1992.

[60] R.L. White. *The Use of Supercomputers in Stellar Dynamics*. Springer, Berlin, 1986.

[61] L.M. Widrow and N. Kaiser. Using the Schrödinger equation to simulate collisionless matter. *ApJ*, 416:L71, 1993.

[62] H.E. Wilhelm. *Phys. Rev. D.*, 1:2278, 1970.

[63] D.M. Young and R.T. Gregory. *A Survey of Numerical Mathematics*, volume I. Dover, Toronto, 1988.

[64] D.M. Young and R.T. Gregory. *A Survey of Numerical Mathematics*, volume II. Dover, Toronto, 1988.

[65] F. Zwicky. *Helv. Phys. Acta.* , 6:110, 1933.

Vita

Reid Larimore Guenther, son of Ruth Rike and Anthony Guenther, was born December 22, 1966 in Indianapolis, Indiana. He was raised in Memphis, Tennessee by Harry and Ruth Rike, Reid graduated Salutatorian from the Central High School Honors Program in 1985. He received his B. A. in Physics in the spring of 1989. In the fall of 1989, he entered graduate school at the University of Texas at Austin and worked towards his Ph.D. in Physics.

Permanent address: 11250 Taylor Draper Lane #1123
Austin, Texas 78759
U.S.A.

This dissertation was typeset with LaTeX[‡] by the author.

[‡]LaTeX is a document preparation system developed by Leslie Lamport as a special version of Donald Knuth's TeX Program.